

ABSTRACT

MOODY, BENJAMIN. Exploring New Detection Schemes for Molecular Detection, Nucleic Acid Research, and the Study of *In Situ* Cellular Chemistry. (Under the direction of Gregory S. McCarty).

In complex and dynamic environments such as biological systems, new detection schemes that are quick, inexpensive, and non-invasive are necessary to provide analyses with high quality data. To this end, the research presented here is focused on exploring new detection schemes for molecular detection, nucleic acid research, and the study of *in situ* cellular chemistry. This research investigates the use of surface enhanced Raman spectroscopy (SERS) as the primary detection technique, starting first with experiments designed to broaden and improve the application of SERS within biomedical settings and then applying SERS to further the fundamental understanding of relevant biomedical topics such as DNA mutation and stem cell differentiation.

The first set of experiments to be discussed involves a methodology to produce solid state nanogap electrodes. In Chapter 2 a combination of oligonucleotide-based molecular lithography and traditional photolithography is used to create finely tunable nanogap electrodes and to explore the fabrication of Raman enhancing substrates. Solid state nanogaps represent a relevant application of nanolithography as they can be used in sensitive chemical and biological detection schemes and are invaluable for investigating molecular electronic candidates, for researching biological systems, and as substrates for surface enhanced Raman spectroscopic studies. Here, nanogaps are implemented for monitoring by

using two detection schemes, one optical (SERS) and one electronic (current-voltage responses). Using the strong Raman enhancements created by the nanogap, Raman spectra and current voltage traces show that the oligonucleotides used as the molecular resist are degraded during processing, that some of the degraded oligonucleotides are removed, and that fresh oligonucleotides are adsorbed.

Next, a methodology is explored to enable the collection of statistically significant SERS data using single nucleotide polymorphisms as a model system. We report a method of using surface enhanced Raman spectroscopy to probe single stranded DNA for genetic markers. Single-stranded oligonucleotides functionalized with gold nanoparticles are hybridized with oligonucleotides adsorbed to photolithographically defined gold surfaces thus creating a surface enhanced Raman environment around the DNA duplex. With this design characteristic Raman spectra are analyzed for differences between DNA duplexes formed from complementary oligonucleotides, completely mismatched oligonucleotides, and those formed from oligonucleotides that have a mid-sequence single nucleotide mismatch. The results show that statistically significant differences in Raman intensity for characteristic peaks can be collected for the three cases. This method is then improved upon by analyzing *unmodified* genes of moderate length by introducing the genes into a surface enhanced Raman complex. With this design we are able to collect characteristic Raman spectra about the genes and to again detect genetic markers such as single-nucleotide polymorphisms but also a variety of additional polymorphic regions. Results show that strands containing one of

three different types of polymorphism can be differentiated using statistically significant peak position differences and trends regarding Raman intensity.

Finally, SERS is utilized in a more dynamic biological environment – in living human stem cells. Living cells uptake gold nanoparticles and sequester these particles in the endosomal pathway. Once inside the endosome, nanoparticles aggregate into clusters that give rise to large spectroscopic enhancements that can be used to elucidate local chemical environments through the use of surface enhanced Raman spectroscopy. This research uses colloidal gold nanoparticles to create volumes of surface-enhanced Raman scattering (SERS) within living human adipose derived adult stem cells enabling molecular information to be monitored. We exploit this technique to spectroscopically observe chemical changes that occur during the adipogenic differentiation of human adipose derived stem cells over a period of 22 days, monitoring both the production of lipids and the complex interplay between lipids, proteins, and chemical messengers involved in adipogenesis.

Exploring New Detection Schemes for Molecular Detection, Nucleic Acid Research, and the
Study of *In Situ* Cellular Chemistry

by
Benjamin Patrick Moody

A thesis submitted to the Graduate Faculty of
North Carolina State University
in partial fulfillment of the
requirements for the degree of
Doctor of Philosophy

Biomedical Engineering

Raleigh, North Carolina

2010

APPROVED BY:

Gregory S. McCarty (Committee Chair)

Michael P. Gamcsik

Elizabeth G. Loba

Glenn Walker

Paul Wollenzien

Biography

Benjamin Moody graduated from Virginia Tech with a BS in Chemical Engineering and a minor in chemistry. After working for several years in the pharmaceutical industry he returned to school in pursuit of a Ph.D. from the Joint Department of Biomedical Engineering at North Carolina State University and the University of North Carolina at Chapel Hill.

Acknowledgements

I would like to gratefully acknowledge:

Dr. Gregory S. McCarty

Dr. Elizabeth Lobo

Dr. Glenn Walker

Dr. Paul Wollenzien

Dr. Michael P. Gamcsik

Dr. Carla M. Haslauer

Dr. Wayne Pfieler

Dr. Seth McCullen

Dr. Dale Bachelor

J.B. Clark

Amy McPherson

Stefan Ufer

Dr. Susan Bernacki

Ariel Hanson

Joanna Stocking

John Leotaud

NC State Analytical Instrumentation Facility

North Carolina State University College of

Engineering

Charles Jones

Elizabeth Moody

Matthew K. Zachek

James Roberts

Dr. Leslie Sombers

Dr. Adrian O'neill

Jeff Soohoo

Linda Simmerson

Nancy McKinney

Brian Gonzalez

Andrew Brna

Rekha Balasubramanyam

Stephanie Gootnick

Richard Green

Chuck Mooney

Valerie Knowlton

NC State Center for Electron Microscopy

Table of Contents

List of Tables	vii
List of Figures	viii
Chapter 1: Introduction	1
1.1 Raman spectroscopy and SERS	2
1.1.1 Basic physics.....	2
1.1.2 Competing spectroscopies.	2
1.1.3 Surface enhanced Raman spectroscopy.....	4
1.2 Single Nucleotide Polymorphisms.....	6
1.2.1 Background.....	6
1.2.2 Detection.....	7
1.3 Cell Monitoring.....	9
1.4 Objectives	10
1.4.1 Fabricating Raman enhancing solid-state nanogap sensors.....	11
1.4.2 Detecting and evaluating mid-sequence SNPs.....	12
1.4.3 Developing real-time cell monitoring systems	13
1.5 Dissertation Findings	14
Chapter 2: Solid State Nanogaps for Differential Measurements of Molecular Properties... 17	
2.1 Introduction.....	18
2.2 Materials and Methods.....	20
2.2.1 Electrodes/Nanogap fabrication.....	20
2.2.2 Raman Spectroscopy.....	21
2.3 Results and Discussion	23
2.4 Conclusion	28
Chapter 3: Statistically Significant Raman Detection of Mid-Sequence Single Nucleotide Polymorphisms	29
3.1 Introduction.....	30
3.2 Materials and Methods.....	33
3.2.1. Substrate Preparation 1	34
3.2.2 Oligo Preparation 1 (Capture Strands).....	34
3.2.3 Substrate Preparation 2	35
3.2.4 Oligo Preparation 2 (Target Strands).....	35
3.2.5 Hybridization	36
3.2.6 Raman Detection.....	36
3.3 Results and Discussion	39
3.4 Conclusions.....	43

Chapter 4: Using Surface Enhanced Raman Spectroscopy to Probe for Genetic Markers on Single Stranded DNA	44
4.1 Introduction.....	45
4.2 Materials and Methods.....	48
4.2.1 Substrate Preparation 1	48
4.2.2 Oligo Preparation 1 (Capture Strands).....	49
4.2.3 Substrate Preparation 2	52
4.2.4 Oligo Preparation 2 (Target Strands).....	52
4.2.5 Oligo Preparation 3 (Test Strands).	53
4.2.6 Hybridization.	53
4.2.7 Raman Detection.....	54
4.2.8 Statistical Analysis.....	54
4.3 Results.....	55
4.4 Discussion	61
4.5 Conclusions.....	66
 Chapter 5: In Situ Monitoring of Adipogenesis with Human Adipose Derived Stem Cells Using Surface Enhanced Raman Spectroscopy	67
5.1 Introduction.....	69
5.2 Methods and Materials.....	71
5.2.1 Cell Culture.....	71
5.2.2 Raman Detection.....	71
5.2.3 Data Processing.....	73
5.3 Results.....	74
5.4 Discussion	82
5.5 Conclusions.....	88
 Chapter 6: Future Directions.....	89
6.1 Investigation of the SERS Effect	89
6.2 Single-Cell SERS Analyses	91
6.3 Multidimensional Analysis of SERS Data.....	99
6.4 Intracellular SERS Targeting using Antibodies.....	106
 Chapter 7: Conclusions	111
 References.....	114
 Appendix.....	124
A. Soft Lithography Protocol.....	125
B. Photolithography Protocol.....	129

B.1. Photresist Application	129
B.2. CANON 501 With Alignment Procedure	132
B.3. Photresist Development.....	138
C. Electron Beam Evaporate Protocol	139

List of Tables

Table 3.1: Oligonucleotide Design for A-G and C-T Oligo Sequences	39
Table 4.1: Oligonucleotide Design for Matched and Mismatched Sequences	51
Table 4.2: Two-tail p-values from t-test results used to test the significance of intensity differences among selected peaks. Asterisks represent corresponding significance level. ...	57
Table 4.3: Two-tail p-values from t-test results used to test the significance of peak position differences among selected peaks. Asterisks represent corresponding significance level. ...	60
Table 5.1: Raman shift assignments and interpretations of Raman shifts observed in human adipose derived adult stem cells before, during, and after adipogenic differentiation.	77
Table 6.3.1: Sample type classification accuracy of the four-group PCA-LDA model as assessed by a leave-one-out cross-validation. The seven median spectra from each sample type were baseline subtracted prior to PCA-LDA analysis.	100
Table 6.3.2: Leave-one-out LDA cross validation sensitivities for classifying all 31 spectra from each sample group. Spectra were baseline subtracted and normalized prior to LDA analysis.	101
Table B.1: Positive Photoresist Application Specifications	127
Table B.2: Negative Photoresist Application Specifications	128
Table B.3: Exposure time parameters	131

List of Figures

Figure 2.1: Schematic showing the process of hybrid molecular lithography.....	20
Figure 2.2: Raman signal from a nanogap created using single-stranded oligonucleotides as a molecular resist in the structure's fabrication. Figure 1a shows a portion of the Raman spectra collected at the electrode interface as fabricated, after a dodecanethiol (DDT) substitution, and then after thiol functionalized oligonucleotides (Oligos) were added to the solid state nanogap. Figures 2.1b and 2.1c are the spectra that result from subtracting the As Fabricated trace from the Dodecanethiol trace and from subtracting the Dodecanethiol trace from the Oligonucleotide trace, respectively. These latter spectra are used to highlight the change in condition between two states.....	24
Figure 2.3: Current – voltage characteristics for the electrode as fabricated, after the dodecanethiol substitution, and then again after the final oligonucleotide addition. The electrode conducted 350 nA as fabricated, 18 nA after the alkane substitution, and 130 nA after the oligo substitution, all at +0.5 V of applied bias.....	25
Figure 3.1: Visualization of the hybridization scheme used to create a SERS environment around DNA duplexes.....	34
Figure 3.2: Raman spectra comparing the averaged median intensities of single-stranded oligos (matched, mismatched, and single-mismatched) hybridized to form double-stranded duplexes using the a) C-T and b) A-G sequences. Standard error bars are included for key peaks along with asterisks that indicate the level of statistical difference.	42
Figure 4.1: Visualization of the hybridization scheme used to create a SERS environment around DNA duplexes. Single stranded oligos are hybridized as either completely matched, with a single mismatch (SNP), with an adjacent triple mismatch (ATM), or with a delocalized triple mismatch (DTM). Grey boxes highlight the mismatches for clarity.	50
Figure 4.2: Raman spectra comparing the averaged median intensities of single-stranded oligos (matched, single-mismatched, delocalized triple mismatched, adjacent triple mismatch, and completely mismatched) hybridized to form double-stranded duplexes. Standard error bars are included for the key peaks. (see Table 2 for p-values).....	56
Figure 4.3: Scanning electron micrographs of representative sample capture surfaces after hybridizing single-stranded oligos and gold nanoparticles to form double-stranded SERS complexes (top row). The bottom row contains corresponding particle count analyses that clarify the different particle densities of each micrograph. These images enable a qualitative	

analysis of the nanoparticle densities that results from hybridizing with (A) completely matched, (B) SNP, (C) triple mismatched, and (D) completely mismatched test strands..... 57

Figure 4.4: Raman spectra highlighting the peak position shifts that occur when comparing the average matched sample to the SNP and ATM samples. The DTM sample followed in trend with the other mismatched samples and was therefore excluded for clarity. The highlighted peaks represent (A) down-shifting guanine ring breathing and (B) phosphodiester stretch modes, and (C) an up-shifting guanine/sugar stretch. Peak positions are shown with their respective standard errors representing the variability between the seven median spectra averaged together to obtain these positions. Levels of significant difference are compared to the matched sample. Constituent peak intensities were baseline subtracted and normalized to the peak of interest before averaging then smoothed. (see Table 4.3 for p-values) 59

Figure 5.1: Transmission electron micrographs of colloidal gold nanoparticles aggregated within differentiating hASCs. Nanoparticles are 40 nm in diameter..... 74

Figure 5.2: Representative surface-enhanced Raman spectra of undifferentiated hASCs measured 2 (blue), 6 (black), 8 (red), and 44 (green) days after seeding. Spectra are smoothed and normalized to the ubiquitous 1328 cm^{-1} protein peak¹⁻³ and offset for comparison..... 75

Figure 5.3: Representative surface-enhanced Raman spectra measured from hASCs at various time points during adipogenic differentiation. Samples were analyzed shortly after the addition of differentiation medium at (a) 1 and (b) 2 days then at intermediate time points between (c) 6 and 20 days and then finally at (d) 22 days. The variety of peak positions indicates the complex chemical changes that occur during differentiation. Spectra are smoothed and normalized to the ubiquitous 1328 cm^{-1} protein peak¹⁻³ and offset for comparison..... 77

Figure 5.4: Raman spectra showing an average of the five fully differentiated adipocyte spectra from Figure 5.3d compared to an average of the four undifferentiated stem cell spectra in Figure 5.2. The figure highlights the spectral similarities and differences that are common between undifferentiated and differentiated stem cells. 79

Figure 6.2.1: Schematic of the microfluidic device to be used in hADAS cell differentiation study. Media flow will be from left to right via a syringe pump piped to the point where the lines intersection. White circles represent “cell spots” where collagen patches will be used to capture hADAS cells as described by O’Neill et. al.⁴ 92

Figure 6.2.2: Raman spectra taken from a living hADAS cell at four different locations. Figure shows the DNA characteristic spectrum visible at the nucleus as compared to the lipid/protein spectra taken elsewhere.....	95
Figure 6.3.1: PCA scores of each sample type as plotted against the first and second principle components. Each data point represents one of the seven median spectra as discussed in Chapter 4. Data was baseline corrected prior to PCA.	100
Figure 6.3.2: PCA scores of a) ATM and DTM sample types and of b) ATM, DTM, and SNP as plotted against the first and second principle components. The figure shows the similarities shared by the mismatched samples in general and contrasts the differences between the triple mismatched samples. Prior to PCA the data was baseline corrected and normalized to limit intensity variations thus highlighting variation between characteristic peaks.	103
Figure 6.3.3: PCA scores of the matched samples as compared to the a) SNP, b) DTM, and c) ATM as plotted against the first and second principle components. Despite sharing expected similarities, the PCA groupings in this figure show how generally distinguishable the matched samples are from samples with polymorphisms. Prior to PCA the data was baseline corrected and normalized to limit intensity variations thus highlighting variation between characteristic peaks.....	104
Figure 6.4.1: Raman spectra comparing the averaged Raman intensities of undifferentiated hASCs (blue) as compared to those that have been exposed to adipogenic differentiation medium for 1 day (green) and 22 days (red). The figure highlights the intensity reduction that is observed on average as the cell cultures differentiate. Spectra have been smoothed and baseline corrected.....	107
Figure 6.4.2: Raman spectra comparing the normalized average Raman intensities of undifferentiated hASCs (blue) as compared to those that have been exposed to adipogenic differentiation medium for 1 day (green) and 22 days (red). The figure highlights spectral similarities shared between the three groups. Spectra have also been smoothed and baseline corrected.....	108
Figure A1: Schematic outlining the four steps used to create a master wafer for soft lithography. Adapted from ⁵	123
Figure A2: Chemical structure of PDMS.....	125

Chapter 1: Introduction

The basis of scientific learning is the analytical experiment just as the basis of any experiment is detection. In the intersecting disciplines of biology, biochemistry, chemistry and biomedicine there have long been clever detection techniques capable of eliciting exciting and important information. However, as scientific disciplines evolve, so must the experiments and the detection techniques in which they are rooted. To this end, my research is focused on exploring new detection schemes for molecular detection, nucleic acid research, and the study of in situ cellular chemistry. Using a unique combination of tools and skillsets the intent of my recent research has been to improve the quality and depth of the detection and analysis techniques currently available in chemistry, biology, and biomedicine. Under the support and guidance of my advisor, Dr. Gregory S. McCarty, our lab has custom built a modular Raman microscope for use as a multipurpose chemical analyses platform around which we have conducted biomedical research involving nanolithography, surface enhanced Raman spectroscopy (SERS), genetic polymorphisms, adipogenesis, and stem cell differentiation. In addition, surface modification techniques using self-assembling monolayers (SAM), molecular lithography, standard photolithography, and electron beam deposition have been complemented with surface characterization instruments like the scanning electron microscope (SEM) and the atomic force microscope (AFM). In general

our main efforts are 1) to improve upon the scope of existing analytical techniques and 2) to further explore relevant fundamental questions in biology, chemistry, and physics.

1.1 Raman spectroscopy and SERS

1.1.1 Basic physics. The evolution of Raman spectroscopy from its conception in 1928 to its current state is a story whose scope far exceeds the limits of this document. While the curious reader can find excellent material on Raman's history, applications, and recent advances,⁶⁻⁸ for the more casual reader it will suffice to say that Raman spectroscopy has over time become a valuable tool in the scientist's tool belt. Today it is widely known to be inexpensive, relatively fast, and non-invasive with good detection sensitivity. In brief, the Raman effect is described as an inelastic scattering of light that occurs when an appropriately powerful monochromatic light source interacts with matter. For the purposes of our research, the scheme is essentially to reflect a single wavelength laser off a sample of interest and then to analyze the reflected light for any deviations in wavelength. Wavelength deviations are characteristic of different molecular functional groups and can thus be correlated to the chemical composition of the material the laser illuminates.

1.1.2 Competing spectroscopies and optical techniques. Among the wide range of applications of Raman spectroscopy, few are as progressively relevant as those involving biomedicine. Raman's unique qualifications include an ability to ascertain real-time chemical information from living systems, the ability to highlight micrometer areas for

analysis, a relative insensitivity to water, and the potential for the extreme spectroscopic enhancements. Raman is generally considered more powerful than IR spectroscopy but less destructive than UV-vis for chemical analyses. Nevertheless, it has been estimated that only one in a million photons undergo Raman scattering resulting in a relatively weak signal that has historically been difficult to detect. Therefore Raman has yet to find as broad an audience as competing optical techniques.

In medicine, for example, both intrinsic and extrinsic fluorophores have been used to study cellular and tissue changes that can result from cancer, atherosclerosis, miscellaneous oxidative events, or tooth decay.⁹ Fluorescence spectroscopy has also been used to great avail in genotyping, DNA sequencing, and single nucleotide polymorphism (SNP) detection.^{10, 11}

However, a great deal of interest in Raman spectroscopy is due to its unique advantages as compared to other optical techniques. For example, there is a greater number of Raman dyes or labels than fluorescent labels and multiplexing among Raman dyes is generally easier on account of the sharper, more distinct spectral signature Raman dyes exhibit.¹² Secondly, unlike most Raman dyes, fluorophores can be subject to photobleaching.¹³ Finally, because a single Raman spectrum created from a single monochromatic light source can have several peaks involved, it is more convenient to use peak ratio analyses with Raman spectroscopy.¹²

1.1.3 Surface enhanced Raman spectroscopy. Also, with improvements in lasers, bandpass and notch filters, and in light detectors in general, Raman spectroscopy is gaining in popularity and usefulness. Another significant advancement worth noting is the advent of surface enhanced Raman spectroscopy (SERS). SERS is a spectroscopic technique that amplifies and improves Raman signal within a very localized vicinity, generally around two closely spaced metal structures of varying size and design. While it is not definitively known exactly why or how this works, there are two well accepted models for explaining this enhancement of Raman activity, the electromagnetic model and the chemical or charge transfer model; and one emerging model, the dipole-quadrupole theory of Raman enhancement. The electromagnetic and charge transfer models have been discussed in the scientific literature since the discovery of SERS (~1974). Essentially the two models postulate, respectively, how surface plasmons on the metal features interact with the incident laser light to create an enhancing localized electric field or how the plasmons interact with the analyte itself to enhance the analyte's polarity and thus ability to reflect Raman scattered light. Neither adequately describes the complexity of the surface enhancements seen in SERS, especially the large enhancement factors recently observed experimentally. A dipole-quadrupole theory has recently been introduced to more adequately model the enhancement observed in SERS.^{14, 15} Note that recent advances have enabled density functional theory (DFT) to be used to calculate peak positions and relative intensities (e.g. very weak, weak, strong or very strong) for Raman spectra both normal Raman and SERS. Many papers have

been published studying simple molecules adsorbed to metal atoms both experimentally and theoretically with DFT. A few references are included for completeness.¹⁶⁻²⁰

The difficulty that frequently arises with SERS is creating substrates that have large and very uniform enhancement factors. Ideally SERS substrates should be efficiently fabricated on the wafer-size scale and will consist of small metallic structures with uniform spacing from a few hundred nanometers to just a few nanometers. More routinely, however, SERS substrates are subject to local unpredictable “hot spots” of enhancement and require advanced nanolithographic patterning to prepare.²¹⁻²³ Hot-spots are caused by areas of varying Raman enhancement on the substrate. This variable enhancement can lead to large sample-to-sample variations in Raman intensity and can result in data that is uncharacteristic of the system under study.²⁴ In addition to hot-spots, possibly large variations are frequently caused by other small differences in the substrate, non-specific binding, and random intermolecular interactions of the SERS features. As a result, variability can easily defeat attempts at obtaining statistically significant data for differentiation studies and because of this, Raman spectroscopy and SERS data are have become notorious for being difficult to interpret.

Nonetheless, there are many approaches to creating SERS environments including everything from chemical and electrochemical surface roughening to nanolithographic patterning schemes like e-beam lithography.^{21, 22} In this discussion however we primarily

focus on the SERS effect generated through the use of one of two techniques – closely packed gold nanoparticles and solid state nanogaps – both of which have previously been used to amplify Raman signal.²⁵⁻²⁸ We have chosen to use nanoparticles and solid state nanogaps because the spacing of both can be tailor-made with nanometer precision in attempts to specify the exact SERS effect.

1.2 Single Nucleotide Polymorphisms

1.2.1 Background. Deoxyribonucleic acid (DNA) mutations can be caused by exposure to either environmental mutagens or to internal physiological mutagens. More commonly they occur when an error in DNA replication or repair causes a single base in the DNA to spontaneously be deleted, inserted, or substituted.²⁹ Subsequently, a nucleotide mismatch is when non-complementary bases are left to align for Watson-Crick pairing. If the most frequent nucleotide in a single base of DNA is replaced by another nucleotide with a frequency greater than 1%,²⁹ the mutation is specifically classified as a single-nucleotide polymorphism (SNP).³⁰ Similarly, regions within a gene that has several of these “rearrangements” can generally be called a polymorphic region (PR).³¹ A cluster of SNPs or a cluster of deletions within a gene are examples of polymorphic regions.³²

On a molecular level, polymorphisms can lead to inappropriate amino-acid substitutions in proteins that alter the proteins’ function.³³ This has the potential of detrimentally affecting DNA repair, encouraging genetic instability, and promoting cancer.

Studies suggest that SNPs account for 90% of polymorphisms²⁹ in the human genome. In fact, an SNP database started by the National Center for Biotechnology Information in 1998 contained over 4 million human SNPs by 2005.³⁴ SNPs have been associated with breast, lung, head, and neck cancers among others³⁵ and as genetic markers SNPs are being used for mapping conditions as diverse as diabetes, multiple sclerosis, and obesity.³⁰ On the other hand, some SNPs are being researched for their beneficial roles in reducing disease susceptibilities and for the possibility of being used as a marker for improved drug reactions.²⁹

1.2.2 Detection. Currently, there is a plethora of different schemes used in SNP and PR detection,³⁶ though each generally relies on some combination of a smaller subset of discrimination and detection methods. For example, a standard high throughput rubric for SNP detection takes advantage of microarray technology, fluorescent tags, and the hybridization differences that occur between complementary oligonucleotides and those with nucleotide polymorphisms. One such method might hybridize oligo/fluorescent dye complexes with oligo/fluorescent quenching complexes. In this fashion the fluorescent tag remains quenched until the complex is somehow separated, usually through stringent washes. Because de-hybridization will occur under lower stringency for imperfectly hybridized oligonucleotides, SNP complexes will separate before perfectly complementary oligos thus triggering a detectable fluorescent signal as the fluorescent dye is distanced from its

quencher.^{10, 37} Integrating microarrays into such a setup allows the analysis of thousands of samples per day.¹⁰ Even moderately large sized eukaryotic genomes can now be explored for SNPs using oligonucleotide assays.³²

Other methods may use enzymes like DNA polymerases, DNA ligases, or the flap endonuclease to discriminate between normal and mismatched samples. Some systems forgo fluorescence-based optical detection for mass spectrometry.¹⁰ A few currently available commercial systems include GeneChip, Masscode, Invader, and SNaPShot. Whatever the system though, the main two steps remain – 1) differentiate between perfectly complementary and SNP samples and 2) detect that there is a difference.

On a less immediately commercial scale, recent innovations using DNA functionalized with gold nanoparticles has been shown to quickly detect terminal mismatches in DNA with a simple color change.³⁸ In 2004 it was noted that single stranded DNA oligos can be functionalized in separate solutions of gold nanoparticles, which have an inherent pink color. When the nanoparticle solutions of DNA with mismatched terminal bases are mixed, the gold nanoparticles precipitate and the solution loses its pink color. Unfortunately researchers were not able to use this technique with mismatched bases closer to the middle of the sequence.³⁸

Finally, some researchers are turning to spectroscopic approaches like Raman spectroscopy for non-destructive sensitive polymorphism detection. Raman spectroscopy is

a sensitive optical detection technique that can be combined with aspects of nanotechnology to provide even greater utility.²⁷ Functionalizing DNA with gold nanoparticles opens several avenues of pure DNA analysis and subsequent gene detection methodologies. Sun et al. have developed a way to detect breast cancer genes using the hybridization of sample DNA with probing DNA that has been modified with gold nanoparticles and specific Raman labels. Using this technique, Sun et al. were able to achieve detection sensitivities of down to 1 fM.²⁷ While much progress is being made,^{24, 39, 40} much has yet to be done to couple Raman techniques to the detection of SNPs.

1.3 Cell Monitoring

The chemical changes responsible for a stem cell's unique physiological capabilities have been explored through the use of various ingenious though often invasive techniques. Biological assays routinely used for stem cell analyses involve fixing, staining, and chemical drying – all of which interrupt the cell's natural life processes. These types of assays cannot provide real-time, continuous information but rather give a snapshot of a cell's condition. However, as stem cell research becomes increasingly relevant for new therapeutic and regenerative medicines, new research methods must be explored to facilitate real-time, non-destructive methods for cell characterization. Such non-destructive methods will enable the collection of high quality data with less experimental complexity and expense.

Raman spectroscopy has had a small though useful place in modern biological research since early protein experiments in 1970.^{7, 41} It is generally considered non-invasive, has the potential for continuously collecting data in real-time, and provides multiplexed chemical information that can be used to simultaneously explore covariant chemical relationships in complex environments. To date, Raman has been used to study bacteria,^{42, 43} viruses,⁴⁴ cancer,^{2, 27, 45, 46} brain tissue,³ cell cycle dynamics,⁴⁷⁻⁴⁹ embryonic stem cells,^{50, 51} and DNA hybridization⁵² though many of these experiments still involve invasive sample preparations. The non-invasive attributes of Raman spectroscopy, on the other hand, make it uniquely useful for monitoring cells as they undergoes a variety of transitions including growth, stress, differentiation, and death. Researchers have used Raman to study the biochemical changes of cells in different phases of the growth cycle⁴⁷ and to discriminate between healthy and tumor bone cells,⁵³ breast tissues,² and skin cells.⁵⁴ Other research has used Raman to explore Parkinsons' effects on brain tissues^{3, 50} and to follow differentiation in Murine embryonic stem cells.^{50, 55} More recent studies show that Raman can be used to monitor the in situ production of mineral matrix as mesenchymal stem cells (MSCs) differentiated into osteoblasts.^{56, 57}

1.4 Objectives

Given these strengths and an overall refinement of optical technology, Raman systems are uniquely suited for uses in sensitive chemical and biochemical detections and for

the exploration of some of biology and biomedicine's most pressing questions. This document presents a summary of my doctoral research. It discusses three specific objectives: 1) using molecular lithography to create enhanced spectroscopic substrates, 2) using surface enhanced Raman spectroscopy to detect single nucleotide polymorphisms and other genetic aberrations, and 3) using Raman spectroscopy to explore cellular chemistry – namely the chemical changes that occur as a human stem cell undergoes adipogenic differentiation.

1.4.1 Fabricating Raman enhancing solid-state nanogap sensors. In this objective, we use a combination of oligonucleotide-based molecular lithography and traditional photolithography to create finely tunable nanogap electrodes – planar electrodes with separations of just a few nanometers. Briefly, solid state nanogaps are created using a combination of conventional photolithography and a molecular lithography process similar to those already published.^{58, 59} However, in this study the molecular resists is created with single-stranded oligonucleotides (oligos) and enables rapid production of 10-30 nanometer separations between metallic features. Because oligos can be prepared quite inexpensively and tailored to many different sequences and sizes, an oligo molecular resist can be used to closely control the gap size (ie, the distance between conductors) from a few nanometers to several tens of nanometers. Solid state nanogaps represent an immediately relevant application of nanolithography. They can be used in extraordinarily sensitive chemical and biological detection schemes and are useful for an array of practical and academic pursuits.

These structures are invaluable for investigating molecular electronic candidates, for researching biological systems, and as a substrate for Raman spectroscopic studies. Here, as a proof of concept, the local molecular environment of the nanogap is monitored using Raman spectroscopy and current-voltage traces. The strong Raman enhancements created within the nanogap enabled spectroscopic detection of the addition, subtraction, and degradation of oligos within the nanogap.

1.4.2 Detecting and evaluating mid-sequence SNPs. In this objective we report that gold nanoparticles can be used in deoxyribonucleic acid (DNA) hybridization experiments to create a SERS environment around DNA of interest. With this set-up we are able to differentiate between DNA duplexes with and without mid-sequence base mismatches. The hybridized gold particles create a separation that is nominally controlled by the length of the oligos; typically moderate sized oligos are between 10 and 20 nm in length.⁶⁰ This fast and sensitive technique sidesteps the need for expensive polymerase chain reaction (PCR) or mass spectrometry based techniques and can be run with microfluidic devices or in array formats. Such an advance could make single nucleotide polymorphism (SNP) detection assays much more cost-effective, allowing for greater availability of research into cancer sub-typing, genetic disease mapping, and SNP-genotyping.

The methodologies discussed in this objective also potentially enable automated detection of SNP using Raman spectroscopy. Specifically, the SERS substrate and data

analysis rubric we have created facilitate the collection of statistically significant Raman data with a dramatically decreased degree of operator bias and the aberrant effects of Raman's usual heavy variability. The long-term benefit of such a system lies not only with its initial applications of manual detection but also with its enormous potential for automation and subsequent applications as previously mentioned.

1.4.3 Developing real-time cell monitoring systems. In this objective, human adipose derived adult stem (hADAS) cells are dosed with Au nanoparticles with the goal of providing information and insights into the progression of stem cells through an adipogenic differentiation pathway. HADAS cells are provided through an unfunded collaboration with Professor E. Lobo of the NC State/UNC Joint Department of Biomedical Engineering.

In addition to standard technological advances that have slowly been improving Raman capabilities, intracellular Raman work has been recently aided by the use of gold nanoparticles. Living cells naturally uptake gold nanoparticles in the fluid phase and transport these particles through an endosomal pathway. Once inside the endosome, nanoparticles aggregate into clusters that give rise to large spectroscopic enhancements that can be used to elucidate local chemical environments through the use of surface enhanced Raman spectroscopy. Thus far, relatively few papers have been written on the topic beyond proof of concept experiments though, and to the author's knowledge none have been reported on adipose derived stem cells. This objective uses 40 nm colloidal gold nanoparticles to

create volumes of surface-enhanced Raman scattering (SERS) within living hASCs enabling molecular information to be monitored. We exploit this technique to spectroscopically observe chemical changes that occur during the adipogenic differentiation of human adipose derived stem cells over a period of 22 days, monitoring both the production of lipids and the complex interplay between lipids, proteins, and chemical messengers involved in adipogenesis. Adipogenic differentiation is used here as a model system to explore the utility of SERS as a non-invasive in situ analysis method.

1.5 Dissertation Findings

The findings of this research have been shared at both scientific conferences and the publication of manuscripts to peer-reviewed journals. The manuscripts accepted, submitted, and in preparation are listed below along with miscellaneous related publications and presentations:

In Preparation

B Moody, A Brna, GS McCarty. Multidimensional Interpretation Using Surface Enhanced Raman Analysis of Nucleotide Polymorphisms

Submitted

B Moody, CM Haslauer, E Kirk, EG Lobo, GS McCarty. In Situ monitoring of adipogenesis with human adipose derived stem cells using surface enhanced Raman spectroscopy.

Peer-Reviewed Publications

B Moody, J Leotaud, GS McCarty. Using Surface Enhanced Raman Spectroscopy to Probe for Genetic Markers on Single Stranded DNA. *Journal of Biomedical Optics*, 2010

GS McCarty, B Moody, M Zachek. Enhancing Electrochemical Detection by Scaling Solid State Nanogaps. *The Journal of Electroanalytical Chemistry*, 2010

JG Roberts, B Moody, GS McCarty, LA Sombers. Investigating Surface Transformations Induced by Electrochemical Pretreatment at Carbon Fiber Microelectrodes. (In press, *Langmuir* 2010)

M Zachek, P Takmakov, B Moody, RM Wightman, G McCarty. Simultaneous Decoupled Detection of Dopamine and Oxygen using Pyrolyzed Carbon Microarrays and FSCV. *Analytical Chemistry*, 2009

B Moody, GS McCarty. Solid state nanogaps for differential measurements of molecular properties. *Applied Physics Letters*, 2009

B Moody, G McCarty. Statistically Significant Raman Detection of Midsequence Single Nucleotide Polymorphisms. *Analytical Chemistry*, 2009

Book Chapters

B Moody, M Zachek, GS McCarty. Devices and Sensors for Bioelectric Monitoring and Stimulation; Irudayaraj, Joseph, Ed.; (In preparation)

B Moody, GS McCarty. Nanolithographic Techniques in Tissue Engineering. In Nanotechnology and Tissue Engineering: The Scaffold; Laurencin, K. T., Nair, L. S., Eds.; CRC Press: 2008; pp 261.

Conference Presentations

B Moody, GS McCarty. Using Surface Enhanced Raman Spectroscopy to Detect Mid-Sequence Single Nucleotide Polymorphisms. 60th Pittsburgh Conference on Analytical Chemistry and Applied Spectroscopy, Chicago, IL, March 8-13, 2009.

B Moody, CM Haslauer, E Kirk, EG Lobo, GS McCarty. Analysis of Adipose Derived Adult Stem Cell Differentiation with Surface Enhanced Raman Spectroscopy. 61th Pittsburgh Conference on Analytical Chemistry and Applied Spectroscopy, Orlando, FL, February 28 – March 5, 2010.

Chapter 2: Solid State Nanogaps for Differential Measurements of Molecular Properties

This chapter demonstrates the production and probing of extremely small separations between metal conductors, separations referred to as solid state nanogaps. These nanogaps can be inexpensively and controllably produced using a combination of molecular and standard photolithography. In this chapter these nanogaps are implemented for monitoring by using two detection schemes, one optical and one electronic. Specifically, the enhancement principles from surface enhanced Raman spectroscopy are used to collect molecular information about the species in the nanogap and current-voltage traces are collected to probe the charge transport of the nanogap. These data show that the oligonucleotides used as the molecular resist are degraded during processing, that some of the degraded oligonucleotides are removed, and that fresh oligonucleotides are adsorbed.

2.1 Introduction

Solid state nanogaps are scientifically interesting due to their small size, robustness, and versatility. Many insights in physics at the nanometer scale have been made using these types of structures and more are expected in the future.⁶¹⁻⁶³ Practically, solid state nanogaps have the potential of detecting chemical species on the near single-molecule scale.

Disciplines that stand to benefit from robust, sensitive, and inexpensive detection devices extend from practical applications of medical screening and explosives detection to more academic pursuits such as researching the fundamentals of charge transport and molecular binding events.

Coincidentally, surface enhanced Raman spectroscopy (SERS) also stands to benefit from the maturation of nanogap technologies. SERS is a variant of Raman spectroscopy that uses roughened metallic substrates to enhance, amplify, and otherwise refine its output signal. However, the difficulty that frequently arises with SERS is creating substrates that have large and very uniform enhancement factors. Ideally SERS substrates should be efficiently and inexpensively fabricated on the wafer scale and will consist of small metallic structures with uniform spacing from a few hundred nanometers to just a few nanometers. More routinely, however, SERS substrates are subject to local unpredictable “hot spots” of enhancement and require advanced nanolithographic patterning to prepare.²¹⁻²³ Research is beginning to show that the closely spaced metal features at the nanogap are also capable of

enhancing the Raman effect.^{25, 26, 64} Such discoveries lead to the possibility of using nanogaps for dual function applications – to serve as an electronic detection device and as a SERS platform for chemical characterization. However, making a nanogap with the exact spacing can be difficult, especially with a large wafer-scale production. Fortunately, molecular lithographies can aid in this process.

In the past nanogap structures have been fabricated with mechanically controlled break junctions,^{65, 66} nanowire lithography,⁶⁷ and electron beam lithography with electromigration^{25, 68} among others.⁶¹ Each method has its own individual advantages and disadvantages though very few offer both the promise of nanoscopic gap-size control and the likelihood of wafer-scale fabrication efficiency. In this project, emphasis will be placed on using a hybrid molecular technique to create planar electrodes with separations of about 20 nanometers. In the future these structures will be invaluable for investigating molecular electronic candidates, for researching biological systems, and as a substrate for SERS studies. Here, as a proof of concept experiment, the local molecular environment of the nanogap is monitored using SERS and current-voltage traces immediately after fabrication, then again after an alkanethiol substitution, and finally after a subsequent oligo substitution.

2.2 Materials and Methods

2.2.1 Electrodes/Nanogap fabrication. Solid state nanogaps are generated using a variation of previously developed molecular resist strategies.⁵⁸ These strategies have demonstrated the ability to use multilayer resists to create structures from just a few nanometers to ~40 nm.⁵⁹ The structures presented here are different in several ways from previous alkanethiol-based solid state nanogaps in that these structures are created with thicker single layer molecular resists and they maintained the capping metallic layer often sacrificed in other papers.

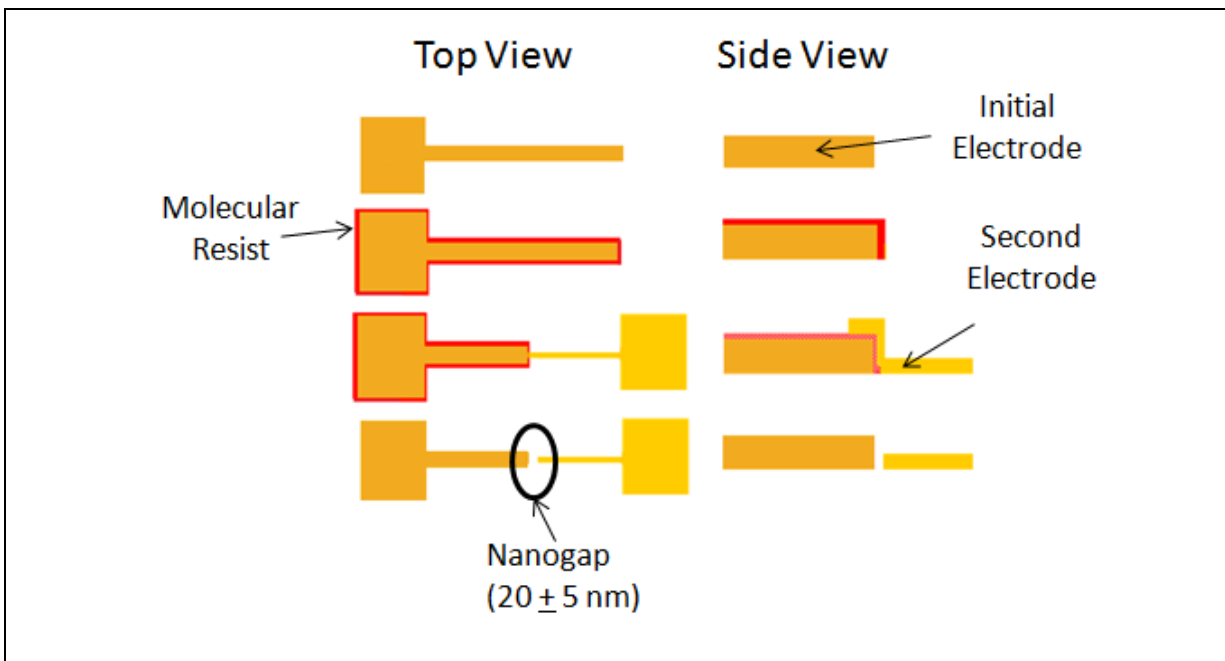


Figure 2.1. Schematic showing the process of hybrid molecular lithography.

The hybrid fabrication methodology for these structures is shown schematically in Figure 2.1 and will be briefly explained. In this report, the initial electrode in the electrode pair that composes the nanogap is fabricated on a silicon wafer with 200 nm of silicon oxide (University Wafer) using a conventional photolithography lift-off process with SPR3012 (Rohm&Haas) and LOR5A (MicroChem) resists and then 3 nm of chrome and 40 nm of gold are deposited using electron beam evaporation. The photoresist and unwanted metal are removed with sonication in acetone and an immersion in CD-26 (MicroChem). Next, the electrode is submerged in 5 μ M solution of thiolated oligonucleotide (IDT) for 24 hrs. Finally, a second photolithographic lift-off process, metallic evaporation and resist removal are used to pattern the second electrode in the electrode pair. These processes were similar to those used to pattern the initial electrode except 3 nm of chrome and 25 nm of gold were deposited. The oligo resist had the sequence 5' – T₁₀ – GC AGC TTA GAA TCA AAT AGC GCG ATA TGC ATC GAT GAC TA – 3' and a thiol modification at the 5' terminus. Research suggests an oligo this size should be about ~20 nm in length.⁶⁰ Scanning electron microscope (SEM) images were collected to characterize the electrode fabrication process (data not shown) and image analysis confirms that the size of the nanogap is within the expected range of 20 ± 5 nm.

2.2.2 Raman Spectroscopy. All Raman spectra presented in this paper were collected with a custom built Raman microscope. Raman scattering was excited using a 12 mW, 632.8

nm HeNe laser (Thorlabs) coupled to an inverted microscope (Nikon, Diaphot) with a 100x (Nikon) dry objective. The reflected Raman signal was analyzed through an imaging spectrograph (PI Acton, SpectraPro SP-2156) and detected with a liquid nitrogen cooled CCD camera (PI Acton, Spec-10:100BR/LN). The laser power at the sample measured 3 mW and the laser spot was $\sim 2 \mu\text{m}$ in diameter. Collection times were 20 s. GRAMS/AI 8.0 software (Thermo) was used for analysis and correction.

The electronic properties of the nanogap were also collected as they provide a quick, qualitative measure of variation at the nanogap. While electronic property measurements are fast and inexpensive they provide little molecular information. For this reason surface enhanced Raman spectroscopy was also performed. The electronic properties and Raman spectra for these structures were recorded at three time points during the experiment: 1) immediately after fabrication, 2) after substitution of dodecanethiol into the gap, and 3) after immersion in a 50-mer thiol terminated oligonucleotide. Note that the Raman information was collected in a confocal format at the nanogap enabling the data to be collected from nominally the same position during each step of the experiment.

2.3 Results and Discussion

Figure 2.2 shows portions of the Raman spectra from a representative solid state nanogap and Figure 2.3 shows the current voltage traces for the same solid state nanogap at the same time points. The dark blue trace in Figure 2.2 shows the as fabricated condition. Note that while spectra recorded away from the nanogap show little signal or perhaps small contributions from the Si substrate (data not shown), the portion of the spectrum from the nanogap shown in Figure 2.2 has two strong peaks at 1342 and 1585 relative cm^{-1} . These peaks are very similar to those observed in pyrolyzed photoresist or for glassy carbon with two strong bands around 1360 relative cm^{-1} (Disordered (D) band) and 1600 relative cm^{-1} (Graphitic (G) band).^{69, 70} These features alone are typical of sp^2 bonding within a graphitic carbon matrix whereas oligo systems typically have several additional characteristic peaks present.^{24, 71} This suggests that some of the oligonucleotide being used as a molecular resist degraded during the fabrication process. The dark blue trace in Figure 2.3 shows the electronic properties of the as fabricated nanogap. Through SEM imaging the separation of the nanogap was observed to be ~ 20 nm with a roughness on the order of 5 nm. At this length scale no charge transport is expected from ballistic tunneling⁵⁸ but as can be seen in the current voltage trace, significant charge transport was observed for this system. It is expected that this charge transport was through the oligos or through the degraded oligos which appear graphitic from the molecular information collected by Raman spectroscopy.

Note that oligonucleotides and DNA once thought to be insulators have since been shown to enable long range charge transfer when dry, though the exact mechanism is still debated.^{72, 73}

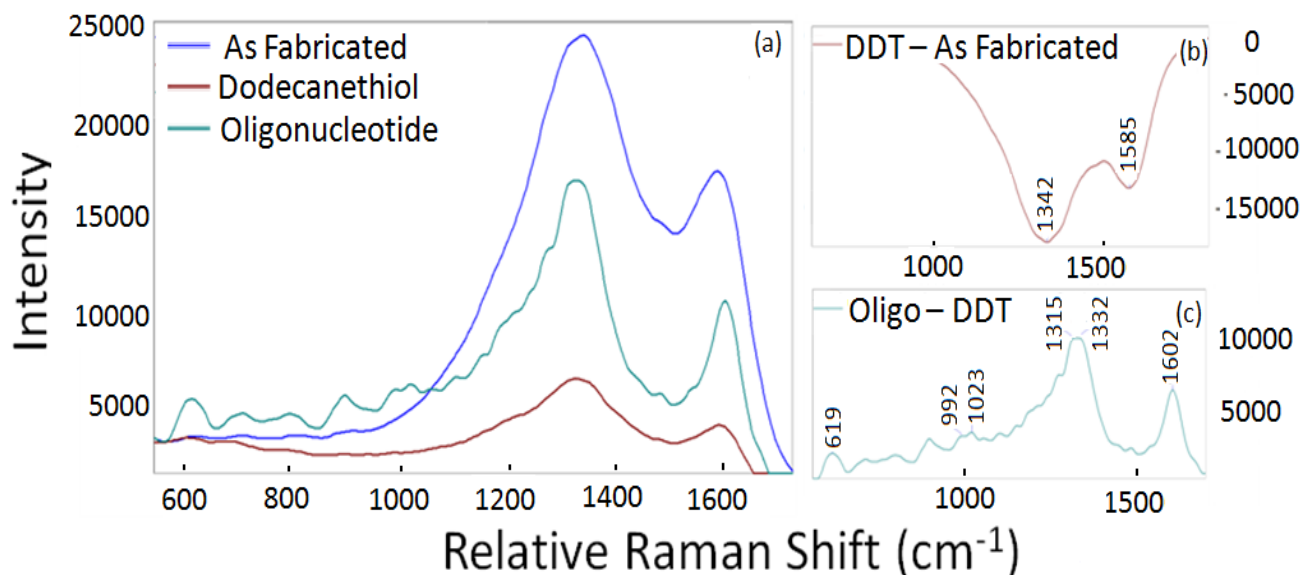


Figure 2.2. Raman signal from a nanogap created using single-stranded oligonucleotides as a molecular resist in the structure's fabrication. Figure 2.2a shows a portion of the Raman spectra collected at the electrode interface as fabricated, after a dodecanethiol (DDT) substitution, and then after thiol functionalized oligonucleotides (Oligos) were added to the solid state nanogap. Figures 2.2b and 2.2c are the spectra that result from subtracting the As Fabricated trace from the Dodecanethiol trace and from subtracting the Dodecanethiol trace from the Oligonucleotide trace, respectively. These latter spectra are used to highlight the change in condition between two states.

In an effort to remove some of the degraded oligonucleotide, the sample was immersed in a solution of 1 mM dodecanethiol (DDT) in ethanol and heated to 60°C for one hour. The sample was then slowly returned to room temperature over several hours. Then the Raman spectrum and electronic properties of the *same* nanogap were collected again.

The results are shown in the brown trace of Figure 2.2 for Raman spectroscopy and the brown current voltage traces in Figure 2.3. Experiments in our lab have not shown significant characteristic SERS scattering from dodecanethiol. The lack of SERS signal from DDT was expected since Raman activity is enhanced in molecules with some π -bonding or with large cross-sectional areas.^{74, 75} Thus,

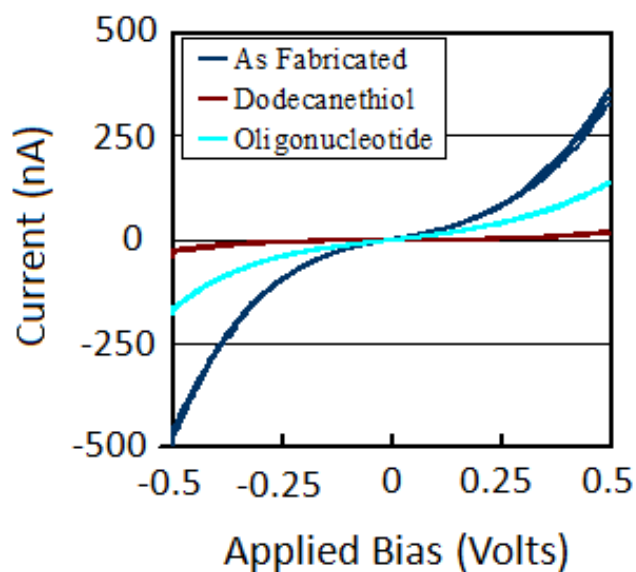


Figure 2.3. Current – voltage characteristics for the electrode as fabricated, after the dodecanethiol substitution, and then again after the final oligonucleotide addition. The electrode conducted 350 nA as fabricated, 18 nA after the alkane substitution, and 130 nA after the oligo substitution, all at +0.5 V of applied bias.

because dodecanethiol is a straight chain, sp^3 hybridized system, a great reduction in Raman activity is expected when it is used to replace the more complex and aromatic, π -bonded environment of the oligonucleotide system. From Figure 2.2 it can be seen that Raman activity indeed dropped significantly after the alkanethiol substitution, including activity from the graphitic peaks. This point is highlighted specifically by subtracting the “As Fabricated” trace from the “Dodecanethiol” trace. The resulting Figure 2.2b shows large negative peaks at 1342 and 1585 cm^{-1} that have been attributed to the D and G bands of carbon.^{69, 70} In Figure 2.3 a significant reduction in the charge transfer through the nanogap is also shown. It can be deduced from this information that some (though not all) of the degraded oligonucleotide has been removed from the solid state nanogap. Repeated aggressive sonication in strong solvents like dimethylformamide (DMF) can be used to remove more of the molecular species at the nanogaps, resulting in a Raman spectrum that is featureless except for a small peak at 530 cm^{-1} that represents the silicon substrate. Unfortunately, this process is time consuming and its adverse effects to the electrodes limit overall device yield.

Finally, the alkanethiol-substituted oligo sample was immersed in a 5 μM aqueous solution of thiol modified 50-mer oligonucleotide and heated to 60°C for one hour. The sample was removed, rinsed, and the electronic and Raman spectrum were again recorded and are shown as green traces in Figures 2.2 and 2.3. The conductivity of the sample

increased while still remaining non-linear with respect to applied voltage (see Figure 2.3). Figure 2.2c shows the Raman spectrum created by subtracting the “Oligonucleotide” spectrum from the “Dodecanethiol” spectrum. The resultant spectrum shows characteristic nucleic acid peaks for cytosine (at 619, 1023 cm^{-1}),⁷⁶ adenine (at 1332 cm^{-1}),⁷⁷ thymine (at 992 cm^{-1}),⁷⁶ and guanine (at 1315, 1602 cm^{-1}).⁷⁷ This information verifies that some oligonucleotide was added to the solid state nanogap. It is expected that this corresponds to a significant Raman enhancement factor. Unfortunately, to date Raman spectra for single stranded oligonucleotide is notoriously difficult to obtain⁷⁸ and by our hands none have been collected on other substrates for comparison. Notice also that while all conditions share similar peaks in the range of the sp^2 bands, besides the additional peaks below 1200 relative wavenumbers, the oligo sample exhibits a significant shift of the 1342 cm^{-1} peak to lower wavenumbers and a shift of the 1585 cm^{-1} peak to higher wavenumbers. This can be observed easily in Figure 2.2c. It is hypothesized that these features are due to the convolution of peaks from the remaining degraded oligonucleotide from the fabrication process and some overlapping peaks from the added oligonucleotide. It is expected that the shifts predominantly indicate the presence of C-N stretching and NH_2 deformations, respectively.^{24, 71}

2.4 Conclusion

The probing of electronic and optical properties for nanogaps created using a combination of oligo-based molecular lithography and conventional photolithography has been shown. Because of the advanced state of common oligonucleotide preparation techniques, theoretically the oligonucleotide length and thus a single layer molecular resist thickness can be easily tailored to size specifications from just a few nanometers up to realistically tens of nanometers. These nanogaps are not only capable of sensitive electronic detection for quickly and inexpensively probing charge transfer at the nanogap, but may also be analyzed for molecular information using SERS.

Chapter 3: Statistically Significant Raman Detection of Mid-Sequence Single Nucleotide Polymorphisms

This chapter highlights methodologies that enable statistically significant data to be collected for single nucleotide polymorphisms using surface enhanced Raman spectroscopy. Single-stranded oligonucleotides functionalized with 40 nm gold nanoparticles are hybridized with oligonucleotides adsorbed to a photolithographically defined gold surface thus creating a surface enhanced Raman environment around the DNA duplex. With this design characteristic Raman spectra have been collected and explored for differences between DNA duplexes formed from complementary oligonucleotides, completely mismatched oligonucleotides, and those formed from oligonucleotides that have a mid-sequence single nucleotide mismatch. The results show that statistically significant differences in Raman intensity for characteristic peaks can be collected for the three cases.

3.1 Introduction

Currently, there are a variety of different schemes used in SNP detection,³⁶ however, nearly all require a polymerase chain reaction step⁷⁹ in order to produce enough enriched source material for analysis. Though it does provide good specificity and sensitivity,⁸⁰ PCR is known for being difficult to integrate into the sequence analysis processes used for SNP detection and is often cited as a major limitation to throughput in SNP genotyping assays.⁸¹ As an alternative to PCR-based analysis, some researchers are exploring nanotechnology for SNP detection. A recent innovation using DNA functionalized with gold nanoparticles shows that DNA/nanoparticle solutions with mismatched terminal bases will precipitate and lose color when mixed.³⁸

Others are turning to spectroscopic approaches like Raman spectroscopy for non-destructive sensitive detection. Raman spectroscopy is a sensitive detection technique that has the potential of reducing the need for PCR. While innately weak Raman signals, fluorescence, and large background noise can make biological Raman applications difficult, advances in laser and filter technology and the advent of surface enhanced Raman spectroscopy (SERS) have improved Raman capabilities. Further, combinations of Raman spectroscopy with aspects of nanotechnology provide even greater utility²⁷. Functionalizing DNA with gold nanoparticles opens several avenues of pure DNA analysis and subsequent gene detection methodologies. Sun et al. have developed a way to detect breast cancer genes

using the hybridization of sample DNA with probing DNA that has been modified with gold nanoparticles and specific Raman labels. Using this technique, Sun et al. were able to achieve detection sensitivities of down to 1 fM²⁷. While much progress is being made,^{24, 39,}⁴⁰ much has yet to be done to couple Raman techniques to the detection of SNPs.

Surface enhanced Raman spectroscopy (SERS) is a spectroscopic technique that amplifies and improves Raman signal within a very localized vicinity, generally around two closely spaced metal structures. In general SERS is inexpensive, relatively fast, and vastly increases detection sensitivity. A major difficulty hampering SERS analysis, however, is sample-to-sample variability. SERS analyses especially are adversely affected by the existence of so-called “hot-spots” – a substrate-based phenomenon that can result in data that is uncharacteristic of the system under study and causes large sample-to-sample variations that can hinder statistically significant differential analyses.^{21, 24} In this chapter we focus on experimental set-up and SERS substrate preparations along with simple data processing techniques in order to acquire statistically meaningful Raman data. As a proof of concept, this method is used to monitor deoxyribonucleic acid (DNA) hybridizations and to detect mid-sequence single nucleotide polymorphisms (SNPs).

DNA in general and specifically SNP systems are both biologically important and experimentally robust and therefore make for good model systems. By definition, if the appropriate nucleotide in a single base of DNA is replaced by another nucleotide with a

frequency greater than 1%,²⁹ the mutation is classified as a single nucleotide polymorphism.³⁰ On a molecular level, polymorphisms can alter protein function, affect DNA repair, encourage genetic instability, and promote cancer.³³ Studies suggest that SNPs account for 90% of polymorphisms²⁹ in the human genome and have been associated with breast, lung, head, and neck cancers among others.³⁵ As genetic markers SNPs are being used for mapping conditions as diverse as diabetes, multiple sclerosis, and obesity.³⁰

The methodologies reported in this paper enable automated statistically significant detection of SNP using Raman spectroscopy. Specifically, gold nanoparticles in conjunction with photolithographically created gold substrates can be used in DNA hybridization experiments to create a SERS environment around DNA of interest. With this configuration a separation between gold surfaces that is nominally controlled by the length of the oligos (typically moderate sized oligos are between 10 and 20 nm in length⁶⁰) is created to enhance the Raman effect and enable differentiation between DNA duplexes with and without mid-sequence base mismatches.

3.2 Materials and Methods

As seen schematically in Figure 3.1 the overall idea is to adsorb single stranded oligonucleotides (50-mers in length) to gold nanoparticles in aqueous solution and then place these solutions on noble metal features that are functionalized with either complementary, non-complementary, or complementary except for a single mismatched base oligonucleotides. After several hours the samples are rinsed and Raman spectra collected. The scheme involves five main steps: 1) photolithographically preparing the substrate with gold features, 2) functionalizing the nanoparticles with “target” oligonucleotides, 3) functionalizing the substrate with “capture” oligonucleotides, 4) hybridization of the oligo/nanoparticle solution with the substrate, and 5) Raman analysis.

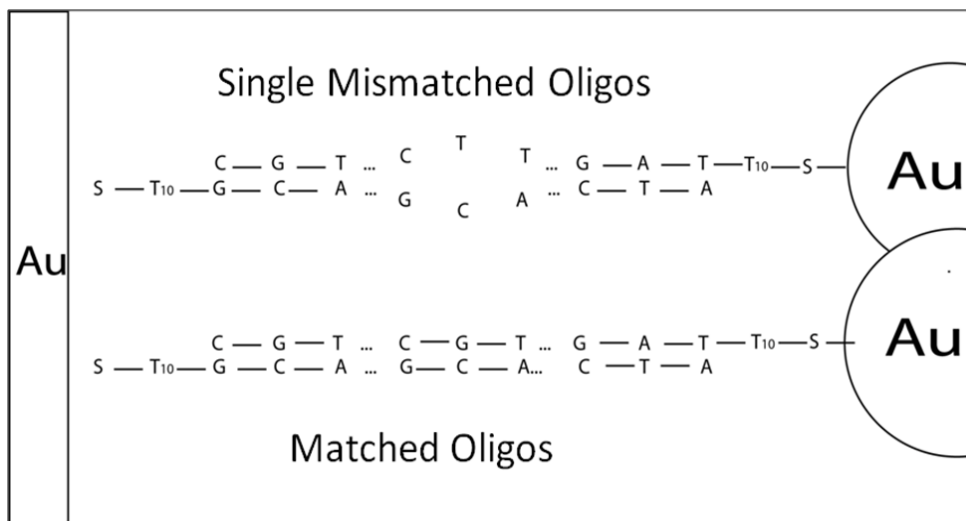


Figure 3.1. Visualization of the hybridization scheme used to create a SERS environment around DNA duplexes.

3.2.1. Substrate Preparation 1. Through a combination of photolithography and electron beam deposition, a quartz wafer (SiliconQuest) was prepared and patterned with ~2-3 μm diameter circular gold spots (400 nm Au on 30 nm Chrome) situated in arrays of 20 spots per array. The spots are placed in five rows of four spots with each spot distanced 5 μm from its nearest neighbor. The wafer was treated with 30% w/w peroxide for 1 hr immediately prior to spotting in order to clean the surface.

3.2.2 Oligo Preparation 1 (Capture Strands). All oligos were purchased from IDT as 40 mer sequences supplemented with 10 thymine bases (T_{10}) on the 5' end for a total of 50 bases. The T_{10} section is intended to act as a spacer between the gold surfaces and the actual sequence thereby reducing non-specific binding and improving hybridization.^{27, 82} In addition, each oligos was also designed with a 5' thiol modification and was purified with a standard desalt during manufacturing.

Dry DNA (from IDT) was first suspended in 1xTE buffer solution, pH 7.5 (IDT), then reduced by adding Reductacryl (Calbiochem) at a ratio of 1 mg oligo to 50 mg Reductacryl. The reduced solution was agitated for 30 minutes, filtered through a 0.22 μm filter (Fisher), and then used to prepare a 1 μM solution in the IDTE buffer. This solution was spotted onto the dry micropatterned metal arrays on the quartz wafer which was then placed in a humid environment and incubated for 6 hrs at room temperature.

50 mer oligonucleotides with 5' thiol modifications were used as capture strands. Two nearly identical sequences differing by only three bases around the site of mismatch were run for comparison. Capture strands for the first sequence, or the C-T sequence, had the sequence: 5'- Thiol – T₁₀ – GC AGC TTA GAA TCG – C – ATA GCG CGA TAT GCA TCG ATG ACTA – 3'. Capture strands for the second sequence, named the A-G sequence, had a slightly altered sequence: 5'- Thiol – T₁₀ – GC AGC TTA GAA TCA – A – ATA GCG CGA TAT GCA TCG ATG ACTA – 3'.

3.2.3 Substrate Preparation 2. After incubation with capture strands, the wafer was rinsed by multiple submersions in DI water and dried under nitrogen. Then the wafer was spotted with a 1 mM solution of mercapto-1-hexanol (MHOH) (Sigma) to further reduce non-specific binding.^{27, 83} The wafer was then allowed to sit overnight (~17 hrs) after which the MHOH was rinsed with DI water by immersion and dried under compressed air.

3.2.4 Oligo Preparation 2 (Target Strands). Concentrated gold nanoparticle solutions were prepared by centrifuging 6 mL of 40 nm diameter gold nanoparticles (Ted Pella) at 6000 rpm for 20 min and collecting the precipitate. Target oligo solutions were prepared by first reducing the target strands with Reductacryl using the same procedure as with capture strands and then adding them to the concentrated gold nanoparticle solutions. After 24 hrs, the gold/oligo solution was brought to 1 μ M in 10 mM pH 7.5 phosphate buffer/tween solution (PB/T). After 30 minutes the target solution was salted by 5 additions

of 15 μL 4 M NaCl with vigorous mixing in between additions. After \sim 48 hrs, the target solutions were washed in PB/T with 0.3 M NaCl twice by centrifugation (8000 rpm, 20 min) and redispersing sonications and brought up in the same solution.

Target strands were deemed complementary (matched), single mismatched, or non-complementary (completely mismatched) as described in Table 3.1. To explore the robustness of the procedure and the effect of different sequences on the results, two different DNA sequences were used – one sequence designed to have a guanine-adenine mismatch and another designed to have a cytosine-thymine mismatch. All mismatches were placed at the fifteenth base position from the 5' terminal. Procedure for functionalization with gold nanoparticles and hybridization with capture strands is similar to that developed by Sun et al. with some variations.²⁷

3.2.5 Hybridization. Target strands were spotted onto the dry capture strand arrays prepared above, again put in a humid environment, and incubated at 40°C for 4 hrs. The wafer was then rinsed with 10 mM PB/T and immersion rinsed in DI water and dried with nitrogen. Finally, the wafer was soaked in Silver Enhance (Ted Pella) solution for 10 min, rinsed and dried again, and immediately analyzed with Raman under room conditions. Further water rinses after 24 hrs did not seem to have an effect on the Raman signal.

3.2.6 Raman Detection. Raman scattering was excited using a 12 mW red HeNe laser (Thorlabs) coupled to an inverted microscope (Nikon, Diaphot) with a 60x dry objective

(Olympus). The reflected Raman signal was analyzed through an imaging spectrograph (PI Acton, SpectraPro SP-2156) and detected with a liquid nitrogen cooled CCD camera (PI Acton, Spec-10:100BR/LN). The laser power at the sample measured 3 mW and the laser spot was about $\sim 2 \mu\text{m}$ in diameter. Collection times were 20 s. GRAMS/AI 8.0 software (Thermo) was used to average the spectra and for baseline correction.

Table 3.1 Oligonucleotide Design for A-G and C-T Oligo Sequences

A-G Sequence	
Complementary	5' - Thiol – T ₁₀ – TAGT CAT CGA TGC ATA TCG CGC TAT – T – TGA TTC TAA GCT GC – 3'
Single Mismatch	5' - Thiol – T ₁₀ – TAGT CAT CGA TGC ATA TCG CGC TAT – G – TGA TTC TAA GCT GC – 3'
Non-Complementary	5' - Thiol – T ₁₀ – GC AGC TTA GAA TCA – A – ATA GCG CGA TAT GCA TCG ATG ACTA – 3'
C-T Sequence	
Complementary	5' - Thiol – T ₁₀ – TAGT CAT CGA TGC ATA TCG CGC TAT – G – CGA TTC TAA GCT GC – 3'
Single Mismatch	5' - Thiol – T ₁₀ – TAGT CAT CGA TGC ATA TCG CGC TAT – T – CGA TTC TAA GCT GC – 3'
Non-Complementary	5' - Thiol – T ₁₀ – GC AGC TTA GAA TCG – C – ATA GCG CGA TAT GCA TCG ATG ACTA – 3'

3.3 Results and Discussion

This chapter describes efforts to create a statistically robust method for using Raman spectroscopy to explore the hybridization of oligo-modified nanoparticles and determine the feasibility of using this type of approach for SNP detection. The proposed mechanism behind these experiments is that mismatched DNA will not bind as strongly as matched DNA and will be more susceptible to removal through stringent washes. Therefore, mismatched samples will have fewer hybridization events and less overall Raman signal. Differences between matched and mismatched spectra are determined by examining four different peaks that are characteristic for the oligonucleotides.

Several experimental considerations were implemented in an effort to reduce ambiguity of the Raman data. Defined gold substrates were created from arrays of small (~2 μm diameter) photolithographically fabricated features. Electron beam deposition was used to deposit Au on the photolithographically defined features giving good control of substrate parameters like surface area, thickness, and roughness, effectively decreasing the impact of substrate variations and improving data quality. The size of the features ensured that the entire feature and very little surrounding area was illuminated by the focused laser spot during Raman analysis and the defined feature locations enabled easy analysis by scanning electron microscopy. Gold substrates were thus used as easily fabricated and highly repeatable substrates upon which a Raman enhancement could be generated primarily by

nanoparticle–substrate interactions. Future efforts will examine substrates to increase Raman enhancement factors.

Effects of anomalous feature interactions are also diminished by simple data processing. Eight random spectra were collected from three 20-spot arrays for each sample type – perfect match, single mismatch and complete mismatch. This resulted in the collection of twenty-four spectra for each configuration. Data were smoothed and baseline corrected by subtracting an offset. Note that the offset was a straight line from the local minimum (created by the laser line notch filter) in the spectrum at ~200 relative wavenumbers to the local minimum at ~2000 relative wavenumbers (past the region of observed Raman peaks). The “rubber band” method was not used for baseline correction as its human input makes it more susceptible to the artificial generation of statistically significant data. Subsets of the six spectra closest to the median were then selected from each group in order to eliminate both high and low outliers. Finally, the subsets were averaged to determine overall intensity differences for plotting and the intensities of characteristic nucleic acid peaks were extracted for statistical analysis.

As a result hybridized spots for both sequences show a visible and statistically significant difference (from $p < 0.05$ to $p < 0.001$) in overall peak intensities between matched and single mismatched samples. As seen in Figure 3.2, matched samples have the greatest

average intensity, single mismatched samples have less, and completely mismatched samples have almost none.

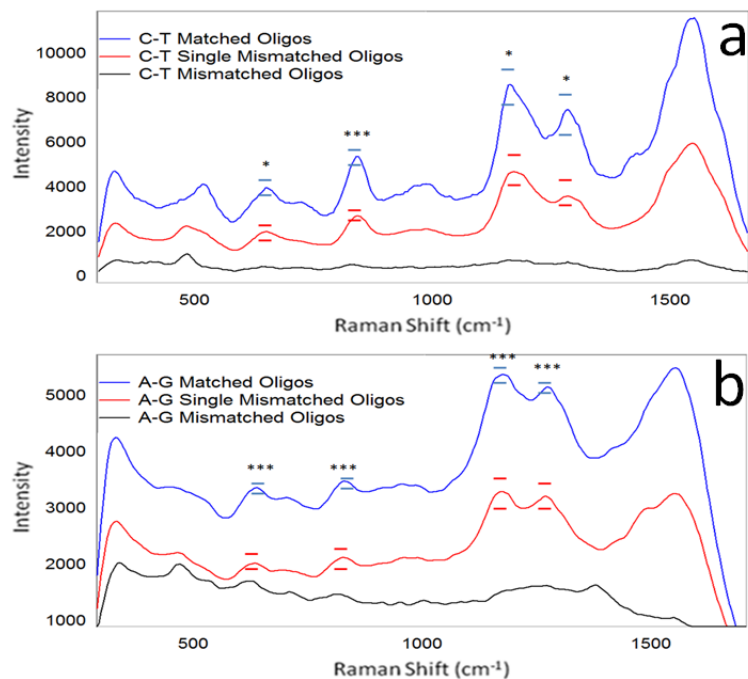


Figure 3.2. Raman spectra comparing the averaged median intensities of single-stranded oligos (matched, mismatched, and single-mismatched) hybridized to form double-stranded duplexes using the a) C-T and b) A-G sequences. Standard error bars are included for key peaks along with asterisks that indicate the level of statistical difference.

T-tests were applied to four peaks of interest within each sequence. For the C-T sequence these peaks included the guanine ring breathing at 650 cm⁻¹,^{76,77} the phosphodiester backbone peak at 841 cm⁻¹,⁷⁷ a guanine stretch at 1170 cm⁻¹,^{71,76} and

guanine/thymine vibrations at 1285 cm^{-1} .⁷⁶ Statistically significant peaks in the A-G sequence include thymine/adenine modes at 635 cm^{-1} ,^{76,77} the backbone peak at 831 cm^{-1} ,^{77,84,85} adenine/guanine stretches at 1179 cm^{-1} ,⁷¹ and guanine/thymine stretches at 1275 cm^{-1} .^{76,77} Figure 3.2 more succinctly shows the peak positions, level of significance, and standard error of these key peaks. Note that among all these peaks, the matched samples consistently show at least a 37% increase over the single mismatched samples.

An SEM analysis (data not shown) further supports the theory that more nucleotides are being hybridized in complementary samples than in single-mismatched samples. Images show greater surface area coverage of nanoparticles on the gold spot with complementary oligos, a reduced amount on the spot with single-mismatched oligos, and almost no particles on the completely mismatched sample. These images give additional confirmation on the number of strands that are hybridizing and on how representative the Raman signal is of hybridization events. Presumably this technique could be advanced to a point that would enable a correlation between particle counts/surface area coverage and Raman intensity.

3.4 Conclusions

A preliminary method capable of generating statistically significant data for detecting mid-sequence SNPs is reported in this work. Combining the virtues of photolithography, surface enhanced Raman spectroscopy, and comparatively simple surface chemistry techniques, the process is also inexpensive and relatively fast. The merits of our technique, while here focused on the specific problem of SNP detection, contain underlying methodologies that are generally applicable to a host of Raman applications.

Chapter 4: Using Surface Enhanced Raman Spectroscopy to Probe for Genetic Markers on Single Stranded DNA

Methods capable of quickly and inexpensively collecting genetic information are of increasing importance. In this chapter we report a method of using surface enhanced Raman spectroscopy to probe single stranded DNA for genetic markers. This unique approach is used to analyze unmodified genes of moderate length for genetic markers by hybridizing native test oligonucleotides into a surface enhanced Raman complex, vastly increasing detection sensitivity as compared to traditional Raman spectroscopy. The Raman complex is formed by sandwiching the test DNA between 40 nm gold nanoparticles and a photolithographically defined gold surface. With this design we are able to collect characteristic Raman spectra about the test DNA and to detect genetic markers such as single-nucleotide polymorphisms and polymorphic regions. Results show that strands containing one of three different types of polymorphism can be differentiated using statistically significant peak position differences and trends regarding Raman intensity.

4.1 Introduction

The detection of genetic markers has become ubiquitous in modern scientific research as a tool for examining the genetic relationships that underpin traits involving heredity, biological variability, disease susceptibility, and pharmacological efficacy to name a few. Because DNA sequence variations and base mismatches such as single nucleotide polymorphisms (SNPs) have been associated with approximately 90% of polymorphisms in the human genome,²⁹ researcher often use SNPs as markers for a variety of genetic diseases,³⁰ cancers,³⁵ and miscellaneous genetic curiosities.

The importance of improving the speed, specificity, and cost-efficiency of methodologies used to collect genetic information directly correlates with the importance of the information itself. Though polymorphisms as genetic markers are traditionally probed using time-intensive Southern blot hybridizations and polymerase chain reaction (PCR) related methodologies,⁷⁹ previously mentioned innovations using DNA functionalized with gold nanoparticles (AuNPs) have made preliminary steps in detecting terminal DNA mismatches.³⁸ Unfortunately researchers were not able to use this technique with mismatched bases closer to the middle of the sequence and the test DNA had to be modified to attach the nanoparticles.³⁸

Raman spectroscopy is another sensitive detection technique that has the potential of reducing the need for PCR and laborious biochemical techniques. Since the early 1970's

researchers have been using Raman to explore nearly every aspect of biology and biomedicine⁸⁶ - including DNA.⁸⁷ Combining gold nanoparticle-based SERS with DNA opens several avenues of pure DNA analysis and subsequent gene detection methodologies.

Previous results from our lab used SERS to detect, with high levels of statistical confidence, differences between samples of complementary oligos and those formed from oligos with a mid-sequence base mismatch.⁵² However, a major drawback to the practical and clinical applicability of this technology is the need to add thiol modifications to each different oligo intended for analysis. Not only is it expensive to add thiol modifications to numerous target strands, the variability associated with the surface chemistry involved in functionalizing a large variety of oligonucleotides with gold nanoparticles gives rise to assorted degrees of clumping, precipitation, poor adsorption and other deleterious interactions with the gold nanoparticles. We have found that using a single modified target oligo to test for multiple mutations reduces sample-to-sample variability, decreases the amount of preparation time, and decreases the need for costly reagents and modified DNA material.

In this chapter we refine and expand previous techniques to further investigate the technology's potential for genetic marker detection and to make the technology more applicable to biological studies. Namely, we have eliminated the need to tag the test oligo with gold nanoparticles and we have expanded the capabilities of this technology to detect

and explore two different types of polymorphic regions (PRs) in addition to lone SNP detection. The enhanced ability to test for multiple mutations along a native, unmodified gene broadens the applicability of this technique to practical genetic marker detection methodologies.

4.2 Materials and Methods

The overall idea is to capture single stranded “test” oligonucleotides between closely spaced gold features. As depicted in Figure 4.1, a DNA test strand can be probed for abnormal base mutations by hybridizing one highly conserved region of the strand to a gold surface-bound “capture” oligo and another region to a gold nanoparticle-bound “target” oligo thus creating a SERS environment around the test oligo. This was accomplished in a three step aqueous hybridization procedure using preparations similar to those previously developed^{27, 52} with several variations. Test samples were composed of the four types of DNA duplexes visualized in Figure 4.1 and defined in Table 4.1 – those formed from complementary oligos, those formed from oligos with a single mid-sequence base mismatch (SNP), those formed from oligos that have three delocalized mismatches (DTM), and those that have a polymorphic region of three adjacent mismatches (ATM). Resulting Raman spectra were compared for statistically significant intensity and peak position differences at four characteristic peaks as described below. The overall method involves eight main steps discussed further in the Methods section.

4.2.1 Substrate Preparation 1. As described elsewhere,⁵² ~2-3 μm gold spots (400 nm Au on 30 nm Chrome) situated in arrays of 20 spots per array are prepared on quartz wafers (SiliconQuest) using photolithography and electron beam deposition. The wafer was treated with 30% w/w peroxide for 1 hr immediately prior to spotting.

4.2.2 Oligo Preparation 1 (Capture Strands). 40 mer oligonucleotides with a 3' thiol modification were used as the capture strands. The sequence (5'– ATC GCA TGA GCT CAT ATG CAT CGA TGA CTA T₁₀ – Thiol – 3') was chosen with ten thymine bases acting as a spacer^{27, 82} immediately adjacent to the thiol modification followed by 30 bases chosen to interact with the 30 bases on the 5' end of the test strands. Oligos were purified with a standard desalt during manufacturing.

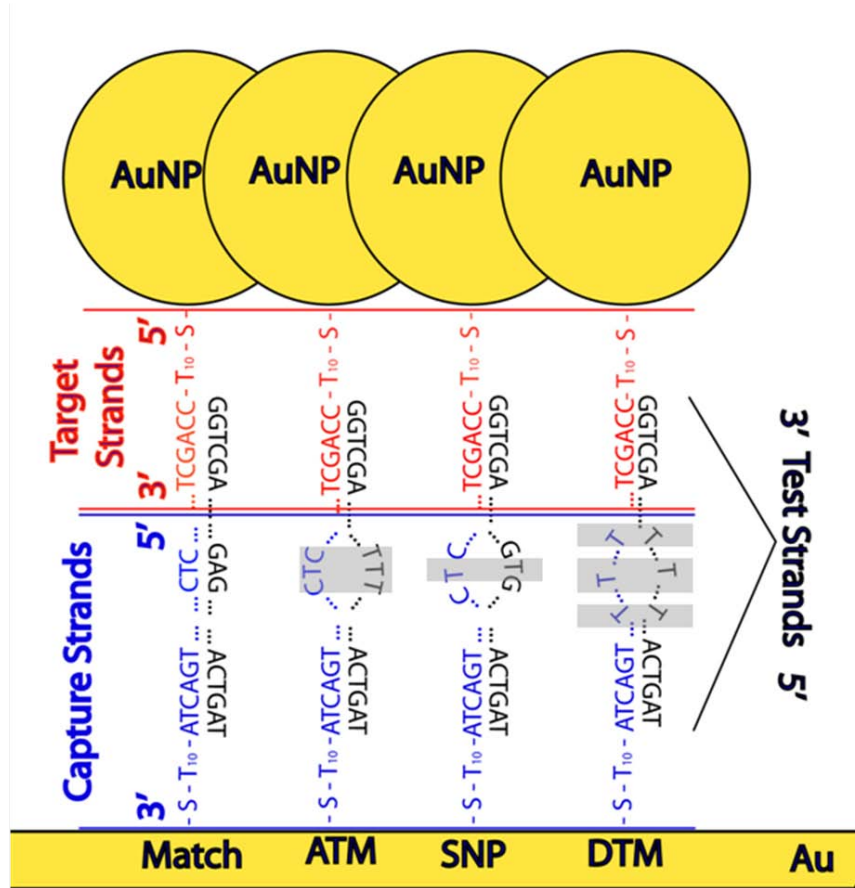


Figure 4.1. Visualization of the hybridization scheme used to create a SERS environment around DNA duplexes. Single stranded oligos are hybridized as either completely matched, with a single mismatch (SNP), with an adjacent triple mismatch (ATM), or with a delocalized triple mismatch (DTM). Grey boxes highlight the mismatches for clarity.

Table 4.1. Oligonucleotide Design for Matched and Mismatched Sequences

Sequence	
Target Strand	5' - Thiol - T ₁₀ - CCA GCT TAGA - 3'
Capture Strand	5' - ATC GCA TGA GCT CAT ATG CAT CGA TGA CTA - T ₁₀ - Thiol - 3'
Complementary	3' - GGT CGA ATC TTA GCG TAC TCG AGT ATA CGT AGC TAC TGAT - 5'
Single Mismatch	3' - GGT CGA ATC TTA GCG TAC TCG - T - GTA TAC GTA GCT ACT GAT - 5'
Adjacent Triple Mismatched	3' - GGT CGA ATC TTA GCG TAC TC - TTT - TAT ACG TAG CTA CTG AT - 5'
Delocalized Triple Mismatched	3' - GGT CGA ATC TT - T - GCG T - T - C TCG AGT - T - TAC GTA GCT ACT GAT - 5'

The DNA capture solution was prepared by suspending dry DNA (from IDT) in and aqueous buffer, IDTE (IDT), to a 1 μ M concentration. This solution was first reduced with

Reductacryl (Calbiochem) then spotted onto micropatterned metal arrays on the quartz wafer which was then placed in a humid environment and incubated for 6 hrs at room temperature.

4.2.3 Substrate Preparation 2. After incubation the wafer was rinsed by multiple submersions in DI water and dried under nitrogen. Then the wafer was spotted with a 1 mM solution of mercapto-1-hexanol (MHOH) (Sigma) in ethanol and allowed to sit overnight (~17 hrs) in order to limit nonspecific binding in later steps.^{27, 83} MHOH was rinsed with DI water by immersion and dried under nitrogen.

4.2.4 Oligo Preparation 2 (Target Strands). Target strands were designed to be complementary to the last ten bases on the 3' terminus of the test strands. Therefore, target strands contained 20 bases – ten meant to hybridize with the linking strands and ten thymine spacers – and a thiol modification on the 5' end. Procedure for functionalization with gold nanoparticles and hybridization with capture strands is similar to that developed by Sun et al. with some variations.²⁷

The Target solution was prepared by adding concentrated DNA in IDTE to a solution of 40 nm gold nanoparticles (Ted Pella) such that the final DNA concentration of the target solution was 10 μ M. After 24 hrs, the gold/oligo solution was buffered with a 10 mM pH 7.5 phosphate buffer/tween solution (PB/T). After 30 minutes the target solution was salted by four additions of 20 μ L 4 M NaCl with vigorous mixing in between additions to bring the

final salt concentration to 0.3 *M*. After ~48 hrs, the target solutions were washed in PB/T with 0.3 *M* NaCl twice with centrifugations (and redispersing vortexes) in between and again brought up to 10 μ *M* in the same solution.

4.2.5 Oligo Preparation 3 (Test Strands). Test strands were deemed complementary (matched), single mismatched (SNP), adjacent triple mismatched (ATM), delocalized triple mismatched (DTM), or non-complementary (completely mismatched) based on how they matched to the capture strand, as described in Table 4.1. All mismatches were designed to be thymine-thymine or thymine-cytosine mismatches to minimize the possibility of alternate Watson-Crick base pairings such as the “wobble”.

Test Strands were also prepared by diluting the dry DNA to 1 μ *M* solutions in IDTE. Immediately following Substrate Preparation 2, the test strands were spotted onto appropriate arrays, again put in a humid environment, and incubated at 40°C for 4 hrs. The wafer was then rinsed by immersion in DI water and dried slightly with nitrogen.

4.2.6 Hybridization. Finally, target strands were spotted onto the arrays, again put in a humid environment, and incubated at 40°C for 4 hrs. The wafer was then rinsed with 10 *mM* PB/T and immersion rinsed in DI water and dried with nitrogen. Finally, the wafer was soaked in Silver Enhance (Ted Pella) solution for 10 min, rinsed and dried again, and

immediately analyzed with Raman. Further water rinses after 24 hrs did not seem to have an effect on the Raman signal.

4.2.7 Raman Detection. Raman scattering was excited using a 12 mW red HeNe laser (Thorlabs) coupled to an inverted microscope (Nikon, Diaphot) with a 60x dry objective (Olympus). The reflected Raman signal was analyzed through an imaging spectrograph (PI Acton, SpectraPro SP-2156) and detected with a liquid nitrogen cooled CCD camera (PI Acton, Spec-10:100BR/LN). The laser power at the sample measured 3 mW and the laser spot was about 2 μm in diameter. Collection times were 20 s. GRAMS/AI 8.0 software (Thermo) was used to average the spectra and for baseline correction.

4.2.8 Statistical Analysis. A two-sided, two-sample t-test ($\alpha = 0.05$) assuming unequal variances was applied to the seven median intensity values of the selected peaks. The same method was employed to determine significance in peak shifts except that peak positions were used in lieu of intensities. Peak intensities were normalized prior to plotting (see Fig. 4.4) to more accurately represent the individual shifts.

4.3 Results

Twenty-four Raman spectra from each test sample were collected and processed as previously reported.⁵² To eliminate high and low outliers, subsets of seven median spectra were selected from each original group of 24. These median subsets were averaged to determine overall intensity for plotting and the intensities and peak positions of the four characteristic nucleic acid peaks were extracted for statistical analysis. Statistical significance was determined (from $p < 0.01$ to $p < 0.001$, $\alpha = 0.05$) for differences between each of the samples at the four selected peaks. These peaks include guanine ring breathing at 660 cm^{-1} ,^{71, 76} the phosphodiester backbone peak around 840 cm^{-1} ,⁷⁷ a guanine stretch at 970 cm^{-1} ,^{71, 76, 77} and guanine vibrations at 1174 cm^{-1} .⁷⁶ Figure 4.2 more succinctly shows the peak positions and standard error of these key peaks. Note that among all these peaks, the overall Raman intensity of the complementary sample is significantly greater than that of the single mismatched sample which is itself greater than the triple mismatched samples. Significance levels are individually summarized in Table 4.2.

Scanning electron microscopy (SEM) images seen in Figure 4.3 qualitatively support the theory that more nucleotides are being hybridized in complementary samples than in single-mismatched and multiple mismatched samples. The figure shows greater surface area coverage of nanoparticles on the gold spot with complementary oligos and a reduced amount on the spots with mismatched oligos. Additionally, image analysis software (ImageJ)

concludes the percent coverage of nanoparticles in the representative areas is 25.0% for the matched sample, 17.8% for the SNP sample, and 14.1% for the triple mismatched sample.

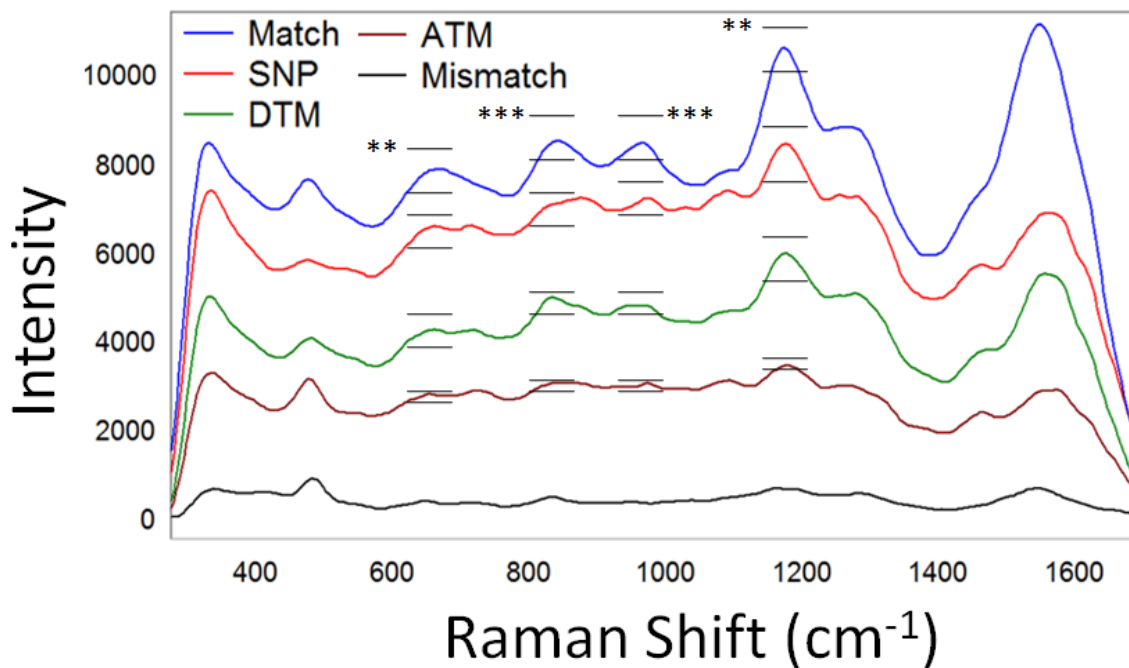


Figure 4.2. Raman spectra comparing the averaged median intensities of single-stranded oligos (matched, single-mismatched, delocalized triple mismatched, adjacent triple mismatch, and completely mismatched) hybridized to form double-stranded duplexes. Standard error bars are included for the key peaks. (see Table 4.2 for p-values)

Table 4.2. Two-tail p-values from t-test results used to test the significance of intensity differences among selected peaks. Asterisks represent corresponding significance level.

		Comparison		
		Match/SNP	SNP/DTM	DTM/ATM
Relative Peak Position (cm ⁻¹)	660	5.19x10 ⁻³ **	6.06x10 ⁻⁵ ***	5.98x10 ⁻⁴ ***
	840	1.11x10 ⁻³ ***	5.45x10 ⁻⁵ ***	3.51x10 ⁻⁸ ***
	970	8.76x10 ⁻⁴ ***	2.18x10 ⁻⁵ ***	1.85x10 ⁻⁷ ***
	1170	4.80x10 ⁻⁴ ***	4.82x10 ⁻³ **	6.73x10 ⁻⁴ ***

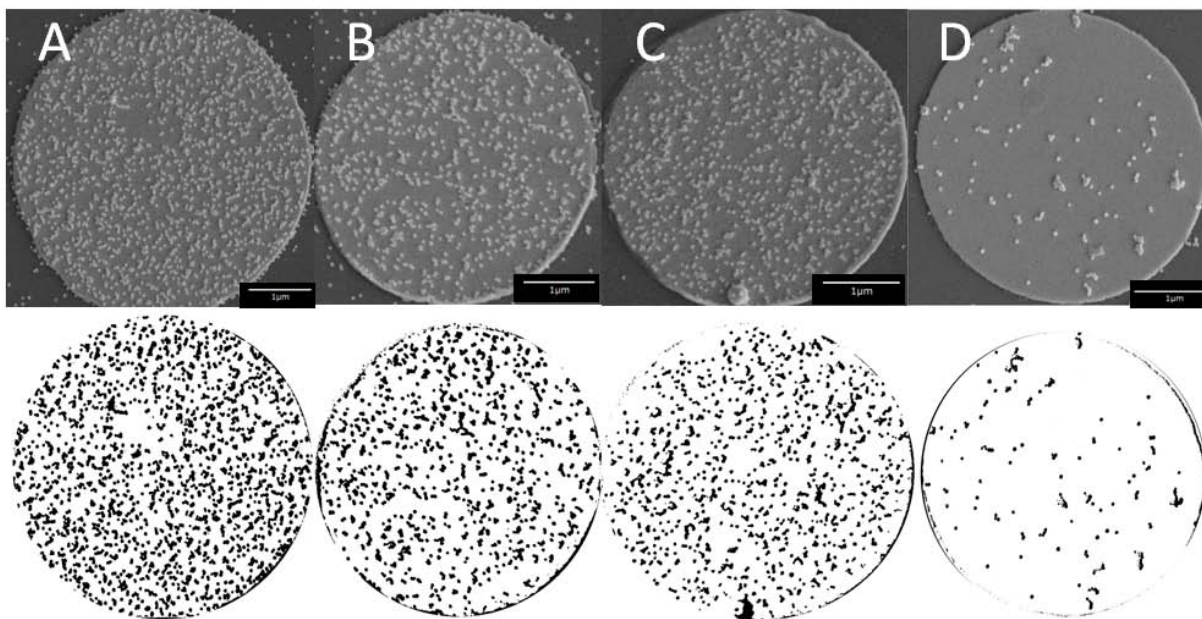


Figure 4.3. Scanning electron micrographs of representative sample capture surfaces after hybridizing single-stranded oligos and gold nanoparticles to form double-stranded SERS complexes (top row). The bottom row contains corresponding particle count analyses that clarify the different particle densities of each micrograph. These images enable a qualitative analysis of the nanoparticle densities that results from hybridizing with (A) completely matched, (B) SNP, (C) triple mismatched, and (D) completely mismatched test strands.

Figure 4.4 represents a magnification of the 500 – 1300 cm^{-1} area in Figure 4.2. The three aforementioned peaks, highlighted and magnified further in frames A-C, show statistically significant peak shifts when comparing the average matched sample to the SNP and ATM samples. The DTM sample followed in trend with the other mismatched samples and was therefore excluded for clarity. Constituent peak heights were normalized to the peak of interest before averaging. It should be noted that while the average position among mismatched samples appears different in Figure 4.4, this difference is not statistically significant and therefore will not be treated as meaningful. Only position shifts between the matched samples and the mismatched samples are statistically significant. Peak positions are shown with their respective standard errors and levels of significant difference as compared to the matched sample. Table 4.3 summarizes the significance level of each shift.

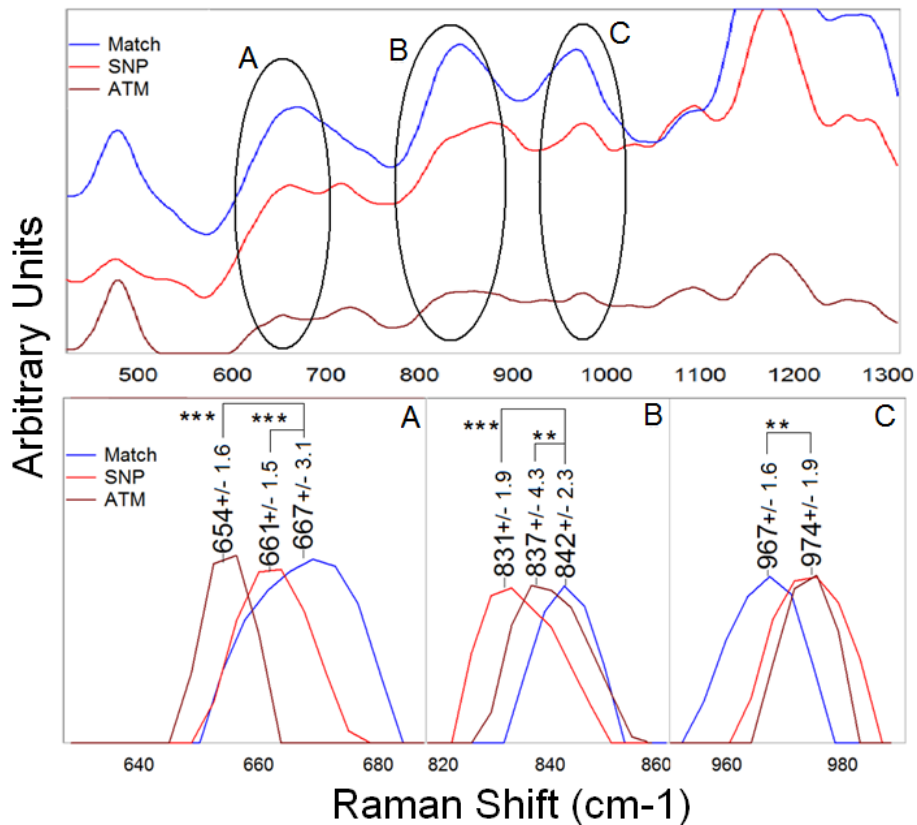


Figure 4.4. Raman spectra highlighting the peak position shifts that occur when comparing the average matched sample to the SNP and ATM samples. The DTM sample followed in trend with the other mismatched samples and was therefore excluded for clarity. The highlighted peaks represent (A) down-shifting guanine ring breathing and (B) phosphodiester stretch modes, and (C) an up-shifting guanine/sugar stretch. Peak positions are shown with their respective standard errors representing the variability between the seven median spectra averaged together to obtain these positions. Levels of significant difference are compared to the matched sample. Constituent peak intensities were baseline subtracted and normalized to the peak of interest before averaging then smoothed. (see Table 4.3 for p-values)

Table 4.3. Two-tail p-values from t-test results used to test the significance of peak position differences among selected peaks. Asterisks represent corresponding significance level.

Relative Peak Position (cm ⁻¹)	Comparison	
	Match/SNP	Match/ATM
660	$2.98 \times 10^{-2} *$	$6.68 \times 10^{-4} ***$
840	$2.05 \times 10^{-4} ***$	$2.36 \times 10^{-2} *$
970	$6.26 \times 10^{-3} **$	$1.12 \times 10^{-2} *$

4.4 Discussion

The effort of these experiments was to extend the use of Raman spectroscopy to detect genetic markers on unmodified oligonucleotides and to determine the applicability of using this type of approach for exploring DNA hybridization characteristics associated with SNPs and PRs. There are two mechanisms behind the feasibility of these experiments. One, because genetic markers such as SNPs and PRs contain energetically unfavorable nucleotide mismatches in the DNA helix, mismatched oligos are less likely to hybridize as effectively as matched oligos and are more successfully removed with stringent washes. Because the creation of a SERS environment is dependent on the hybridization of oligos, mismatched samples have a decreased overall Raman signal which can be used to differentiate them from matched samples. Increasing the number of mismatches only amplifies this effect and further decrease the Raman signal. Secondly, it is proposed that hybridized samples with mismatches are subject to altered intermolecular bonding patterns that affect characteristic vibration modes. Therefore, not only is the overall Raman intensity different for mismatched samples, the Raman signature also gives insight into the mismatch.

In accordance with the theoretical basis for this experiment and as shown in Figures 4.2 and 4.3, it is to be expected that the SNP samples have a weaker Raman intensity than matched oligos and that multiple mismatches exhibit a weaker signal still. Based on free energy calculations of single stranded oligo hybridizations as described and tabulated by

Turner et al,⁸⁸ it is predicted that among the multiple mismatched samples the DTM will show a higher binding affinity than the ATM. These calculations assume base-pair mismatches form energetically unfavorable internal loops within the helix and infer that when predicting hybridization stability both the size of the mismatch and the sequence position of the mismatch are important. In this case, not only would the DTM incur a lower cumulative energy penalty than the ATM but also the mismatches in the DTM are positioned such that they sacrifice fewer energetically favorable matches. Such calculations conclude that the energy difference between the two triple mismatched samples is only 1.4 kcal in favor of DTM hybridization. Though Raman experiments were able to distinguish this difference significantly, as seen in Figure 4.2, experimental conditions such as hybridization temperature, reagent concentration, DNA age, and quality of the photolithography must be tightly controlled for successful differentiation. It is proposed that such a small energy difference is very near the lower level of detection for this technique. However, between the match, SNP, and triple mismatches in general, experimental results show robust, consistent, and reproducible intensity trends. For comparison, free energy calculations comparing DTM and SNP show a 5.5 kcal difference and those comparing SNP and the complete match hybridization show a 4.8 kcal difference.

To further improve understanding of the system, observations were also made regarding peak positions in the Raman spectra seen in Figures 4.2 and 4.4. The principal

observation is a slight shift in the position of three of the characteristic peaks mentioned above – the guanine ring breathing peak at 660 cm^{-1} ,^{71, 76} the phosphodiester backbone peak around 840 cm^{-1} ,⁷⁷ and the guanine stretch at 970 cm^{-1} .^{71, 76, 77} Because Raman spectroscopy is a fingerprint technique, each peak represents a specific molecular vibration that contains information about its local chemical environment. Therefore additional information can be gained by observing shifts in peak position as they relate to molecular conformations, structural rearrangements, and other changes in the chemical environment.

Significant differences here can be used to gain insight into chemical changes that occur upon hybridization of mismatched oligos. Frame A of Figure 4.4 shows that the phosphodiester peak at 842 cm^{-1} in the matched sample is conspicuously shifted down (“blue-shifted”) to around 831 cm^{-1} for the mismatched samples. It has been observed in previous studies that the phosphodiester band blue-shifts from 835 cm^{-1} to 815 cm^{-1} to near 800 cm^{-1} as the order and rigidity of the system decreases from B-DNA to A-DNA to single stranded oligonucleotides, respectively.⁷⁷ In other words, as the order and rigidity of the bond decreases, it takes less energy from an incident photon to induce the same vibrational mode. Empirically this can be represented with the equation

$$1. \quad \Delta E_{\text{photon}} = \Delta E_{\text{transition}} = \frac{h}{2\pi} \sqrt{\frac{k}{\mu}} \quad 89$$

or

$$2. \quad \nu = \frac{1}{2\pi c} \sqrt{\frac{k}{\mu}} \quad 89$$

Where h is Planck's constant, c is the speed of light, k is Hooke's law force constant for stretching the bond, ν is the Raman frequency shift for the associated vibration, and μ is the reduced mass of the two atoms whose bond is being affected.⁸⁹

Interestingly, frame C of Figure 4.4 shows that the 967 cm^{-1} peak associated with the bond stretch between guanine and its sugar is seen to red-shift in the SNP and ATM samples as compared to the matched sample. We speculate that breaking the hydrogen bonding pattern in the bases induces a more widespread redistribution in electron arrangement over the entire nucleotide that relaxes structural bonds near the backbone and strengthens those nearer to the base. In this case, the 967 cm^{-1} peak shifts to approximately 974 cm^{-1} in the two mismatched samples. By contrast, a vibrational mode not necessarily associated with nucleotide structure, guanine's imidazole ring breathing mode related to the peak at 667 cm^{-1} , blue shifts to $\sim 654 \text{ cm}^{-1}$ in the mismatched samples again indicating a decreased sense of order within the ring. This final shift can be seen in Figure 4.4, frame A. Again, there were no meaningful position shifts amongst the mismatched samples, only between the mismatched samples and the matched sample.

Given these peak shifts, equations 1 and 2 above can further be used to explore the effect that mismatches in the DNA helix have on related Hooke's law force constants, k , thus resulting in a semi-quantitative representation of the rigidity of the system. For instance, assuming a negligible difference of reduced masses between any two samples, these equations predict that the difference in the phosphodiester stretch peak position corresponds to only a 2.9 % difference in force constants when comparing the matched and SNP samples, the samples with the largest peak shifts. Likewise, considering matched and ATM samples, peak shifts in the guanine/sugar stretch indicate a 1.4 % difference while the shift in ring breathing modes indicates a 4.2 % difference in force constants. Such calculations attest to the varied amount of information that can be obtained from these types of Raman studies, extending the technique both as a robust polymorphism detection scheme for genotyping analyses and as a useful tool for analyzing additional minute and fundamental chemical relationships regarding DNA hybridization.

4.5 Conclusions

In summary, this work reports a preliminary method capable of detecting and exploring genetic markers composed of mid-sequence SNPs and multiple base mismatches in unmodified DNA sequences. The SERS approach provides both a robust detection rubric for further analyses using polymorphisms and a useful research tool potentially capable of exploring precise biochemical changes associated with DNA mutations. A similar design could easily be transformed to create useful automated microarrays or microfluidic formats that further improve efficiency.

Chapter 5: In Situ Monitoring of Adipogenesis with Human Adipose Derived Stem Cells Using Surface Enhanced Raman Spectroscopy

Techniques capable of non-destructively collecting high quality, real-time chemical information from living human stem cells are of increasing importance given the escalating relevance of stem cells in therapeutic and regenerative medicines. Raman spectroscopy is one such technique that can non-destructively collect real-time chemical information. Living cells uptake gold nanoparticles and transport these particles through an endosomal pathway. Once inside the endosome, nanoparticles aggregate into clusters that give rise to large spectroscopic enhancements that can be used to elucidate local chemical environments through the use of surface enhanced Raman spectroscopy. This report uses 40 nm colloidal gold nanoparticles to create volumes of surface-enhanced Raman scattering (SERS) within living human adipose derived adult stem cells enabling molecular information to be monitored. We exploit this technique to spectroscopically observe chemical changes that occur during the adipogenic differentiation of human adipose derived stem cells over a period of 22 days, monitoring both the production of lipids and the complex interplay between lipids, proteins, and chemical messengers involved in adipogenesis. The results

show fluctuations in local intracellular concentrations of cAMP, GDP, and GTP during adipogenesis.

5.1 Introduction

The manipulation and measurement of single biological entities is critical for the development of accurate cell-based medical, pharmaceutical, and environmental studies. Cell-based research platforms can be used to directly evaluate ways in which tumor cells interact with chemotherapeutic agents, new cosmetics formulations affect human epidermal keratinocytes, or in which pesticides affect lung tissue. The ideal cellular analysis platform could provide real-time, continuous data from *in vitro* and eventually *in vivo* cell cultures. Raman spectroscopy and surface enhanced Raman spectroscopy (SERS) are non-destructive light-based techniques that bring this ideal closer to reality than ever before.

Recent studies show that living cells naturally uptake gold nanoparticles into the endosomal pathway through fluid phase endocytosis.^{90, 91} The endocytosed particles are sent to endosomes and lysosomes where they aggregate, creating concentrated areas of enhanced Raman activity within the cell.^{56, 92} Using this system in tandem with SERS, cells can be examined for chemical changes without harmful biological preparations thereby creating the potential for real-time, continuous analyses of living organisms and their native functions. Thus far relatively few papers have been written on the topic of SERS in cells beyond proof of concept experiments.^{1, 57, 93, 94} To the author's knowledge none have reported using SERS to explore human adipose derived adult stem cells (hASCs) or adipocytes. Isolating differentiated and non-differentiated adipogenic stem cell pools has been a viable possibility

since the mid-1970s.⁹⁵ For interest, a thorough review of both the isolation and the differentiation procedures was published by Gimble and Guilak in 2003.⁹⁶

Interest in adipocyte research has increased recently, spawned by renewed interest in the fat cell's probable role in obesity, diabetes, and other metabolic disorders as well as its role in energy regulation.^{97,98} The differentiation of stem cells to adipocytes provides a basic platform for studying adipocytes and adipogenesis. Adipogenic differentiation is used here as a model system to explore the utility of SERS as a non-invasive in situ analysis method. In this work hASCs are dosed with gold nanoparticles then differentiated down an adipogenic pathway while spectroscopic "snapshots" of the chemical processes are collected. This research provides a foundational study for understanding the roles that SERS chemical analyses can have in stem cell differentiation studies. In the future SERS is expected to enable new insights into cellular processes such as adipogenesis and stem cell differentiation.

5.2 Methods and Materials

5.2.1 Cell Culture. In this work hASCs isolated from human adipose tissue (UNC-Chapel Hill IRB 04-1622) from a 36 year-old female were grown on glass slides in traditional growth medium and incubated at 37°C and 5% CO₂. The slides were modified with polydimethylsiloxane (PDMS) boundaries that continuously maintained the hASCs in media during incubation and while the samples were being examined outside the incubator. The growth medium consisted of minimum essential medium eagle, alpha-modified (α -MEM) supplemented with 10% fetal bovine serum (FBS), 100 units/mL penicillin, 100 μ g/mL streptomycin, and 2 mM L-glutamine. Human ASCs were seeded at a density of 7000 cells per slide in 1.5 mL of growth medium. Twenty-four hours after seeding, the cells were exposed to an aqueous colloidal suspension of 40 nm Au nanoparticles (TedPella).

After 20 days in culture, the growth medium was permanently replaced with an adipogenic medium consisting of α -MEM with 10% FBS, 100 units/mL Penicillin, 100 μ g/mL Streptomycin, 2 mM L-glutamine, 1 μ M Dexamethasone, 10 μ g/mL h-Insulin, 100 μ M Indomethacin, and 500 μ M Isobutylmethylxanthine (IBMX).

5.2.2 Raman Detection. Twenty-four hours after the addition of gold nanoparticles (and at subsequent time points) the cells were removed from the incubator and analyzed with a custom-made Raman microscope. Raman scattering was excited using a 12 mW red HeNe

laser (Thorlabs) coupled to an inverted microscope (Nikon, Diaphot) with a 100x dry objective (Nikon). The reflected Raman signal was analyzed through an imaging spectrograph (PI Acton, SpectraPro SP-2156) and detected with a liquid nitrogen cooled CCD camera (PI Acton, Spec-10:100BR/LN). Individual collection times of 20 s were used to highlight more general spectral changes and to reduce variability caused by transient molecular interactions with individual nanoparticles.¹ The laser power at the sample measured 3 mW and the laser spot was about 2 μm in diameter. According to previous research and results from our own lab and others,⁴⁹ this power and spot size are sufficient to induce a significant Raman effect yet harmless enough to avoid damaging the cell or interfering with the cell's natural functions.⁴⁹

Because hASCs are on average 10-20 μm in diameter, the 2 μm spot used in our Raman system enables the collection of spectra from sub-cellular areas allowing us to differentiate the nucleus from other components like transport vesicles. Our research shows that undifferentiated cells exhibit several spots of notable Raman signal, often including the nucleus and the surrounding nuclear envelope. However, consistently intense Raman signals come from smaller organelles, most likely endosomes due to the nanoparticle aggregation that occurs in these areas. Raman spectra were collected from these areas and nanoparticle aggregation was verified using Transmission electron microscopy (TEM).

Literature suggests that a 5 mW 488 nm laser can kill a cell with a 5 minute continuous exposure. A lower energy 785 nm laser induced very little cell mortality at 115 mW with a 40 minute exposure.⁴⁹ Our 633 nm HeNe laser uses photons whose energy lie somewhere between those of the 488 and 785 nm lasers and power at the sample has been measured at only ~ 3 mW. Additionally, our own previous Raman studies show that laser exposure times of 30 seconds or less are more than adequate at detecting Raman signal from SERS enhanced hADAS cells, especially from highly Raman active areas like the nucleus. Thus it is unlikely that any complications will arise due to the Raman analysis directly.

5.2.3 Data Processing. GRAMS/AI 8.0 software (Thermo) was used for spectrometric analysis and correction. Data were smoothed and baseline corrected by subtracting an offset. The offset was a straight line from the local minimum (created by the laser line notch filter) in the spectrum at ~200 relative wavenumbers to the local minimum at ~1800 relative wavenumbers (past the primary region of observed Raman peaks). The “rubber band” method was not used for baseline correction as its human input makes it more susceptible to the artificial generation of data. The spectra were then normalized to the ubiquitous 1328 cm⁻¹ protein peak¹⁻³ and offset for comparison.

5.3 Results

Research has shown that gold nanoparticles are endocytosed into cells via the endosomal pathway within about 20 minutes of addition to cell media.^{1, 56, 99} The nanoparticles are generally packaged and sent to endosomes within the cell and remain sequestered there. After approximately 120 minutes highly efficient nanoparticle dimers and trimers give rise to large SERS enhancements; after which additional aggregation may trigger a specific treatment within the endosome that limits interparticle distances and thus tempers the SERS enhancement.⁹⁹ Nevertheless, the SERS effect enables local chemical environments to be easily discerned, especially concerning the endosomal subenvironments. TEM was used to confirm the endocytosis and aggregation of gold nanoparticles into the cells. Figure 5.1 shows TEM micrographs of representative hASCs after incubation with gold particles for approximately 24 hrs. These images confirm both the uptake and aggregation of nanoparticles within the cells. These results are in agreement with past research utilizing a variety of cell lines.^{91, 92, 99}

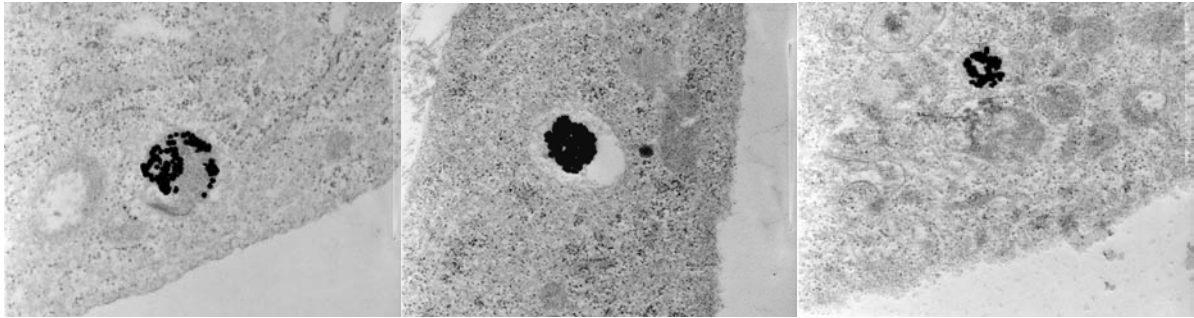


Figure 5.1. Transmission electron micrographs of colloidal gold nanoparticles aggregated within differentiating hASCs. Nanoparticles are 40 nm in diameter.

Raman spectroscopy was used to evaluate the local chemical environments of hASCs over time. Typical Raman spectra of undifferentiated hASCs are shown in Figure 5.2 at 2, 6, 8, and 44 days after seeding, spectra are offset for clarity. Major peaks include those representing C-C vibrations in proteins and nucleic acids (644 cm^{-1}),^{1, 2, 76, 100} sugar-phosphate stretches from DNA backbone (847 cm^{-1}),^{2, 77, 92, 100} a generic CH_3 rocking (1147 cm^{-1}),³ and a dominant protein-related CH_2/CH_3 deformation (1324 cm^{-1}).¹⁻³ While other Raman signatures can be found within the undifferentiated stem cells, the particular signatures shown in Figure 5.2 are by far the most common and have the strongest intensities. This series of experiments verifies the existence of a dominant Raman spectrum for undifferentiated hASCs with little variation throughout time in culture.

A second set of experiments were performed to evaluate chemical changes in the stem cells during differentiation down an adipogenic pathway. One day after substituting the growth medium with adipogenic medium, the spectra become more diverse as can be seen in

Figure 5.3a. Despite the diversity, however, the signals do share common changes in characteristic peaks as compared to the undifferentiated stem cells. Most notable are the appearance of lipid related peaks at 775 cm^{-1} ,¹ and 1362 cm^{-1} ,^{1,2} soon followed by a relative increase in nucleoside-related peaks at 1194 cm^{-1} ,^{1,76} and 1225 cm^{-1} ,^{1,71,76} and another lipid peak at 1080 cm^{-1} ,^{2,3,45,101} as shown in Figure 3b. As compared to undifferentiated spectra, there is also a reduction in the 514 cm^{-1} and 1147 cm^{-1} peaks relative to the 1320 cm^{-1} protein peak. The 514 cm^{-1} peak is often attributed to disulfide bridges between cysteine residues¹⁰² while the 1147 cm^{-1} peak is related to a methyl rocking. Raman assignments are summarized in Table 5.1.

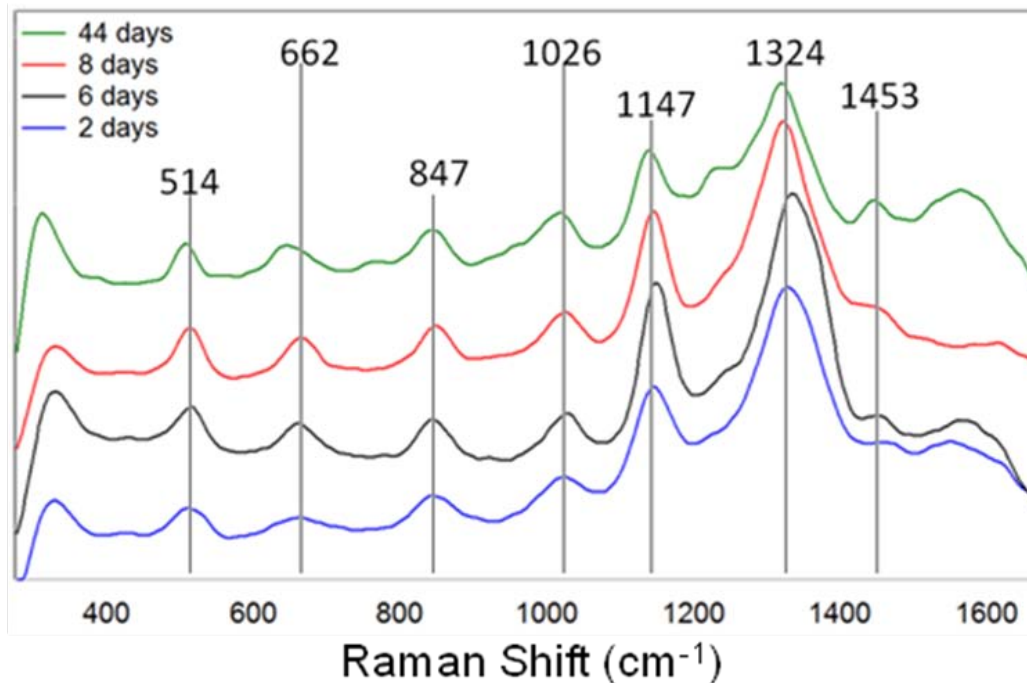


Figure 5.2. Representative surface-enhanced Raman spectra of undifferentiated hASCs measured 2 (blue), 6 (black), 8 (red), and 44 (green) days after seeding. Spectra are smoothed and normalized to the ubiquitous 1328 cm^{-1} protein peak¹⁻³ and offset for comparison.

By comparing the spectra in Figure 5.2 to those in Figure 5.3a-d, it can be deduced that the transition from stem cell to adipocyte also causes several notable peak shifts. Namely, the 1026 cm^{-1} peak linked to C-O and C-N bonds in nucleic acids^{71, 76} and amino acid residues^{3, 100} in undifferentiated stem cells red-shifts to 1037 cm^{-1} in differentiating cells, where it remains throughout and after differentiation. By contrast, the 662 cm^{-1} peak also related to assorted nucleic and amino acid vibrations^{1, 2, 76, 100} blue-shifts to near 618 cm^{-1} during the period of differentiation.

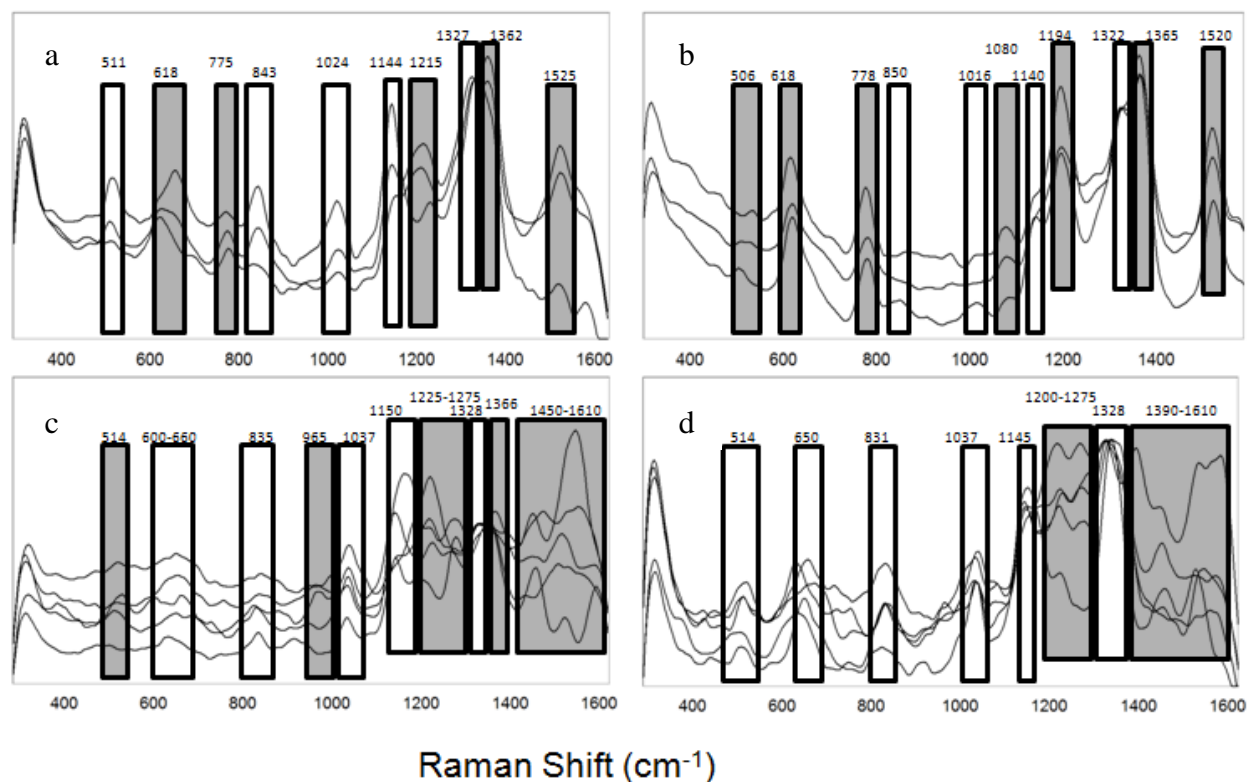


Figure 5.3. Representative surface-enhanced Raman spectra measured from hASCs at various time points during adipogenic differentiation. Samples were analyzed shortly after the addition of differentiation medium at (a) 1 and (b) 2 days then at intermediate time points between (c) 6 and 20 days and then finally at (d) 22 days. The variety of peak positions indicates the complex chemical changes that occur during differentiation. Spectra are smoothed and normalized to the ubiquitous 1328 cm^{-1} protein peak¹⁻³ and offset for comparison. Grey boxes highlight areas of spectral differences as compared to the undifferentiated cell spectra. Clear boxes highlight areas of similarity.

Table 5.1. Raman shift assignments and interpretations of Raman shifts observed in human adipose derived adult stem cells before, during, and after adipogenic differentiation.

Position (cm ⁻¹)	Lipid	Protein	Nucleotide
514		Cysteine disulfide bond	
618-662		C-C twist in Tyr, Phe	C-N bend in guanine
775-8	Lipid		
835-850		C-C stretch in proline; ring breathing in Tyr	Asymmetric phosphate stretch in DNA backbone
964		Phosphate stretch in hydroxyapatite	
1026-1037		C-N stretch in Phe; C-H bend in Phe	C-N stretch in guanine
1080	C-O, C-C, & phosphate stretching		
1145		CH ₃ rocking	
1194			C-H bend in cytosine; C-N stretch in adenine
1225-1275		CH ₂ & CH ₃ bending; Amide III vibration	C-C stretch in cytosine
1328-1335		CH ₂ & CH ₃ deformation; C-H bend in Phe, Trp	
1365	CH ₂ deformation		
1394			C-N stretch in adenine
1453-1595	Miscellaneous lipid vibrations	Miscellaneous protein vibrations	Adenine, cytosine, guanine

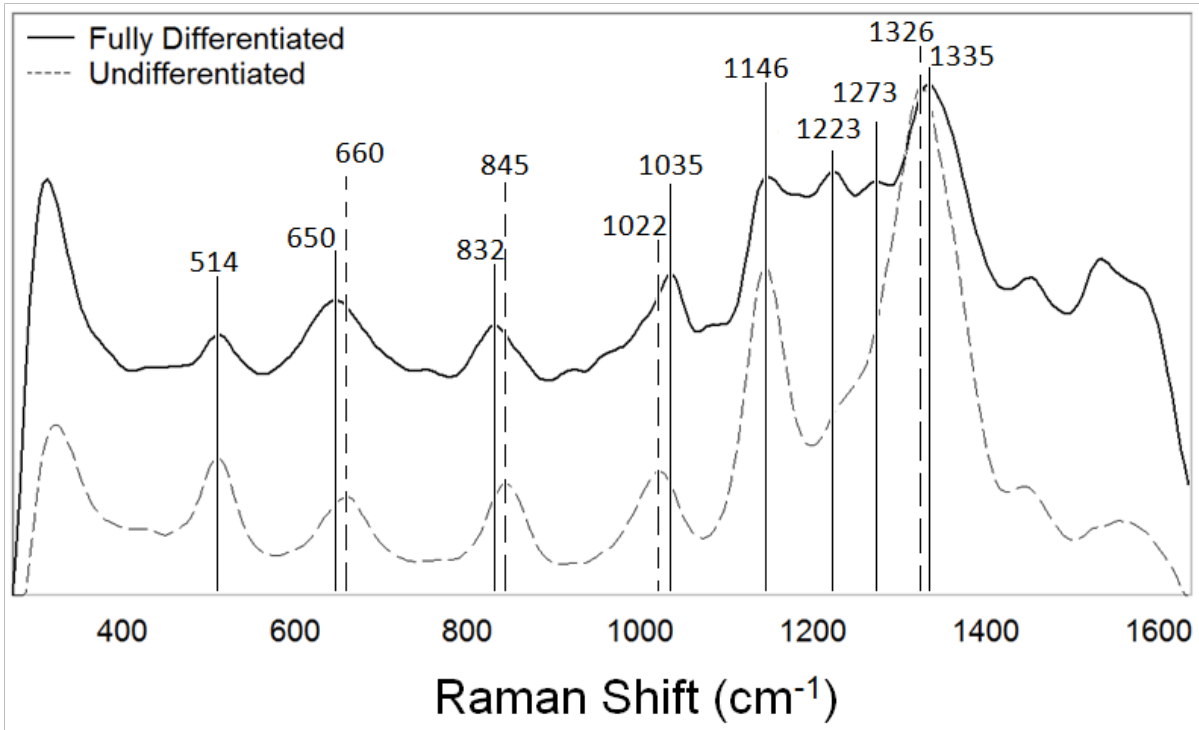


Figure 5.4. Raman spectra showing an average of the five fully differentiated adipocyte spectra from Figure 3d compared to an average of the four undifferentiated stem cell spectra in Figure 2. The figure highlights the spectral similarities and differences that are common between undifferentiated and differentiated stem cells.

Much of the cell-to-cell variations in peak positions diminished after 22 days of differentiation, as seen in Figure 5.3d. At this point the shape and size of the cells indicates that the cells have fully differentiated into adipocytes. A majority of the detectable Raman activity from these adipocytes again highlights peaks common to the undifferentiated cell

spectra with a major peak around 1328 cm^{-1} and lingering contributions from the 1360's cm^{-1} lipid peak that first appeared during differentiation. The 1147 cm^{-1} methyl peak present in undifferentiated hASCs also reappears in adipocytes as does a slightly broadened 514 cm^{-1} . The 847 cm^{-1} phosphate peak returns to a shifted 830 cm^{-1} and the protein peaks in the $1020\text{-}1037\text{ cm}^{-1}$ and $600\text{-}650\text{ cm}^{-1}$ ranges stabilize and return to around the 1037 cm^{-1} and 650 cm^{-1} positions, respectively. However, activity in the $1490\text{-}1610\text{ cm}^{-1}$ and the $1220\text{-}1275\text{ cm}^{-1}$ ranges retains an increased prominence from earlier stages of differentiation. To highlight these contrasts Figure 5.4 shows an average of the five spectra of fully differentiated adipocytes from Figure 5.3d compared to an average of the four spectra of the undifferentiated stem cells in Figure 5.2.

5.4 Discussion

The purpose of this study was to use gold nanoparticles to create a SERS environment within hASCs and to use this enhanced spectroscopic capability to monitor the chemical activity that occurs during adipogenic differentiation. From earlier TEM studies and the images shown in Figure 5.1 it is clear the nanoparticles are being localized in specific compartments within the cells, predominantly within the endosomes.^{1, 99} Because the endosomal pathway is central to the sorting and transport of proteins, lipids, and various chemical messengers into and out of the cell,¹⁰³ such a pathway provides a convenient vantage point from which fluxes in cellular chemistry can be observed. In these experiments we collect Raman spectra from these enhanced areas over a period of time in which the stem cells are differentiated down an adipogenic pathway. We propose that endosomes are likely exposed to the increase in lipid and fatty acid production that occurs during adipogenesis and that this change in chemical composition can be spectroscopically observed using the Raman enhancement provided by the gold nanoparticles trapped within the endosome.

Initially, the ubiquitous presence of nucleoside related molecules, particularly those derived from the purine nucleosides (such as ATP, GDP, cAMP, etc.), dominate the Raman signal collected from undifferentiated stem cells and can be observed in the Figure 5.2 spectra from the peaks at 662, 847, and 1026 cm^{-1} .^{76, 99} However, upon initiation of adipogenic differentiation the variation in Raman signatures from cell to cell becomes much

larger. The most notable initial changes are the gradual increase in lipid presence as is apparent in Figure 5.3a-b. One such change is a splitting in the 1320's cm^{-1} peak. Spectra taken from differentiating cells 24 hrs after addition of the differentiating medium show that this peak begins to show contributions from vibrations at 1362 cm^{-1} that are associated with CH_2 deformations in lipids. Representative spectra in Figures 5.3b-c show that this doublet begins to shift dominance to the 1360's cm^{-1} position within a day of its appearance and begins to overshadow the 1320's cm^{-1} peak within a week, signaling an increase in the overall lipid concentration with respect to the protein concentration as compared to similar ratios in the undifferentiated stem cells.

Another peak that correlates to this increased lipid presence is the peak at 775-778 cm^{-1} . Virtually nonexistent in any undifferentiated stem cell spectrum, this lipid peak in differentiating cells, when viewed in relation to its neighboring 843 cm^{-1} phosphate peak, grows in intensity in a direct correspondence to the degree and intensity of the appearance of the 1360's cm^{-1} peak. Likewise, the 1080 cm^{-1} peak thought to represent a combination of C-C and C-O vibrations in phospholipids^{2,45} appears and intensifies along with the 1320's cm^{-1} transition to 1362 cm^{-1} .

After the second day in differentiation medium there is a further increase in the 1194 cm^{-1} peak representing a large increase in adenine related molecules.⁷⁶ An increase in characteristic adenosine peaks in addition to those found in undifferentiated stem cells is

expected to be indicative of the role of cyclic AMP (cAMP) as a major component in adipogenic stimulation.¹⁰⁴⁻¹⁰⁶ Though cAMP is a general and widespread intracellular chemical messenger, studies show that mesenchymal stem cells exposed to elevated levels of cAMP are stimulated towards adipogenesis and away from osteogenesis.¹⁰⁴ Additionally, endosomes have cAMP regulated, ATP-dependent proton pumps whose increased activity could also result in larger adenosine signatures.⁹⁹

Accompanying the lipid and adenosine peaks, differentiating cells exhibit a shallow but broad hump that appears around 1225 cm^{-1} and is thought to represent two different vibrational modes in guanine.^{1, 76} This peak continues to increase in differentiation medium until the sixth day of differentiation when large contributions of guanine can be detected. These results support previous findings that guanine, specifically GDP and GTP have a role in regulating adenylate cyclase and therefore also regulating cAMP concentrations¹⁰⁷ and adipogenesis in general.

It is more difficult to identify the underlying mechanisms behind the 1024 and 662 cm^{-1} peak shifts in the differentiating cells. As both of these peak positions are characteristic of similar chemical constituents – amino acid and nucleic acid C-N and C-O bonds – it is easily conceivable that both would be present over broad peak ranges, both are representative of multiple vibrational bands, and that both would undergo substantial position shifts during differentiation. It is however interesting that the two peaks shift in concert with one another

perhaps indicating a covariant relationship underlying their activity. Unfortunately because of the generic nature of both peaks it is difficult to draw any definitive conclusions as to underlying mechanisms of this relationship at this time.

Similar curiosities are the reductions in the 514 and 1147 cm^{-1} peaks that occur during adipogenesis. It is not immediately clear why either the 514 cm^{-1} peak often attributed to cysteine-cysteine disulfide bridges or the 1147 cm^{-1} peak related to a methyl bend should so quickly diminish at the onset of differentiation when other cysteine and alkane related peaks increase. Perhaps the former is related to the “cysteine knot” at the core of bone morphogenic proteins whose natural activity in mesenchymal stem cells is to inhibit adipogenesis and stimulate osteogenesis.¹⁰⁸ Though a diminishing 514 cm^{-1} peak could indicate an absence or reduction of this inhibitory protein, the often ambiguous role of BMP in differentiation coupled with the milieu of alternate cysteine scenarios makes this a specious theory at best. It is clear that further studies must be explored to fully define these features.

Between the sixth and 20th days of differentiation the variety in cell morphology and in Raman spectra becomes more pronounced as the appearance of lipid droplets increases and individual Raman profiles become more erratic, reflecting the complex chemical changes the cells are undergoing. There is also a distinct increase in vibrational activity within the 1450-1610 cm^{-1} spectral region that indicates an increase in the presence and transport of

proteins, ubiquitous amino acids like tyrosine, and nucleic acids such as guanine, cytosine, and adenine. This trend is shown by the spectra in Figure 5.3c.

After 22 days of differentiation most of the cells have taken on the multi-locular appearance of adipocytes cultured *in vitro*.⁹⁷ Additionally, there are again characteristic spectra features from cell to cell that we speculate signal the conclusion of the cell's transformation. As shown in Figure 5.3d and Figure 5.4, note that the characteristic peaks in the adipocyte spectra are similar but not identical to peaks found in the undifferentiated stem cell signatures from Figure 5.2. Many of the adipocyte peak positions are slightly shifted and the peak ratios do not favor the 1320's cm^{-1} protein peak as heavily as in the original undifferentiated stem cells. The typical adipocyte spectrum retains the major protein peak of the hASCs spectra and shows lingering contributions from the 1360's cm^{-1} lipid peak. The 1147 cm^{-1} peak is again present as is a blue-shifted phosphate peak. Protein peaks in the 1020-1040 cm^{-1} and 600-650 cm^{-1} ranges stabilize and return to the 1030 and 650 cm^{-1} positions and a slightly broadened 510 cm^{-1} also returns. However, in the adipocyte spectra the 1390-1610 cm^{-1} and the 1200-1275 cm^{-1} ranges remain increased in prominence from the middle stages of differentiation. We hypothesize that the similarities between the stem cell spectra and the adipocyte spectra are indicative of a return to the synonymous mechanisms of homeostasis shared by the two cell types while the peak shifts and ratio differences highlight the reconfigured chemical makeup that distinguishes the two cell types.

At the conclusion of analysis, cells remained viable despite the presence of gold nanoparticles and the frequent perturbations in environmental conditions caused by removing the cultures from the incubator during analysis. The SERS signals were slightly diminished in intensity and number as compared to the undifferentiated analyses and were more difficult to locate because of the changes in cell morphology that often disguised the appearance of traditional organelles. The increase in cell volume that occurs during differentiation could also be responsible for reducing the signal as could the miscellaneous loss of gold particles that may have occurred during the transformation. Nonetheless, SERS signals remained relatively easy to find on the 22nd day of differentiation, 41 days after dosing with nanoparticles, with an average intensity registering approximately half of the intensity obtained from samples on the second day of differentiation.

5.5 Conclusions

In summary, we have analyzed SERS spectra from within the endosomes of living human adipose derived adult stem cells during a period of time in which the cells were differentiated along an adipogenic pathway. In so doing we have shown that SERS can be used to effectively monitor the relative activity of several intracellular chemical messengers, processes such as lipid production, and various transport phenomena. The existing though still incomplete body of research examining adipocytes and adipogenesis attests to the multitude of chemical changes that occur during differentiation in addition to the complex chemistry continuously occurring in support of cellular viability. In this report adipogenic differentiation is used as a model system to explore the utility of SERS as a non-invasive in situ analysis method. Such ability enables a closer understanding of the cell life cycle, differentiation, and cell signaling as well as drug delivery mechanisms and stress reactions that will become increasingly important for developing the advanced therapeutic and regenerative stem cell techniques of the future.

Chapter 6: Future Directions

6.1 Investigation of the SERS Effect

The infrastructure needed for such projects listed above will also allow us to further study the fundamental nature of the SERS effect. By attaching gold structures to each side of a DNA duplex we are effectively using the DNA as a spacer between the two metals. Oligo-based separations can be used in either nanoparticle or nanogap settings or a combination of the two as previously described. Compared to typical electron beam (e-beam) lithography methods, using DNA to fine-tune feature parameters allows for a huge decrease in cost per experiment and in the amount of overall infrastructure involved.

It is our opinion that using adsorbed functionalized nanoparticles to create nanogaps offers a readily accessible model system to study Raman enhancement and activity at the nanometer scale. For example, in Chapters 2 and 3 the Au surface-Au nanoparticle systems were implemented due to the ease of use, but many material combinations can be utilized to determine how material properties affect the generation of the Raman signal. In preliminary studies, Raman signal was generated primarily by the adsorbed oligonucleotides. Several researchers have utilized similar approaches to study DNA-based analysis, but they typically use a Raman tag, a molecule that has high Raman activity.^{27,28} This Raman tag approach can be used to probe more specific effects in the system. For example, if the flat surface is

functionalized with a Raman tag and the particle is not. Then experiments can be performed exploring the differences between the signals arising from a flat surface and a point separated by a few nanometers and those that arise from two flat surfaces separated by a few nanometers. Similarly, the effects of variations to the flat surface on the fields surrounding the nanoparticles can be probed by only tagging the nanoparticles. Both scenarios will further our fundamental knowledge of the SERS phenomenon and provide better understanding of the system as a whole.

The other obvious variable to be explored is the length between the two excited metal surfaces that create the SERS effect. By varying the length and design of the oligo strands composing the duplex we can vary the distance between metal features. Control over the separation between the nanoparticles and surface is easily controlled using standard biochemistry techniques and nucleic acid manipulation. Depending on temperature, concentration, stringency conditions, and additional monolayer competition, single stranded DNA oligos are predicted to have lengths of around 4.3 Å per base¹⁰⁹ and double stranded DNA of about 3.4 Å per base pair.⁸⁹ Therefore, adjusting the gap distance is mainly a matter of adjusting the oligo length and can be utilized to explore the effect that feature proximity has on surface enhanced Raman scattering.

6.2 Single-Cell SERS Analyses

Now that it has been shown that a SERS analysis is capable of monitoring stem cell differentiation, the logical next step is to develop this methodology to analyze increasingly smaller populations of cells that are experiencing some type of chemical/physiological change. Ultimately the goal is to monitor the chemistry of single living cells and of small subpopulation of cells as they react to a wide array of chemical stimuli. Non-invasive measurements of this nature enable data to be collected under conditions that more closely match those found *in vivo* and therefore represent a step forward for cellular analyses. In general, such an experiment requires five parts: 1) isolate a pool of cells, 2) create a transparent portable device capable of hosting living cells for extended periods of time, 3) select an intrinsic cellular chemical component that is both distinctly Raman active and can be used as a marker to follow through the process of interest, 4) collect Raman data, and 5) decide on the appropriate data analysis rubric. Experimentally, any of these five steps could be problematic however, both experimental and system designs can be implemented to limit the amount of error.

1. The main focus of this research will dictate what cell types are to be used. Stem cells could be used for further adipogenic studies, keratinocytes could be used for dermal toxicity work, tumor cells could be used to study chemotherapeutic efficacy, etc.

2. The portable cell habitat needs to be precisely designed so as to both support culturing of the cell pools but also to allow for repeat Raman analysis with minimal optical interference. It would be ideal for the device to have individual compartments that could subdivide the pools into smaller sample sizes and potentially even allow for repeat observations of individual cells or at least repeat observations of small cell populations. In this manner, population characteristics could be better identified, collected, and analyzed.

Taking cues from the microfluidic device research recently done by Walker and O'neill^{4, 110} our research group has designed a microfluidic device that is both compatible with our Raman system and will create a nurturing environment for cells. Essentially, two photolithography steps will be used to create a polydimethylsiloxane (PDMS) based microfluidic device on a 3" diameter, 0.35 mm thick quartz wafer. This device will ensure the cells are maintained in a comfortable environment during Raman analysis and can be used to control media flowrates and concentrations. As seen schematically below in Figure 6.2.1, the device will have four separate channels, each maintaining four separate subpopulations of cells. Each channel will be independently supplied by cell media allowing for multiple experiments to be run simultaneously. Namely, chemical stimulation can be staggered such that cells in channel 1 (blue) are treated as a control and are continuously fed standard culture medium while the remaining channels will be supplied with chemical stimuli at subsequent doses and time points.

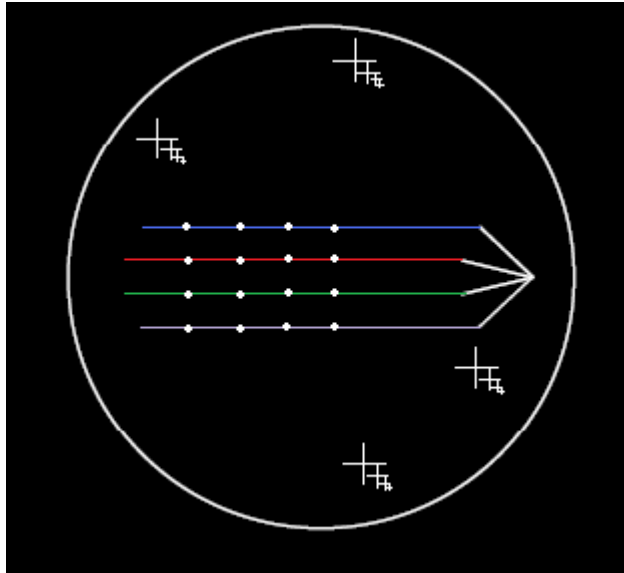


Figure 6.2.1. Schematic of the microfluidic device to be used in generic cell study. Media flow will be from left to right via a syringe pump piped to the point where the lines intersection. White circles represent “cell spots” where collagen patches will be used to capture cells as described by O’Neill et. al.⁴

With this design the device will simultaneously produce a set of cell populations that represent a spectrum of physiological states. Each cell spot will be 300 x 300 μm and should house about 80-100 cells according to past research.⁴ The wafer substrate provides a reasonably durable substrate that is thin enough to be analyzed in our inverted microscope/Raman device (Nikon Diaphot, ELWD 100x) and is transparent when filled with solution. It is also expected that the ability of microfluidic environments to rapidly change the soluble microenvironment will improve upon the temporal information that can be gained.

3. Another potential pitfall is selection of an appropriate marker which can be used to study cell response. Because Raman spectroscopy is best at characterizing chemical constituents by their functional groups (OH, C=O, NH₃, etc.) the question becomes where in the cell will the largest chemical change come from and what will that change be. Will chemical changes be most obvious in the lipid content of the cell membrane or perhaps the cytoplasmic protein content? Will there be a production of cytokines/chemokines. If so, will these compounds be best detected intra- or extracellularly.

By far, choosing an efficient biomarker will be the most challenging aspect of the experiment. The intracellular environment is complex and chemically robust and it is possible the resulting Raman spectrum will be overwhelmed by a myriad of information that makes it difficult to study differences in molecular content between the two cell types. Determining where the marker naturally occurs will enable us to target it most effectively. However, conjugating the surrounding environment with Raman enhancing gold nanoparticles (as previously discussed) and using any of a number of Raman labels to specifically highlight the constituent in question will also be explored. This last option while altering the intrinsic Raman signatures compensates by offering a host of possible labels and by enhancing detection sensitivity.

4. Fortunately, data in our own lab has shown that a well defined DNA signature can be observed in the nucleus of adipose derived stem cells, especially when used in conjunction

with gold nanoparticle enhancement. DNA and RNA profiles have been used successfully in past Raman experiments as markers in the differentiation of murine embryonic stem cells⁵⁰,⁵⁵ and our own studies have shown how the differentiation of hASCs can be monitored with the nanoparticle scheme. It is predicted that additional biomarkers will be discovered correlating to the individual pathway.

Besides concentrating on particular biomarkers, adverse effects from the noisy chemical environment can also be limited through the use of gold nanoparticles. Small metallic features such as gold nanoparticles are commonly used in surface-enhanced Raman spectroscopy (SERS) to dramatically increase and refine the Raman signal. Accordingly, studies by Kneipp et. al. show that introducing gold nanoparticles into cells through fluid phase uptake drastically improves the Raman signals that can be collected from Raman active components of living cells.^{93, 94} Figure 6.2.2 represents corroborating preliminary research done in our own lab that uses 40 nm gold nanoparticles to enhance the Raman signature present in different parts of a hASCs. However, as shown in Chapter 5, hASCs generally exhibit a main type of SERS spectrum at normal states homeostasis and presumably other cell types will also show similar characteristic spectra.

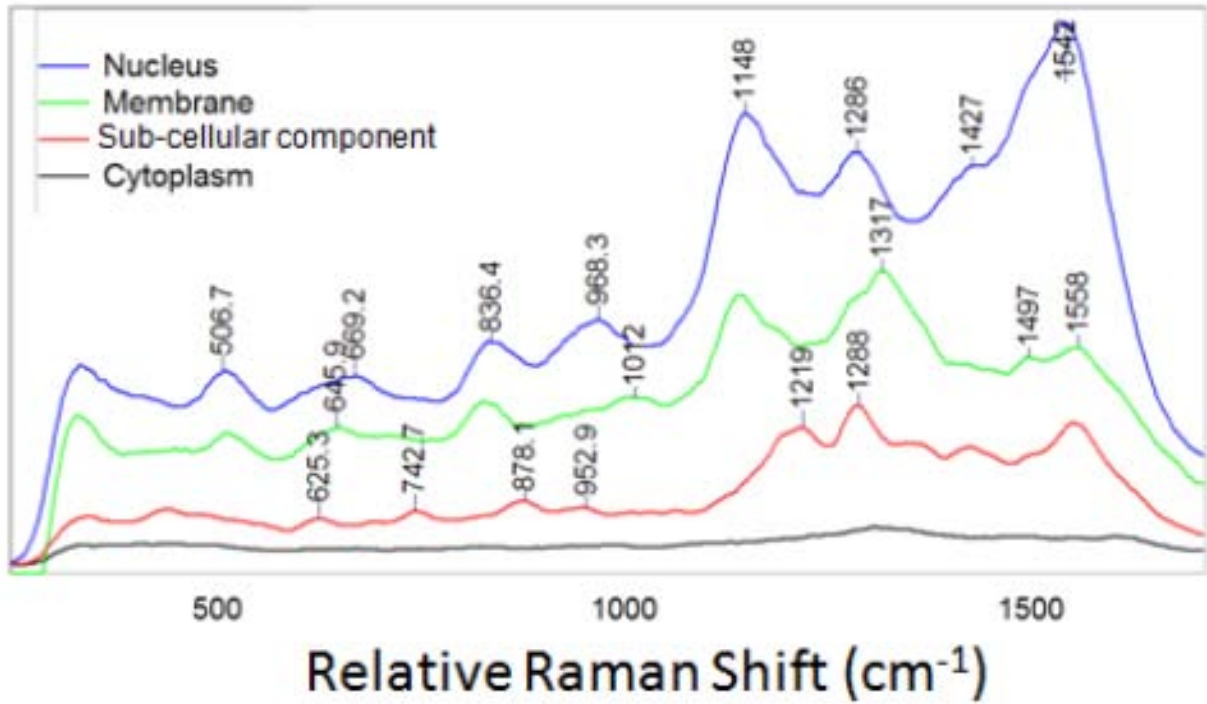


Figure 6.2.2. Raman spectra taken from a living hADAS cell at four different locations. Figure shows the DNA characteristic spectrum visible at the nucleus as compared to the lipid/protein spectra taken elsewhere.

Additionally, the Spec10 spectrometer (ActonPI) component of the Raman system utilizes two independent gradients that can easily be exchanged to improve resolution or overall scope as needed. The system's microRaman capabilities serve to minimize the spectral volume we analyze and the addition of pinholes further improves our confocal abilities (by sacrificing signal intensity). Thus a combination of experimental design and

system specification provide us the ability to focus on specific areas of interest and limit exposure to extraneous signal from an otherwise noisy chemical environment.

Other experiments will also attempt to collect Raman data from the nucleus of individual cells in order to monitor DNA content. At least seven cells within each population will be analyzed in order to gather a suitable amount of data for statistical analysis. Each cell will also be probed outside of the nucleus and in the immediate extra-cellular areas to gather information on any chemical changes that may be occurring in the cytoplasm, membrane, etc., as discussed above.

5. The most obvious way to analyze the data will be to look for differences in peak locations and overall peak intensity.⁵⁰ However, because nanoparticle-induced SERS amplification can cause variable intensity “hot spots”, additional approaches may be necessary. As shown in Chapter 5, a different strategy is to normalize the resulting Raman peaks to a particular peak of interest and then determine peak ratios relative to that peak. This will enable a determination of, as an example, the relative amount of phosphate in the cell with respect to the lipid or nitrogen content and should eliminate the detrimental variability of the SERS effect while still capitalizing on the intensity enhancement and noise reduction. Thus, with a combination of experiment and device design we should be able to determine statistically significant differences between the sample pools.

It is expected that this arrangement will combine the real-time measurement potential of Raman spectroscopy with the ability of microfluidics to quickly and rigidly control a culture's immediate chemical environment thereby leading to the collection of spatially and temporally localized chemical information. These characteristics are ideal for a variety of cellular analyses. It is expected that this research will lead to better measurement capabilities of intracellular chemistry and that this information will provide a more precise understanding of the intracellular chemical mechanisms involved in cell growth and apoptosis, cellular signaling, differentiation, cytotoxicity, motility, etc.

6.3 Multidimensional Analysis of SERS Data

Chapters 3 and 4 have shown Raman spectroscopy capable of detecting single nucleotide polymorphisms and polymorphic regions – genetic aberrations that can function as genetic markers for a variety of human ailments. Though uniquely useful in several such aspects, Raman spectroscopy and particularly surface enhanced Raman spectroscopy (SERS) are also plagued by high degrees of variability in the data these techniques generate, especially concerning biological samples.⁷ This variability reduces the amount of statistically significant conclusions that can be drawn from differential experiments and can limit certain Raman studies to the collection of purely qualitative data.

However, combining surface enhanced Raman spectroscopy with multidimensional analyses (MDA) such as Principal Component Analysis (PCA) and Linear Discriminate Analysis (LDA) can generally be used to discriminate between large sets of variable data and has been used to highlight otherwise imperceptible differences. The addition of multivariate data techniques to Raman experiments has been gaining popularity and has been used to differentiate vital tissue from necrotic tissue,⁴⁵ fetal tissue from juvenile tissue,¹⁰⁰ healthy tissue from cancerous tissue,^{2, 111} and to differentiate between living cells in different stages of the growth cycle.^{47, 53}

The short term goal of this direction is to further develop the collaboration between Raman spectroscopy and MDA with the aim of improving detection rubrics for cancer sub-

typing and genetic testing. Our preliminary experiments use a combination of PCA and LDA to quantifiably determine the sensitivity of data from the SERS genetic marker analysis originally presented in Chapter 4. As previously discussed, separate populations of DNA strands were analyzed with SERS. Each population was composed of DNA strands that were completely matched with respect to one another or that had specific nucleotide mismatches. While the SERS method was able to differentiate one population from another, the simple statistics involved provide little information about individual data points from within each population. Using MDA allows us to extract additional information from the data sets and to quantify the ability of this technique to detect and accurately classify these measurements. This effort represents a significant step forward in improving the technique for future iterations.

Initial MDA results are shown in the PCA plots in Figures 6.3.1- 6.3.3. Figure 6.3.1 represents a PCA analysis of the data originally used in Chapter 4 to determine significant differences between the four sample types. As before, the data has only been baseline subtracted from the local minimum at 200 to ~ 2000 relative cm^{-1} . The PCA plot shows the seven median spectra from each sample type to be spacially distinct and readily classifiable using LDA. From Table 6.3.1 it can be seen that whenever only two samples are directly compared, LDA is able to distinguish 100% between any two samples with the exception of

the SNP and DTM samples. However, when all four samples are compared together the sensitivity rates drop as seen in Table 6.3.1.

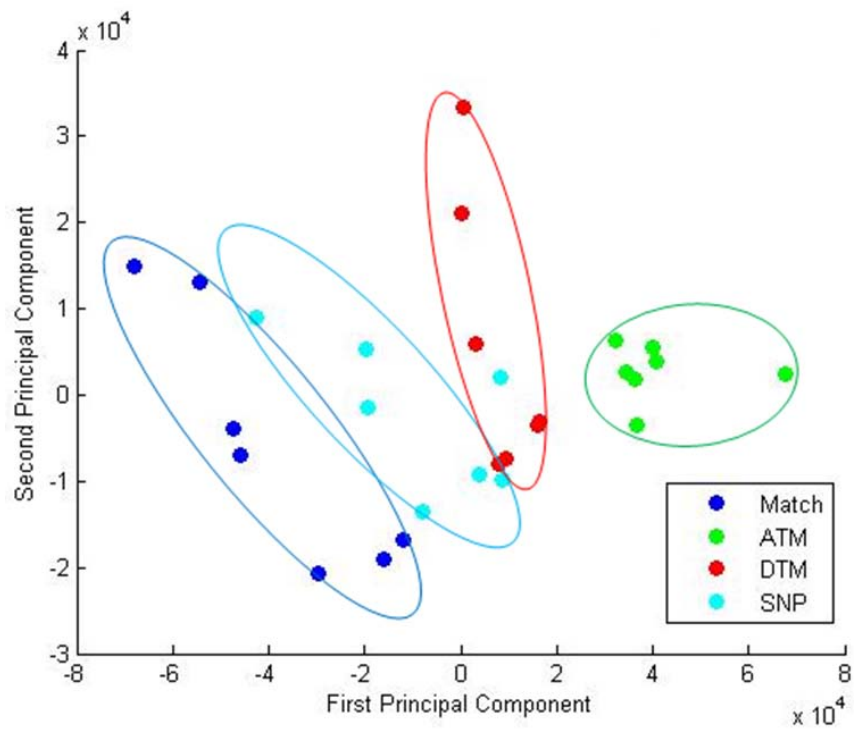


Figure 6.3.1. PCA scores of each sample type as plotted against the first and second principle components. Each data point represents one of the seven median spectra as discussed in Chapter 4. Data was baseline corrected prior to PCA.

Table 6.3.1. Sample type classification accuracy of the four-group PCA-LDA model as assessed by a leave-one-out cross-validation. The seven median spectra from each sample type were baseline subtracted prior to PCA-LDA analysis.

	Match	SNP	DTM	ATM
Sensitivity	100%	-	-	100%
	100%	-	86%	100%
	86%	71%	57%	100%
	100%	-	100%	-
	100%	86%	86%	-
	100%	86%	-	100%
	100%	100%	-	-
	-	-	100%	100%
	-	71%	57%	100%
	-	100%	-	100%
	-	86%	86%	-

To further evaluate the SERS method, MDA analyses were attempted on the entire 31 point data sets from each sample group. As a result, this analysis gives a degree of accuracy for particular points among all of the collected data. To do this the data was first baseline subtracted as above then normalized to the ubiquitous $\sim 840\text{ cm}^{-1}$ phosphate backbone peak. Using normalized data minimizes the effect that intensity fluctuations have on overall variability and allows for the observation of variability between samples with regard to more subtle factors such as peak ratios and positions shifts. As expected, including the entire data

set mostly decreases the sensitivities as shown in Table 6.3.2. Most notably, sensitivities for the matched sample drops to between 71-77% for all categories except when comparing matched and ATM, which retain high sensitivities at 87% and 97% respectively.

Table 6.3.2. Leave-one-out LDA cross validation sensitivities for classifying all 31 spectra from each sample group. Spectra were baseline subtracted and normalized prior to LDA analysis.

	Match	SNP	DTM	ATM
Sensitivity	87%	-	-	97%
	74%	-	88%	78%
	74%	78%	66%	78%
	74%	-	84%	-
	71%	78%	59%	-
	77%	94%	-	81%
	74%	97%	-	-
	-	-	91%	81%
	-	88%	69%	78%
	-	97%	-	84%
	-	81%	63%	-

Additional information from the different groupings can also be observed. For example, Figure 6.3.2 shows the PCA plots of the ATM and DTM samples compared alone (Figure 6.3.2a) and then in comparison to the SNP sample as well (Figure 6.3.2b). An LDA analysis is able to correctly classify 81% of the ATM and 91% of the DTM samples when

analyzed alone. When the single mismatch sample is also included those sensitivities drop to 78% and 69%, respectively. From this data it can be concluded that the single mismatch shares individual characteristics with the triple mismatched sets that the triple mismatched sets do not share with one another. Since the normalization procedures exclude intensity variability from exerting much influence, it can be deduced that simply having a mismatch causes the spectra to vary in one particular way. In addition, the number and arrangement of that mismatch further affects the spectral variability.

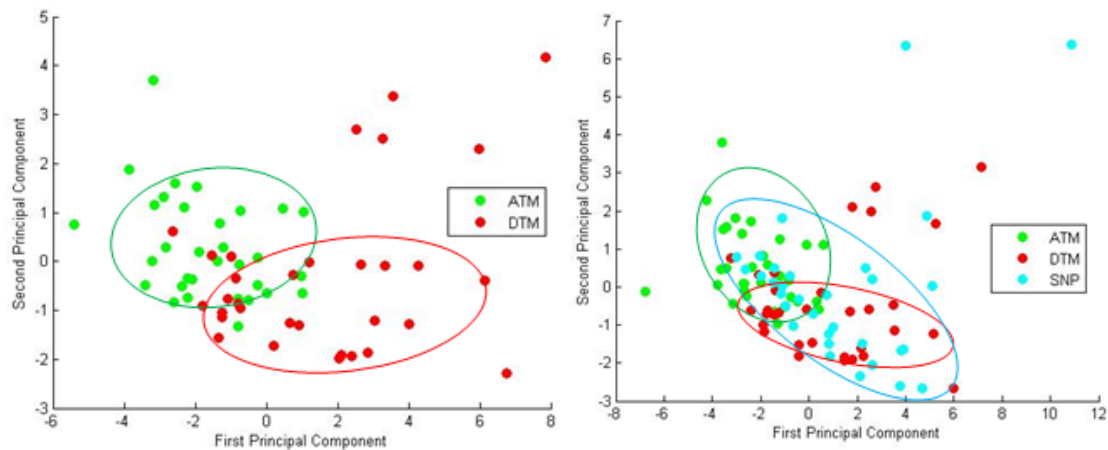


Figure 6.3.2. PCA scores of a) ATM and DTM sample types and of b) ATM, DTM, and SNP as plotted against the first and second principle components. The figure shows the similarities shared by the mismatched samples in general and contrasts the differences between the triple mismatched samples. Prior to PCA the data was baseline corrected and normalized to limit intensity variations thus highlighting variation between characteristic peaks.

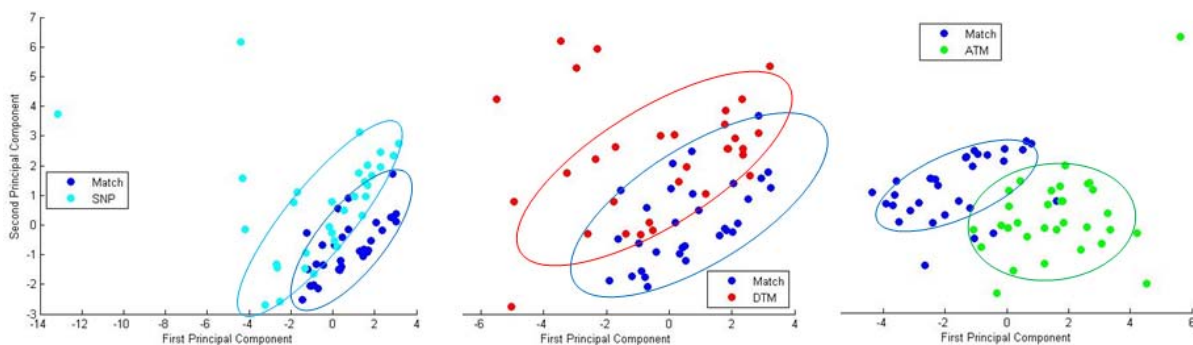


Figure 6.3.3. PCA scores of the matched samples as compared to the a) SNP, b) DTM, and c) ATM as plotted against the first and second principle components. Despite sharing expected similarities, the PCA groupings in this figure show how generally distinguishable the matched samples are from samples with polymorphisms. Prior to PCA the data was baseline corrected and normalized to limit intensity variations thus highlighting variation between characteristic peaks.

The remaining step in this direction is to determine a suitable outlier test that can be used to eliminate data points that stem from either experimental or systematic errors and that do not accurately represent the data on whole. It is predicted that such improvements to these methods will not only give the current SERS analysis a more quantifiable basis but they will also represent an enhanced ability to obtain more subtle information from the individual spectra and from the spectral differences. Advanced numerical analyses like these strengthen existing SERS approaches and further the potential for Raman-based techniques towards becoming viable clinical test methods and powerful academic research tools.

6.4 Intracellular SERS Targeting using Antibodies

The goal of this direction is to target precise cellular locations for SERS analyses. Previous research discussed in Chapter 5 represents an early step in intracellular SERS analyses. While it can be convenient that gold nanoparticles get sequestered into the endosomal pathway thereby creating a SERS environment within endosomes, it is also desirable to have the ability to observe chemical changes that occur elsewhere in the cell – specifically in individual organelles or around particular integrins on the plasma membrane, etc. One method of targeting in this way is to functionalize the nanoparticles with antibodies that either exclude the nanoparticles from entering the endosomal pathway or help to direct the destination of the nanoparticle to selected areas. By using antibodies to target the nanoparticles to a particular location it becomes theoretically possible to establish SERS environments around any cellular component that can be targeted by an antibody.

Our initial research on this front uses 40 nm gold nanoparticles functionalized with Monoclonal Anti-CD34 antibody (mouse). The CD34 antibody is designed to target the CD34 protein on the plasma membrane of certain mesenchymal stem cells yet not the plasma membrane of differentiated adipose cells. Therefore this experiment operates under the hypotheses that 1) anti-CD34 functionalized nanoparticles in cell cultures will bind to plasma membranes thus yielding different SERS spectra than those from non-functionalized nanoparticles sequestered in endosomes as seen in Chapter 5 and that 2) the Raman intensity

of these spectra will diminish as cells are differentiated towards an adipogenic lineage and the antibody/nanoparticles complexes disassociate from the molecular targets. This experiment would work as a control to determine if antibody functionalized nanoparticles can be used to create a SERS environment around targeted areas of interest.

Promisingly, standard spectra obtained from these experiments are substantially different from standard spectra seen in Chapter 5's earlier hASC experiments and from control spectra obtained from cell cultures dosed with non-functionalized nanoparticles (Figure 6.4.1). It is interesting to note that Raman spectra were relatively easy to obtain from undifferentiated hASCs and increasingly difficult to obtain once the cultures began to differentiate. This is attributed to the morphology changes described in Chapter 5 and to the predicted changes in the CD34 membrane proteins that lead to a disassociation between the protein and the antibody/nanoparticle complex. Of the spectra that were obtained, Figure 6.4.1 shows an average drop in intensity between cultures that were undifferentiated and those that were differentiated and an additional drop between cultures that were differentiated for longer periods of time, providing further support for the disassociation hypothesis.

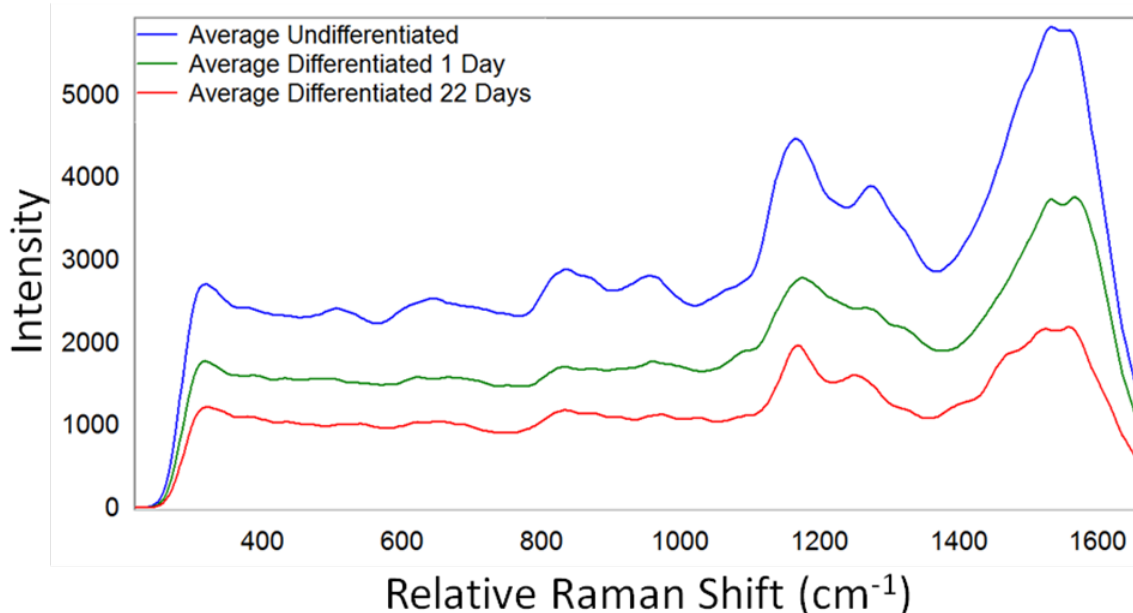


Figure 6.4.1. Raman spectra comparing the averaged Raman intensities of undifferentiated hASCs (blue) as compared to those that have been exposed to adipogenic differentiation medium for 1 day (green) and 22 days (red). The figure highlights the intensity reduction that is observed on average as the cell cultures differentiate. Spectra have been smoothed and baseline corrected.

Figure 6.4.2 shows an overlay of the same three spectra normalized to the peak ~ 1170 cm^{-1} . From this figure it is not obvious what conclusions can be drawn about chemical changes that SERS is able to detect during differentiation. Unlike observing characteristic chemical changes from within the cell's endosome, the plasma membrane is either a less useful vantage point or the spectra that were obtained merely represent spectra from cells that have yet to fully differentiate. Therefore as the cells differentiate there is likely a transitional period in which nanoparticles have begun to disassociate leaving behind only enough

nanoparticles to create enhanced spectra (of reduced intensity) but not enough to enable the enhancement of subtly emerging chemical complexes. It is also possible that though the plasma membrane is certainly subject to changes in integrin quantity and type during adipogenesis, the overall chemical makeup may not experience chemical fluctuations that are large enough or stable enough to be detected by SERS.

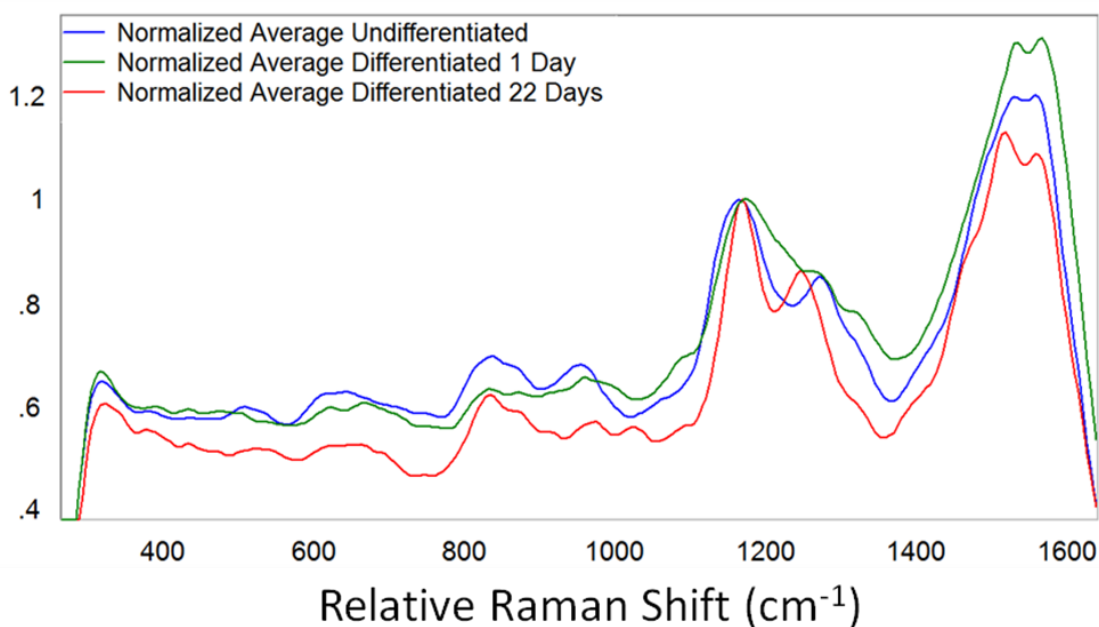


Figure 6.4.2. Raman spectra comparing the normalized average Raman intensities of undifferentiated hASCs (blue) as compared to those that have been exposed to adipogenic differentiation medium for 1 day (green) and 22 days (red). The figure highlights spectral similarities shared between the three groups. Spectra have also been smoothed and baseline corrected.

The next step is to identify antibodies that can target areas where differential activity can be observed, as opposed to experiments where the chemical change simply results in a signal reduction. It has been proposed that Anti-MyF5 antibody (rabbit) will target membrane-bound proteins yet unlike Anti-CD34, MyF5 will not disengage during adipogenesis. This experiment will provide an obvious contrast to CD34 experiments in terms of signal intensity spectra variation. As these early experiments prove, targeting the nanoparticles to appropriate areas within the cell is an important consideration in cellular SERS experiments. In the future, antibody targeting will enable closer SERS analyses of specific activities cellular respiration, protein production, and apoptosis as they occur in specific locations of the cell.

Chapter 7: Conclusions

Using Raman spectroscopy as a detection technique is a viable solution for investigating some of biology's unanswered or underanswered questions. This research has been primarily focused on exploring different avenues through which this is made possible. For example, probing the electronic and optical properties of nanogaps provides a fundamental tool for biomedical exploration that is capable of high speed electronic detection and of collecting molecular information using SERS. By using a combination of oligo-based molecular lithography and conventional photolithography to create these substrates we have identified a cost-effective procedure for producing nanogaps on the wafer scale and as such, we have simultaneously shown a protocol that allows for a gap size that can be tuned to distances between just a few nanometers to approximately 40 nm. In addition to SERS enhancements, these nanogaps also exhibit sensitive electronic detection capabilities for quickly and inexpensively probing charge transfer at the nanogap. For future detection devices this invites the possibility of nanogap arrays for deposition experiments and nanogap integrated microfluidic designs for flow-through analyte detection.

Next we tested a specific biomedical application of SERS detection by identifying a preliminary method of using SERS to detecting mid-sequence SNPs. Again focusing on the creation of statistically significant data, photolithographically defined substrates were designed to couple with a simple surface chemistry procedure and used to create an array of

SERS substrates. Upon these substrates moderate length oligos were positioned into Raman enhancing complexes and SERS was used to detect spectroscopic differences that arise from oligos containing SNPs. A simple data analysis rubric combined with a Student's t-test was then able to statistically differentiate oligos containing SNPs from those without. The overall process proved to be inexpensive and relatively fast.

Because the underlying concept of this technique essentially provides a generic method for spectroscopically identifying oligonucleotide differences in an array format, the next step was to broaden the technique's scope and further test the range of its applicability. To do this we examined two polymorphisms in addition to SNPs and we devised a scheme by which the test oligos no longer needed expensive thiol modifications. These changes make the experiments more amenable to clinical applications such as genetic marker detection and potentially improve the fundamental knowledge of mismatch chemistry in DNA mutations. Using intensity results from the SERS data, we were able to detect and statistically differentiate between oligo samples with single nucleotide polymorphisms, those with a three nucleotide polymorphic region, and those with three single polymorphisms separated throughout the sequence. Characteristic peak position shifts supplied further information as to how particular polymorphisms were possibly arranged on the molecular level.

In our ever broadening application of SERS technologies, we finally attempted to use SERS to explore the chemistry involved in the differentiation of living human adipose

derived adult stem cells. In a period of time in which the cells were differentiated down an adipogenic pathway, SERS spectra were collected from within the endosomes of the stem cells. Results show that SERS can be used to effectively monitor the relative activity of several biochemical process involved in adipogenesis. Future applications are expected to enable advanced biomedical research beyond this model system. Continuous monitoring of this type enables the measurement natural cellular responses to ordinary life situations as well as chemical and pathological stimulation.

Whether using DNA to fabricate nanodevices or using nanotechnology to investigate biological systems, my research represents only a small niche in biomedical engineering aimed at improving the scope of existing analytical techniques and at further exploring relevant fundamental questions in biology, chemistry, and physics. The real beauty of such an ambitious objective is the limitless directions in which it can be taken and the possibility of future exploration.

References

1. Fujita, K. *et al.* Time-resolved observation of surface-enhanced Raman scattering from gold nanoparticles during transport through a living cell. *Journal of Biomedical Optics* **14**, 024038-1-024038-7 (2009).
2. Kast, R. E. *et al.* Raman spectroscopy can differentiate malignant tumors from normal breast tissue and detect early neoplastic changes in a mouse model. *Biopolymers* **89**, 235-241 (2008).
3. Ong, C. W., Shen, Z. X., He, Y., Lee, T. & Tang, S. H. Raman Microspectroscopy of the Brain Tissues in the Substantia Nigra and MPTP-induced Parkinson's Disease. *J. Raman Spectrosc.* **30**, 91-96 (1999).
4. O'Neill, A. T., Monteiro-Riviere, N. A. & Walker, G. M. Characterization of microfluidic human epidermal keratinocyte culture. *Cytotechnology* **56**, 197 (2008).
5. McDonald, J. C. *et al.* Fabrication of microfluidic systems in poly(dimethylsiloxane). *Electrophoresis* **21**, 27 (2000).
6. Ferraro, J. R., Nakamoto, K. & Brown, C. W. in *Introductory Raman spectroscopy* 434 (Academic Press, Boston, 2003).
7. Hanlon, E. B. *et al.* Prospects for *in vivo* Raman spectroscopy. *Phys. Med. Biol.* **45**, R1-59 (2000).
8. Pappas, D., Smith, B. W. & Winefordner, J. D. Raman spectroscopy in bioanalysis. *Talanta* **51**, 131 (2000).
9. Liu, C. H. *et al.* Raman, fluorescence, and time-resolved light scattering as optical diagnostic techniques to separate diseased and normal biomedical media. *J. Photochem. Photobiol. B: Biol.* **16**, 187 (1992).
10. Gut, I. G. Automation of Genotyping of Single Nucleotide Polymorphisms. *Human Mutation* **17**, 475 (2001).
11. Zhang, J. *et al.* SNPdetector: A Software Tool for Sensitive and Accurate SNP Detection. *PLOS Computational Biology* **1**, 0395-0404 (2005).

12. Cao, Y. C., Jin, R. & Mirkin, C. A. Nanoparticles with Raman Spectroscopic Fingerprints for DNA and RNA Detection. *Science* **297**, 1536-1540 (2002).
13. Song, L., Hennink, E. J., Young, I. T. & Tanke, H. J. Photobleaching kinetics of fluorescein in quantitative fluorescence microscopy. *Biophys. J.* **68**, 2588 (1995).
14. Polubotko, A. M. The phenomenon of single-molecule detection by the SERS method and SERS quadrupole theory. *Journal of Optics A: Pure and Applied Optics* **1**, L18-L20 (1999).
15. Polubotko, A. M. SERS phenomenon as a manifestation of quadrupole interaction of light with molecules. *Physics Letters A* **146**, 81-84 (1990).
16. Leopold, N. *et al.* Raman spectroscopic and DFT theoretical study of 4-(2-pyridylazo) resorcinol and its complexes with zinc(II) and copper(II). *Journal of Molecular Structure* **919**, 94-99 (2009).
17. Jia, T. *et al.* A study of surface enhanced Raman scattering for furfural adsorbed on silver surface. *Journal of Molecular Structure* **873**, 1-4 (2008).
18. Zhang, L., Bai, Y., Shang, Z., Zhang, Y. & Mo, Y. Experimental and theoretical studies of Raman spectroscopy on 4-mercaptopyridine aqueous solution and 4-mercaptopyridine/Ag complex system. *Journal of Raman Spectroscopy* **38**, 1106-1111 (2007).
19. Karabacak, M., Cinar, M., Coruh, A. & Kurt, M. Theoretical investigation on the molecular structure, Infrared, Raman and NMR spectra of parahalogen benzenesulfonamides, 4-X-C₆H₄SO₂NH₂ (X=Cl, Br or F). *Journal of Molecular Structure* **919**, 26-33 (2009).
20. Zhu, W., Wei, T., Zhang, X. & Xiao, H. Density functional theory study of structural, vibrational, and thermodynamic properties of crystalline 2,4-dinitrophenol, 2,4-dinitroresorcinol, and 4,6-dinitroresorcinol. *Journal of Molecular Structure: THEOCHEM* **895**, 131-137 (2009).
21. Mulvaney, S. P., He, L., Natan, M. J. & Keating, C. D. Three-layer substrates for surface-enhanced Raman scattering: preparation and preliminary evaluation. *J. Raman Spectrosc.* **34**, 163-171 (2003).
22. Gunnarsson, L. *et al.* Interparticle coupling effects in nanofabricated substrates for surface-enhanced Raman scattering. *Applied Physics Letters* **78**, 802 (2001).

23. Etchegoina, P. *et al.* Electromagnetic contribution to surface enhanced Raman scattering revisite. *Journal of Chemical Physics* **19**, 5281 (2003).
24. Barhoumi, A., Zhange, D., Tam, F. & Halas, N. J. Surface-Enhanced Raman Spectroscopy of DNA. *J. AM. CHEM. SOC.* **130**, 5523 (2008).
25. Ward, D. R. *et al.* Electromigrated nanoscale gaps for surface-enhanced Raman spectroscopy. *Nano Letters* **7**, 1396-1400 (2007).
26. Ward, D. R. *et al.* Simultaneous measurements of electronic conduction and Raman response in molecular junctions. *Nano Letters* **8**, 919-924 (2008).
27. Sun, L., Yu, C. & Irudayaraj, J. Raman Multiplexers for Alternative Gene Splicing. *Anal. Chem.* **80**, 3342-3349 (2008).
28. Sun, L., Yu, C. & Irudayaraj, J. Surface-Enhanced Raman Scattering Based Nonfluorescent Probe for Multiplex DNA Detection. *Anal. Chem.* **79**, 3981 (2007).
29. Claustres, M. in *Guide to Mutation Detection* (eds Taylor, G. R. & Day, I. N.) 9-10 (John Wiley & Sons, Inc., Hoboken, New Jersey, 2005).
30. Dudoit, S. & van der Laan, Mark J. in *Multiple Testing Procedures with Applications to Genomics* 489 (Springer, New York, 2008).
31. Bell, G. I., Karam, J. H. & Rutter, W. J. Polymorphic DNA region adjacent to the 5' end of the human insulin gene. *Proc. Natl. Acad. Sci. USA* **78**, 5759 (1981).
32. Zeller, G. *et al.* Detecting polymorphic regions in Arabidopsis thaliana with resequencing microarrays. *Genome Res.* **18**, 918 (2008).
33. Klungland, A., Laerdahl, J. K. & Rognes, T. in *Oxidative Damage to Nucleic Acids* (eds Evans, M. D. & Cooke, M. S.) 75 (Springer, New York, 2007).
34. Horaitis, R. & Cotton, R. G. H. in *Guide to Mutation Detection* (eds Taylor, G. R. & Day, I. N.) 107-109 (John Wiley & Sons, Inc., Hoboken, New Jersey, 2005).
35. Parsons, J. L., Boswell, E. & Dianov, G. L. in *Oxidative Damage to Nucleic Acids* (eds Evans, M. D. & Cooke, M. S.) 86 (Springer, New York, 2007).

36. Gut, I. G. in *Guide to Mutation Detection* (eds Taylor, G. R. & Day, I. N.) 117-119 (John Wiley & Sons, Inc., Hoboken, New Jersey, 2005).
37. Dubertret, B., Calame, M. & Libchaber, A. J. Single-mismatch detection using gold-quenched fluorescent oligonucleotides. *Nature Biotechnology* **19**, 365 (2001).
38. Sato, K., Sawayanagi, M., Hosokawa, K. & Maeda, M. Single-base Mutation Detection Using Neutravidin-modified Polystyrene Nanoparticle Aggregation. *Analytical Sciences* **20**, 893 (2004).
39. Kneipp, K., Kneipp, H., Itzkan, I., Dasari, R. R. & Feld, M. S. Surface-Enhanced Raman Scattering and Biophysics. *J. Phys. : Condens. Matter* **14**, R597-R624 (2002).
40. Kneipp, K. *et al.* Detection and Identification of a Single DNA Base Molecule Using Surface-Enhanced Raman Scattering (SERS). *Physical Review E* **57**, R6281-R6284 (1998).
41. Lord, R. C. & Yu, N. T. Laser-excited Raman spectroscopy of biomolecules. I. Native lysozyme and its constituent amino acids. *J. Mol Biol* **50**, 509-524 (1970).
42. Premasiri, W. R. *et al.* Characterization of the Surface Enhanced Raman Scattering (SERS) of Bacteria. *J Phys Chem B* **109**, 312-320 (2005).
43. Premasiri, W. R., Moir, D. T., Lkempner, M. S. & Ziegler, L. D. Surface-Enhanced Raman Scattering of Microorganisms. *A.C.S. Symposium Series* **963**, 164-185 (2007).
44. Wood, B. R. *et al.* Resonance Raman microscopy in combination with partial dark-field microscopy lights up a new path in malaria diagnostics. *The Analyst* **134**, 1119-1125 (2009).
45. Koljenovic, S. *et al.* Discriminating Vital Tumor from Necrotic Tissue in Human Glioblastoma Tissue Samples by Raman Spectroscopy. *Laboratory Investigation* **82**, 1265-1277 (2002).
46. Nablev, I. R., Morjani, H. & Manfait, M. Selective analysis of antitumor drug interaction with living cancer cells as probed by surface-enhanced Raman spectroscopy. *Eur Biophys J* **19**, 311-316 (1991).
47. Swain, R. J., Jell, G. & Stevens, M. A. Non-invasive analysis of cell cycle dynamics in single living cells with Raman micro-spectroscopy. *J. Cell. Biochem.* **104**, 1427-1438 (2008).

48. Swain, R. J. & Stevens, M. M. Raman microspectroscopy for non-invasive biochemical analysis of single cells. *Biochem. Soc. Trans.* **35**, 544-549 (2007).
49. Notingher, I. *et al.* In situ characterisation of living cells by Raman spectroscopy. *Spectroscopy* **16**, 43-51 (2002).
50. Notingher, I., Bisson, I., Polak, J. M. & Hench, L. L. In situ spectroscopic study of nucleic acids in differentiating embryonic stem cells. *Vibrational Spectroscopy* **35**, 199-203 (2004).
51. Chan, J. W., Lieu, D., Huser, T. & Li, R. A. Label-Free Separation of Human Embryonic Stem Cells and Their Cardiac Derivatives Using Raman Spectroscopy. *Anal. Chem.* **81**, 1324-1331 (2009).
52. Moody, B. & McCarty, G. S. Statistically Significant Raman Detection of Midsequence Single Nucleotide Polymorphisms. *Anal. Chem.* **81**, 2013-2016 (2009).
53. Notingher, I. *et al.* Multivariate analysis of Raman spectra for in vitro non-invasive studies of living cells. *Journal of Molecular Structure* **744**, 179 (2005).
54. Nijssen, A. *et al.* Discriminating Basal cell carcinoma from its Surrounding Tissue by Raman Spectroscopy. *The Journal of Investigative Dermatology* **19**, 64 (2002).
55. Notingher, I. *et al.* In Situ Spectral Monitoring of mRNA Translation in Embryonic Stem Cells during Differentiation in Vitro. *Anal. Chem.* **76**, 3185 (2004).
56. Huang, D. *et al.* Highly efficient cellular labeling of mesoporous nanoparticles in human mesenchymal stem cells: implication for stem cell tracking. *The FASEB Journal*, 1-24 (2005).
57. Gentleman, E. *et al.* Comparative materials differences revealed in engineered bone as a function of cell-specific differentiation. *Nature Materials* **8**, 763-770 (2009).
58. McCarty, G. S. Molecular Lithography for Wafer-Scale Fabrication of Molecular Junctions. *Nano Letters* **4**, 1391 (2004).
59. Hatzor, A. & Weiss, P. S. Molecular Rulers for Scaling Down Nanostructures. *Science* **291**, 1019 (2001).

60. Tinland, B., Pluen, A., Sturm, J. & Weill, G. Persistence Length of Single-Stranded DNA. *Macromolecules* **30**, 5763 (1997).
61. Liu, B. *et al.* Controllable nanogap fabrication on microchip by chronopotentiometry. *Electromchimica Acta* **50** (2005).
62. Liang, X. & Chou, S. Y. Nanogap Detector Inside Nanofluidic Channel for Fast Real-Time Label-Free DNA Analysis. *Nano Lett* **8**, 1472 (2008).
63. McCarty, G. S., Moody, B. & Zachek, M. K. Enhancing electrochemical detection by scaling solid state nanogaps. *Journal of Electroanalytical Chemistry* **643**, 9-14 (2010).
64. Zheng, G., Qin, L. & Mirkin, C. A. Spectroscopically Enhancing Electrical Nanotraps. *Angew. Chem. Int. Ed.* **47**, 1938 (2008).
65. Muller, C. J., van Ruitenbeek, J. M. & de Jongh, L. J. Conductance and Supercurrent Discontinuities in Atomic-Scale Metallic Constrictions of Variable Width. *Physical Review Letters* **69**, 140 (1992).
66. Reed, M. A., Zhou, C., Muller, C. J., Burgin, T. P. & Tour, J. M. Conductance of a Molecular Junction. *Science* **278**, 252 (1997).
67. Qin, L., Park, S., Huang, L. & Mirkin, C. A. On-Wire Lithography. *Science* **309**, 113 (2005).
68. Wei, D. *et al.* Real Time and in Situ Control of the Gap Size of Nanoelectrodes for Molecular Devices. *Nano Letters* **8**, 1625 (2008).
69. Ferrari, A. C. & Robertson, J. Interpretation of Raman spectra of disordered and amorphous carbon. *Physical Review B* **60**, 14095 (2000).
70. Knight, D. S. & White, W. B. Characterization of diamond films by Raman spectroscopy. *J. Mater. Res.* **4**, 385 (1989).
71. Jang, N. H. The Coordination Chemistry of DNA Nucleosides on Gold Nanoparticles as a Probe by SERS. *Bull. Korean chem. Soc.* **23**, 1790-1800 (2002).
72. Endres, R. G., Cox, D. L. & Singh, R. R. P. Colloquium: The quest for high-conductance DNA. *Rev. Mod. Phys.* **76**, 195 (2004).

73. van Zalinge, H. *et al.* Single-Molecule Conductance Measurements of Single- and Double-Stranded DNA Oligonucleotides. *ChemPhysChem* **7**, 94 (2006).
74. Carey, P. R. Raman Spectroscopy, the Sleeping Giant in Structural Biology, Awakes. *The Journal of Biological Chemistry* **274**, 26625 (1999).
75. Carey, P. R. Resonance Raman Labels and Raman Labels. *The Journal of Raman Spectroscopy* **29**, 861 (1998).
76. Otto, C., van den Tweel, T. J. J., de Mul, F. F. M. & Greve, J. Surface-Enhanced Raman Spectroscopy of DNA Bases. *Journal of Raman Spectroscopy* **17**, 289-298 (1986).
77. Tu, A. T. in *Raman Spectroscopy in Biology: Principles and applications* 134-153 (John Wiley & Sons, Inc, New York, 1982).
78. Gearheart, L. A., Ploehn, H. J. & Murphy, C. J. Oligonucleotide adsorption to gold nanoparticles: A surface-enhanced raman spectroscopy study of intrinsically bent DNA. *J Phys Chem B* **105**, 12609-12615 (2001).
79. Syvanen, A. & Soderlund, H. DNA sandwiches with silver and gold. *Nature Biotechnology* **20**, 349 (2002).
80. Syvanen, A. Accessing Genetic Variation: Genotyping Single Nucleotide Polymorphisms. *Nature Reviews Genetics* **2**, 30 (2001).
81. Mir, K. U. & Ragoussis, J. in *PCR Technology: Current Innovations* (eds Weissensteiner, T., Griffin, H. G. & Griffin, A.) 98 (CRC Press, Washington, D.C., 2004).
82. Park, S., Lazarides, A. A., Storhoff, J. J., Pesce, L. & Mirkin, C. A. The Structural Characterization of Oligonucleotide-Modified Gold Nanoparticle Networks Formed by DNA Hybridization. *J Phys Chem B* **108**, 12375 (2004).
83. Park, S., Brown, K. A. & Hamad-Schifferli, K. Changes in Oligonucleotide Conformation on Nanoparticle Surfaces by Modification with Mercaptohexanol. *Nano Letters* **4**, 1925 (2004).
84. Ke, W., Yu, D. & Wu, J. Raman spectroscopic study of the influence on herring sperm DNA of heat treatment and ultraviolet radiation *Spectrochimica Acta Part A: Molecular and Biomolecular Spectroscopy* **55**, 1081 (1999).

85. Krafft, C., Hinrichs, W., Orth, P., Saenger, W. & Welfle, H. Interaction of Tet Repressor with Operator DNA and with Tetracycline Studied by Infrared and Raman Spectroscopy. *Biophys. J.* **74**, 63 (1998).
86. Pitt, G. D. *et al.* Engineering Aspects and Applications of the New Raman Instrument. *IEE Proc-Sci. Meas. Technol.* **152**, 241-318 (2005).
87. Lafleur, L., Rice, J. & Thomas, G. J. J. Raman Studies of Nucleic Acids. VII. Poly A · Poly U and Poly G · Poly C. *Biopolymers* **11**, 2423 (1972).
88. Turner, D. H., Sugimoto, N., Kierzek, R. & Dreiker, S. D. RNA Structure Prediction. *Annu. Rev. Biophys. Biophys. Chem.* **17**, 167 (1988).
89. Bloomfield, V. A., Crothers, D. M. & Tinoco Jr., I. Nucleic Acids: Structures, Properties, and Functions. (2000).
90. Chithrani, B. D., Ghazani, A. A. & Chan, W. C. W. Determining the Size and Shape Dependence of Gold Nanoparticle Uptake into Mammalian Cells. *Nano Lett* **6**, 662-668 (2006).
91. Shamsaie, A., Heim, J., Yanik, A. A. & Irudayaraj, J. Intracellular quantification by surface enhanced Raman spectroscopy. *Chemical Physics Letters* **461**, 131-135 (2008).
92. Kneipp, K. *et al.* Surface-Enhanced Raman Spectroscopy in Single Living Cells Using Gold Nanoparticles. *Applied Spectroscopy* **56**, 150-154 (2002).
93. Kneipp, J., Kneipp, H. & Kneipp, K. in (ed Kneipp, K.) 186-199 (American Chemical Society, Washington, DC, 2007).
94. Kneipp, J., Kneipp, H., Rice, W. L. & Kneipp, K. Optical Probes for Biological Applications Based on Surface-Enhanced Raman Scattering from Indocyanine Green on Gold Nanoparticles. *Anal. Chem.* **77**, 2381-2385 (2005).
95. Van, R. L. R., Bayliss, C. E. & Roncari, D. A. K. Cytological and enzymological characterization of adult human adipocyte precursors in culture. *F. Clin. Invest.* **6**, 699 (1976).
96. Gimble, J. M. & Guilak, F. Adipose-derived adult stem cells: isolation, characterization, and differentiation potential. *Cytotherapy* **5**, 362 (2003).

97. Hutley, L. J., Newell, F. S., Suchting, S. J. & Prins, J. B. in *Primary Mesenchymal Cells* (eds Koller, M. R., Palsson, B. & Masters, J. R. W.) 173-187 (Springer-Verlag New York, LLC, New York, 2001).
98. Angel, A., Hollenberg, C. H. & Roncari, D. A. K. The Adipocyte and Obesity: Cellular and Molecular Mechanisms. , 309 (1983).
99. Kneipp, J., Kneipp, H., McLaughlin, M., Brown, D. & Kneipp, K. In Vivo Molecular Probing of Cellular Compartments with Gold Nanoparticles and Nanoaggregates. *Nano Lett* **6**, 2225-2231 (2006).
100. Kim, B. S. *et al.* Growth, Differentiation, and Biochemical Signatures of Rhesus Monkey Mesenchymal Stem Cells. *Stem Cells and Development* **17**, 185-198 (2008).
101. de Aza, P. N. *et al.* Vibrational Properties of Calcium Phosphate Compounds. 1. Raman Spectrum of B-Tricalcium Phosphate. *Chem. Mater.* **9**, 912-915 (1997).
102. Nakamura, K. *et al.* Conformational changes in seventeen cystine disulfide bridges of bovine serum albumin proved by Raman spectroscopy. *FEBS Letters* **417**, 375-378 (1997).
103. Dikic, I. Endosomes: Molecular Biology Intelligence Unit. , 157 (2006).
104. Yang, D. *et al.* cAMP/PKA Regulates Osteogenesis, Adipogenesis and Ratio of RANKL/OPG mRNA Expression in Mesenchymal Stem Cells by Suppressing Leptin. *PLoS One* **3**, e1540-1-e1540-10 (2008).
105. Bennett, C. N. *et al.* Regulation of Wnt Signaling during Adipogenesis. *Journal of Biological Chemistry* **277**, 30998-31004 (2002).
106. MacDougald, O. A. & Lane, M. D. Transcriptional Regulation of Gene Expression During Adipocyte Differentiation. *Annu. Rev. Biochem.* **64**, 345-373 (1995).
107. Murayama, T. & Ui, M. [³H]GDP Release from Rat and Hamster Adipocyte Membranes Independently Linked to Receptors Involved in Activation or Inhibition of Adenylate Cyclase. *The Journal of Biological Chemistry* **259**, 761-769 (1984).
108. Roelen, B. A. J. & Dijke, P. t. Controlling mesenchymal stem cell differentiation by TGF-beta family members. *Journal of Orthopaedic Science* **8**, 740-748 (2003).

109. Steel, A. B., Levicky, R. L., Herne, T. M. & Tarlov, M. J. Immobilization of Nucleic Acids at Solid Surfaces: Effect of Oligonucleotide Length on Layer Assembly. *Biophysical Journal* **79**, 975 (2000).
110. Walker, G. M., Monteiro-Riviere, N. A., Rouse, J. & O'Neill, A. T. A linear dilution microfluidic device for cytotoxicity assays. *Lab Chip* **7**, 226 (2007).
111. Nijssen, A. *et al.* Discriminating Basal Cell Carcinoma from its Surrounding Tissue by Raman Spectroscopy. *The Journal of Investigative Dermatology* **119**, 64 (2002).
112. Whitesides, G. M., Ostuni, E., Takayama, S., Jiang, X. & Ingber, D. E. Soft lithography in biology and biochemistry. *Annu. Rev. Biomed. Eng.* **3**, 335 (2001).
113. http://www.bme.ncsu.edu/labs/tbl/documents/su8_2050_laurell_procedure.pdf.
114. http://www.bme.ncsu.edu/labs/tbl/documents/pdms_molding.pdf.
115. Lee, J. N., Park, C. & Whitesides, G. M. Solvent Compatibility of Poly(dimethylsiloxane)-Based Microfluidic Devices. *Anal. Chem.* **75**, 6544 (2003).
116. Shin, Y. S. *et al.* PDMS-based micro PCR chip with Parylene coating. *J. Micromech. Microeng* **13**, 768 (2003).

Appendix

A. Soft Lithography Protocol

The process of soft lithography micromolding is a multiple-step process that can theoretically be made as simple or complex as desired. In its simplest form however, soft lithography will have three basic steps – 1) creating a master, 2) molding the PDMS, and 3) assembling the micromolded device. Note: An updated procedure for micromolding can be obtained from the McCarty/Walker lab and in the references listed below.

- 1) A “master” is the patterned wafer that the PDMS will be molded around to form the imprinted channels in the PDMS. The three basic steps to create a master are shown schematically Figure A1.

A) A computer assisted design (CAD) program is

used to create a design file that is sent to a printer for the production of a photolithography mask. Adobe Illustrator is commonly used to design low resolution masks

while a program like L-Edit may be required for higher resolutions.

Commercial printers like Film Graphics (Raleigh, NC) or FineLine Imaging (Colorado Springs, CO) then print the mask. Low resolution masks generally require a film output with a 3556 DPI resolution and a positive tone.

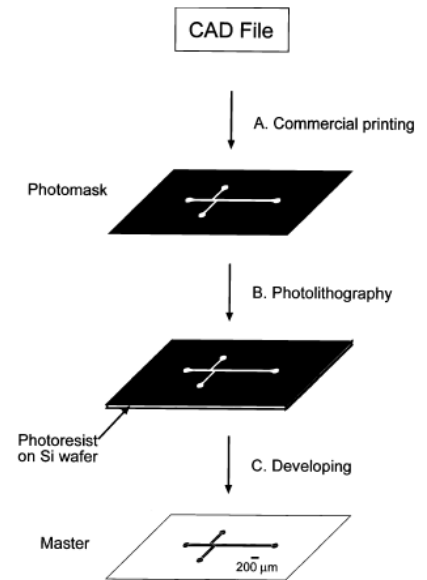


Figure A1. Schematic outlining the four steps used to create a master wafer for soft lithography.⁴

- B) The photolithography step is arguably the most involved step in creating a master. There are several papers that offer very specific guides to this process^{4, 5, 110, 112} as well as a website¹¹³ whose methods have been tested on many occasions. In general the master is created by spinning negative tone photoresist of desired thickness onto clean diameter silicon wafer (University Wafers). The wafer is then baked (Post Application Bake), placed directly under the CAD mask, and exposed to UV light for a set interval using something like a Blak-Ray B-100A UV lamp (UVP). The wafer is baked again (Post Exposure Bake).
- C) Finally the wafer is submerged in an appropriate developer until the pattern fully develops. The process is completed by rinsing the wafer in isopropyl alcohol (IPA).

The specifics of this protocol are governed by the size of the features that is desired in the resulting mold. For example, 50 μm high channels can be created using a SU8-2050 resist (Microchem). The other variables should be set as follows:

- Spin speed: spin at 500 rpm for 10 s then 2000 rpm for 30 s.
- Post application bake: 95 °C for 35 min.
- Exposure time: 60 s.
- Post exposure bake: 95 °C for 45 min.

- Developr: in SU8-Developer (Microchem) for ~ 7 min or until pattern develops.
- 2) Again, creating the PDMS mold is covered in far greater depth elsewhere.^{4, 110, 112,}
¹¹⁴ Generally the process is to mix about 16 g of a PDMS pre-polymer with about 1.6 g of a curing agent (SYLGARD 184 Silicone Elastomer Kit, Dow Corning) and then stir the mixture for ~ 5 minutes. Next, the mixture is degassed in a desiccator before carefully (smoothly) pouring it over the master wafer. Keep in mind the edges of the master wafer must be suitably confined in a petri dish or molded foil container to ensure the PDMS remains pooled on top of the master as it cures. Finally, bake the master/PDMS for 2.5 hours at 80 °C. After baking, when the PDMS no longer flows, it can be carefully peeled off of the master wafer.

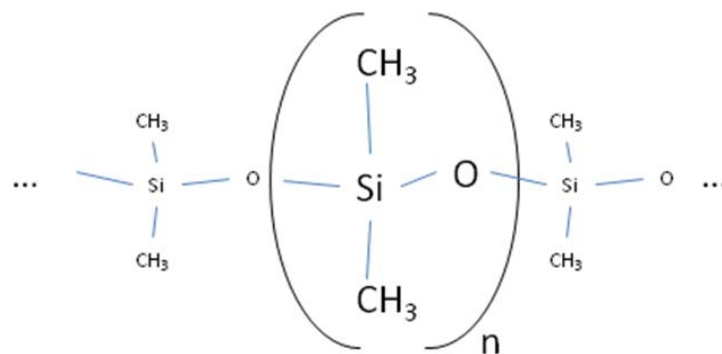


Figure A2. Chemical structure of PDMS.

- 3) The final step is to bond the PDMS to a substrate, usually either a glass slide or another silicon wafer. For non-permanent bonding this is simply done by pressing the mold and substrate together with gentle, even pressure. For a more permanent bond, both the mold and the substrate can be exposed to a weak oxygen plasma for 30 to 60 s before bonding.¹¹⁰

Of course, depending on the specific pattern and purpose of the device there may be additional steps such as boring out fluid reservoirs or plumbing the device to a pump or analysis tool. Nonetheless, the above procedure represents the usual process steps that are used to make a PDMS microfluidics device using soft lithography.

Note: Using solvents within the PDMS channels could be problematic depending on exactly what the solvents. Some solvents have been shown to swell the polymer while others promote dissolution of PDMS oligomers into the solvent stream.¹¹⁵ According to a 2003 Analytical Chemistry paper¹¹⁵ water, nitromethane, ethylene glycol, or acetonitrile are generally acceptable for use as solvents. The use of triethylamine, pentane, and xylenes is not recommended. However, studies have shown that longevity and chemical resistance of the PDMS can be increased by coating the polymer with a thin (~ 5 μm) Parylene film.¹¹⁶

B. Photolithography Protocol

B.1. Photoresist Application

(This protocol is specific to research in NCSU's BMMSL lab)

1. Locate the house vacuum pump in the BMMSL lab.
 - a) Make sure it has enough oil by observing the oil window located in line with the power switch on the side of the pump that faces the wall. Oil level should be between the two lines to the right of the window.
 - b) Flip the wall circuit breaker located just above the pump to the on position (up).
 - c) Press the white on button on top of the pump.
2. Turn on the power supply to the hotplates using the switch marked "recep" on the front panel of the hood and adjust hotplates to appropriate bake temperatures.
3. Turn on the power supply to the spinner using the switch marked "spinner" on the front panel of the hood and turn on the spinner using the on/off switch on the front of the spinner.
4. Line the spinning receptacle with aluminum foil.
5. Place a wafer chuck on the spinner.
6. Place a wafer centered onto the wafer chuck.
7. Set the spinner's initial "spread speed" by pressing the front portion of the foot pedal to start the wafer spinning and then selecting the appropriate speed on the spinner. Press the rear portion of the foot pedal to stop spinning.

8. Apply photoresist or adhesion promoter* by depositing ~1mL/inch of diameter wafer in the middle of the wafer and then immediately starting spinning.
9. After 5 seconds ramp the spinner up to its “application speed” and maintain for 30 seconds. Stop spinning.
10. Use wafer tweezers to gently remove the wafer from the wafer chuck and place it on a hotplate for the post application bake (PAB) and then immediately move to another hotplate for the PAB2 if necessary.
11. Let wafer cool for one to two minutes or cool instantly by touching the bottom side against a room temperature metal.

*Positive photoresists may require the application of an adhesion promoter or bilayer resist like LOR5A before applying the photoresist. Application of these additional compounds follows steps 8-11 after which the steps are repeated for the photoresist application.

Table B.1. Positive Photoresist Application Specifications

	LOR5A	SPR-3012	Hold time
Spread speed	500 rpm	500 rpm	5 s
Application speed	3000rpm	3000 rpm	30 s
PAB Temperature	170 C, 12 min	130 C, 1 min	-
PEB Temperature	-	130 C	1 min

Table B.2. Negative Photoresist Application Specifications

SU-8 2002	Desired thickness (μm)		Hold time
Spread Speed	2 – 3	500 rpm	5 s
Application speed	2	3000rpm	30 s
	2.5	2000 rpm	30 s
	3	1000 rpm	30 s
PAB Temperature	2 – 3	65 C	1 min
PAB2 Temperature	2 – 3	95 C	2 min
PEB1 Temperature	2 – 3	95 C	1 min
SU-8 2025	Desired thickness (μm)		Hold time
Spread speed	25 – 75	500 rpm	5 s
Application speed	25	3000rpm	30 s
	41	2000 rpm	30 s
	75	1000 rpm	30 s
PAB Temperature	41	65 C	1 min
	75	65 C	2 min
	75	65 C	3 min
PAB2 Temperature	41	95 C	3 min
	75	95 C	5 min
	75	95 C	9 min
PEB1 Temperature	25 – 75	95 C	1 min

B.2. CANON 501 With Alignment Procedure

START-UP

1. Turn on mercury lamp power supply (located on the floor):
 - a) Toggle switch ON.
 - b) Press silver START button. If the lamp does not turn on, wait 2 seconds then press the START button again. Repeat until the light starts. Let the bulb warm up for 15 minutes.
2. Turn on nitrogen and clean air flow by rotating supply valves 90 degrees counterclockwise. Gas lines are located to the right of the aligner on the wall just behind the adjacent hood.
3. Turn on the system's two vacuum pumps located to the right and rear of the aligner.
4. Turn on the main POWER switch located on upper left panel. Once the power is on, both wafer carriers will begin elevating in error. Stop the wafer carriers by pressing front and rear position triggers located at the top of both carrier tracks. The carriers should stop and the white button on the control consol will begin blinking.
5. Select the alignment mode by switching to CONTACT and HARD (or other appropriate application).
6. Switch the wafer feed in AUTO.
7. Press MANU alignment button if it is not lit.
8. Check the 4 gauges located below the main panel. They should read:

Vacuum > 50 cm

Pressure = 3.5 kg/cm²

Clean air = 2.2 kg/cm²

Nitrogen = 0.8 kg/cm²

LOAD MASK

1. Unlock the saddle for the lamp housing by pulling the v-shaped lever to the left rear of the housing. Swing the lamp house counterclockwise.
2. Load mask with pattern facing downwards (Cr or emulsion goes down and the mirrored side faces up). The wafer flat will face to the left.
3. Push mask flush against the top and left most stop holes in the upper left corner.
4. Turn on the vacuum to hold the mask by pressing the MASK LOAD switch.
5. Make sure the mask is oriented correctly so that subsequent plates do not need much alignment.
6. You may leave the saddle open for coarse alignment.

LOADING WAFERS

1. Press the blinking white button on the control consol and wait for the wafer carriers to reposition.

2. Place wafer face-up onto the front conveyer track and wait for the aligner to self-calibrate.

It may be necessary to guide the wafer back under the positioning arm at the end of the conveyer track if it rebounds out of the positioning area.

EXPOSURE SETTINGS

1. Set the LIGHT INTEGRA to the desired time.

Table B.3. Exposure time parameters

Resist	Thickness (μm)	Time (s)
SU-8 2002	2 – 3	30
SU-8 2025	25 – 41	30
SPR-3012 (on Si)	1.2	80
SPR-3012 (on quartz)	1.2	50

2. The ALIGN lamp will flash.

COARSE ALIGNMENT

1. With the saddle still open look at the wafer through the mask (using your eyes not microscope)

2. Make rough X-Y alignment by pressing the button on the alignment mouse and moving the mouse. This moves the wafer beneath the mask.
3. Make rough \emptyset alignment by rotating the mask with the \emptyset knob (located next to the X-Y mouse).
4. Return the saddle to the closed position.

ADJUST MICROSCOPE AND VIEW ALIGNMENT MARKS

1. Turn ILLUMINATOR ON.
2. Turn the LEFT and RIGHT knobs to obtain the desired microscope illumination.
3. Focus the objective lenses.
 - A. Focus the left lens with the focus knob for both fields of view (knob on right side of the saddle, below the scope light source).
 - B. Focus the right field of view using the right field knob (knob on left side of the saddle, below the scope light source).
4. Move the objective lenses so the desired alignment marks may be viewed. (One mark will be on left side of the wafer in the left lens, and one mark on the right side of the wafer in the right lens).

To adjust the microscope field of view, the black button next to the handle (noted with a red arrow) must be depressed while moving the microscope.

- A. Move the entire alignment scope left-right or back-front by depressing the release button (black button by grip) and moving the scanning grip (white handle on left of scope).
- B. Adjust the objective lens spacing with the right and left objective spacing knobs. (The right spacing view knob is on the left side of the stage, and the left view spacing knob is on the right side.)
- C. You should now simultaneously see the alignment marks from each side of the wafer in the microscope.

FINE ALIGNMENT

1. While observing the mask and wafer alignment marks through the microscope, perform X-Y and \emptyset fine alignment
2. Make fine X-Y alignment by moving the alignment mouse (don't press the button). This moves the wafer beneath the mask.
3. Make fine \emptyset alignment by using the \emptyset control switches on the front panel.
4. When satisfied with the alignment, press the ALIGN switch. The EXPO light will flash.
5. Using the microscope, recheck the alignment marks, If alignment is unsatisfactory press the ALIGN switch again and repeat 1-4.
6. Once alignment is satisfactory, press EXPO.
7. The ALIGN lamp will go out, the EXPO lamp will light continuously, and the alignment scope moves.

8. The shutter will open and expose the wafer.
9. Once the exposure is complete, the shutter closes and the EXPO lamp goes out.
10. The exposed wafer is sent to the take-up carrier but must be removed from the system immediately to prevent the take up carrier from elevating. The next wafer is ready to be loaded under the mask.
11. Perform coarse alignment, fine alignment, and exposure on the next wafer and continue until complete.

LOADING ERRORS If you get a load error press RELOAD and the wafer will be ejected.

SHUT DOWN

1. Turn off the power switch on the upper left panel. If no one else will be using the system soon turn off the lamp (power switch by the floor), vacuum pumps, and gas lines on the wall.
2. Turn off the spinner using the on/off switch on the front of the spinner and cut the power supply by using the switch marked “spinner” on the front panel of the hood.
3. Turn off the power supply to the hotplates using the switch marked “recep” on the front panel of the hood.
4. Discard contaminated aluminum foil and miscellaneous materials into the ventilated red trashcan.
5. Shut down the house vacuum pump in the BSML lab:
 - a) Press the red on button on top of the house vacuum pump.

b) Flip the wall circuit breaker located just above the pump to the off position (down).

B.3. Photresist Development

1. Place wafer on a hotplate for the post exposure bake (PEB).
2. Use tweezers to remove wafer from hotplate and let cool for one to two minutes or cool instantly by touching the bottom side against a room temperature metal.
3. Submerge wafer into a shallow container of an appropriate photoresist developer for at least 1 min or until features are visible.
4. Use tweezers to remove wafer from developer solution and gently rinse with water (for positive photoresists) or isopropanol (for negative resists) then carefully dry using compressed N₂ from the nitrogen gun.

C. Electron Beam Evaporate Protocol

(This protocol is specific to research in NCSU's BMMSL lab)

Initial Set-up: Evacuate vacuum chamber

Given that:

- Chamber is at atmospheric pressure.
- Chamber vent and pump vent valves are open, all others are closed.
- Ion gage is off.

1. Start pump
2. Close the *pump vent valve*.
3. Wait ~15 seconds and then close the *chamber vent valve* and open the *roughing valve*.
4. When chamber pressure reads below 0.15 Torr, close the *roughing valve* and wait for valve hissing to quiet.
5. Open the *pump vent valve*.
6. Once the foreline pressure stabilizes (~40 Torr), turn the roughing pump off.
7. Open the cryogate. Chamber pressure drops rapidly.

Initial Checks: Before starting the E-beam system, make the following checks.

1. Ion Gage reads a pressure of no higher than 10^{-7} Torr.

2. Pocket leads are connected correctly on the side of the tank: orange is connected when using four pockets and yellow when using one.
3. Shutters are in the closed position (facing away from the front of the vacuum chamber).

Run: Initiating and controlling E-beam deposition.

1. Fill out run sheet
2. Open the four H₂O valves (two for the H₂O source and two for the drain) on the wall behind the instrument.
3. Open the H₂O flow valve to the crystal. Valve is located on top of the chamber.
4. Turn on power to the *IC6000* monitoring module.
5. Visually inspect in the chamber mirror that the source pocket is rotated to the metal intended for deposition.
6. Check to ensure that the correct density is displayed for the material in use. Density can be change by pressing **Disp** then **1**.
7. Bring up operating menu by pressing **Disp** then **8**.
8. Press **Abort** to prevent accidental start-up.
9. Energize main system power by flipping the large wall switch to the on position (up).
10. Switch on (up) the two switches on the *High Voltage EPO* power supply module.

11. Use the green key to power the *TT Series Control* module and then press main power **On**.
12. Hit **Reset** and check that all the interlocks light.
13. If Aux 1 and 2 interlocks do not light, use the yellow key to release the red knob to unlock the High Voltage Interlock. Hit **Reset** again, all interlock lights should light.
14. Wait ~ 5 min before turning High Voltage on.
15. On *TT Series Control* module, turn high voltage **On** and increase it to – 6 kV.
16. On *TT Series Control* module, turn source **On**.
17. Of the three ways to turn on current (local, handheld, remote) on the *Main Power* module, ensure the switch is toggled up to **Local**.
18. Push **Reset** on *IC6000* and then **Man** to activate the beam.
19. Adjust the emission current on the *TT Series Control* module to about 0.02A or to where the dial reads 60. Wait one minute then gradually increase the power by about 0.01A/min until the beam becomes visible (usually between 0.03-0.05A).
20. Use the Lat and Long position and amplitude knobs on the *Power Supply Controller* to position the beam so that it sweeps only across the metal sample. Sparks outside the pocket are signs that the beam is hitting the chamber and needs to be repositioned into the pocket!
21. Deposition is ready to begin when the deposition rate becomes steady at an acceptable level (between 1-5Å/s)

22. When deposition is ready to begin, open the appropriate shutter and hit **Zero**.

Shut Down: Stopping the run and shutting down the instrument.

1. Turn down emission current on the *TT Series Control* module.
2. Hit **Abort** on the *IC6000*.
3. Turn Source and High Voltage off on *TT Series Control* module.
4. Wait 5 minutes before turning off main power switches on the *High Voltage EPO* power supply.
5. Turn the ion gage off.
6. Close gate valve (always).
7. Turn the N₂ on.
8. Closed baritron gauge valve and the process gas valve.
9. Open chamber vent valve (chamber pressure increases to atmospheric).
10. Open right shutter then close it slightly (~1/2")
11. Wait at least 5 minutes after the pocket glow fades then turn crystal H₂O valve off.
12. Turn source H₂O valve off.
13. Turn H₂O drain valve off.

Top up: Raise the top to remove/position samples.

1. With your right arm steadying the chamber lid, use your right hand to press the red operation button while simultaneously pushing the operation switch up. Ensure that nothing hits during elevation.
2. Swivel the lid counterclockwise to get it away from the chamber so nothing can fall down into the chamber.

Top down:

1. Reverse the Top up procedure making sure that the red and black marks on the chamber and lid lips align.

Bottom down: Lower the chamber bottom to refill pockets, access source, etc.

1. Use your right hand to press the red operation button while simultaneously pushing the operation switch down. Ensure that nothing hits during descent.
2. Swing the bottom out clockwise.
3. Carefully use discharge rod to touch high voltage leads.

Troubleshooting

Cryopump gate valve does not open: stuck closed.

1. Repeat open/close procedure.
2. Vent Chamber the repeat open/close procedure.

3. Turn off cryopump compressor and let the chamber and pump pressures equilibrate.

Repeat open/close procedure.

Chamber does not hold pressure: chamber leak

1. Vent chamber. Inspect seals around top and bottom lids.

Chamber slow to rough down: chamber leak

1. Vent chamber. Inspect seals around top and bottom lids.
2. Inspect roughing pump belt and replace if worn.

Cryopump has condensation on outside: cold short.

1. Regenerate pump.

Cryopump will not hold pressure below $1\mu\text{T}$: needs regenerating

Usual parameters

Operating pressure $\leq 5 \times 10^{-7}$ Torr.

Voltage = 6 kV

Cr deposits ~ 1 angstrom/s at 0.06A

Au deposits $\sim 1/2$ angstrom/s at 0.13A